HARVARD UNIVERSITY
Graduate School of Arts and Sciences

DISSERTATION ACCEPTANCE CERTIFICATE

The undersigned, appointed by the

Department of Physics

have examined a dissertation entitled

Electrical and thermoelectric transport in mixed-dimensional graphitic mesoscopic systems

presented by Laurel Erin Anderson

candidate for the degree of Doctor of Philosophy and hereby certify that it is worthy of acceptance.

Signature _____

Typed name: Professor Philip Kim, Chair

Signature _____

Typed name: Professor Amir Yacoby

Signature _____

Typed name: Professor Subir Sachdev

Date: August 3, 2022

Electrical and thermoelectric transport in mixed-dimensional graphitic mesoscopic systems

A DISSERTATION PRESENTED
BY
LAUREL ERIN ANDERSON
TO
THE DEPARTMENT OF PHYSICS

IN PARTIAL FULFILLMENT OF THE REQUIREMENTS
FOR THE DEGREE OF
DOCTOR OF PHILOSOPHY
IN THE SUBJECT OF
PHYSICS

HARVARD UNIVERSITY
CAMBRIDGE, MASSACHUSETTS
AUGUST 2022

Thesis advisor: Professor Philip Kim Laurel Erin Anderson

Electrical and thermoelectric transport in mixed-dimensional graphitic mesoscopic systems

Abstract

Confining electrons to fewer than three spatial dimensions increases the relative strength of potential to kinetic energy, which can generate a wide variety of novel emergent quantum phenomena. I will discuss three experiments probing the unique physics of coupled 1D-2D and 0D-2D systems. First, we studied Coulomb drag between a 1D conductor and a 2D conductor: an individual single-walled carbon nanotube and monolayer graphene, separated by a few-atom-thick hexagonal boron nitride layer. We found novel temperature- and carrier density-dependent drag behavior arising from the mixed-dimensional nature of the system, including possible hydrodynamic flow of graphene electrons generated by current in the nanotube. Separately, we measured thermal transport in carbon nanotubes using 2D graphene sections as heaters and thermometers via Johnson noise measurements. We demonstrated the high sensitivity of our thermometry technique and observed signatures of unusual energy transport due to collective 1D electronic motion combined with long-range interactions. Finally, we studied electrical and thermoelectric transport through an etch-defined graphene quantum dot in a strong magnetic field, where irregularity on the edge of a small flake in the lowest Landau level is predicted to generate novel non-Fermi liquid behavior. We found significant deviations of the thermoelectric response from the predictions of the Mott formula at high magnetic fields, and electrical conductance and thermopower resonances that suggest an interplay of quantum Hall physics, Coulomb interaction, quantum confinement and disorder at a range of temperatures.

Contents

Title Page i

Copyright ii

Abstract iii

Table of Contents iv

Listing of figures vi

Dedication xi

Acknowledgments xii

Previous publications and list of authors xvi

1 Introduction 1

1.1 Introduction to graphene and carbon nanotubes 3

1.2 Electrical conductivity, thermal conductivity, and thermopower 10

1.3 Graphene hydrodynamics 13

1.4 The quantum Hall effect in graphene 16

1.5 Coulomb drag in graphene 20

2 Carbon nanotube-graphene Coulomb drag 27
2.1 Theory for nanotube-graphene Coulomb drag . . . 28
2.2 Coulomb drag as a potential probe of hydrodynamics in graphene . . . 29
2.3 Drag device fabrication . . . 31
2.4 Coulomb drag measurements . . . 35
2.5 Nonlinearity and breaking Onsager reciprocity . . . 42
2.6 Carrier density and temperature-dependent drag . . . 46
2.7 Estimation of nanotube and graphene carrier densities . . . 50
2.8 Comparison of SWNT-graphene Coulomb drag with theory . . . 55
2.9 Distance dependence of Coulomb drag response in graphene . . . 60

3 Electronic thermal transport in carbon nanotubes 63
3.1 Johnson noise thermometry in graphene . . . 64
3.2 Multi-terminal noise measurements of thermal conductivity . . . 65
3.3 Thermal transport device fabrication . . . 73
3.4 Johnson noise measurements of carbon nanotube devices . . . 75
3.5 Outlook . . . 88

4 Toward realization of the Sachdev-Ye-Kitaev model in graphene 90
4.1 "Black hole on a chip:" the Sachdev-Ye-Kitaev model . . . 91
4.2 Theoretical predictions for transport observables of an SYK dot . . . 97
4.3 Experimental design and dot device fabrication . . . 99
4.4 Electrical and thermoelectric response at zero magnetic field . . . 104
4.5 Dot measurements at finite magnetic field . . . 110
4.6 Discussion . . . 122

5 Outlook and future directions 126

Appendix A Supporting data 129

A.1 Additional Onsager data 129

A.2 Individual layer transport and drag resistance in different measurements 133

Appendix B Thermopower measurement technique 138

B.1 AC thermopower measurements 139

B.2 Temperature gradient estimation with quantum Hall thermometry 141

Appendix C Rayleigh scattering spectroscopy, imaging and transfer of carbon nanotubes 144

C.1 Theory of Rayleigh scattering spectroscopy for carbon nanotubes 145

C.2 Technical considerations and description of the tool 148

Appendix D MATLAB code for Rayleigh scattering spectroscopy 157

D.1 Background subtraction program (rly.m) 158

D.2 Peak fitting program (rlypk.m) 160

References 175

Listing of figures

1.1 Graphene lattice, Brillouin zone, and Dirac cones. 4

1.2 Construction of a carbon nanotube from graphene lattice. 7

1.3 Schematics of thermal conductivity and thermopower measurements. 11

1.4 Illustration of Ohmic and hydrodynamic electron flow. 14

1.5 Schematics of Couette flow and nanotube-graphene hydrodynamic Coulomb drag experiment. 16

1.6 Landau level density of states and quantized Hall conductance in graphene. 17

1.7 Schematics of thermopower in the quantum Hall regime. 19

1.8 Schematic of Coulomb drag in a 2D-2D system. 21

1.9 Coulomb drag in a double graphene heterostructure. 23

1.10 Schematic of energy drag for two graphene layers at charge neutrality. 24

2.1 CVD furnace for nanotube growth and schematic of suspended nanotube growth. 32

2.2 Nanotube suspended growth, imaging and characterization. 32

2.3 Fabrication sequence for SWNT-graphene devices. 34

2.4 SWNT-graphene device image, individual layer characterization and gate-dependent Coulomb drag at $T = 300$ K. 36
2.5 SWNT conductance gate sweeps and corresponding drag resistance. 38
2.6 SWNT conductance and drag resistance in a SWNT-bilayer graphene device. . . . 39
2.7 Circuit diagrams for DC drag measurement. 41
2.8 Breakdown of layer reciprocity at low temperatures. 44
2.9 Carrier density dependence of SWNT-graphene drag at various temperatures. . . . 48
2.10 Drag resistance as a function of temperature. 49
2.11 COMSOL simulation of SWNT-graphene device. 51
2.12 Equivalent capacitance circuit of SWNT-graphene device. 52
2.13 SWNT-BLG device schematic and effects of various gate voltages on resistance. . . 53
2.14 Band diagrams of SWNT-graphene heterostructure. 56
2.15 Distance dependence of SWNT-graphene drag. 61

3.1 Schematic of graphene self-heating measurement with Johnson noise 65
3.2 Schematic of multi-terminal noise measurement. 66
3.3 Schematic, image and equivalent thermal circuit of graphene thermometry device with carbon nanotube bridge. 67
3.4 Geometry for derivation of relationship between energy current across the bridge and cold side noise measurement. 69
3.5 Differential noise thermometry circuit schematic. 71
3.6 Balancing circuit schematic for example device. 72
3.7 Images of nanotube-graphene thermometry device at various stages of fabrication. 74
3.8 Current annealing and low-temperature resistance of nanotubes. 75
3.9 Characterization of excess energy loss in NT-graphene devices. 77

3.10 Electrical and thermal conductance measurements of two nanotube-graphene thermometry devices as a function of gate voltage. 79
3.11 Nanotube electrical and thermal conductance in the bandgap. 82
3.12 Temperature dependence of Device 1 at constant NT doping and thermal bias at $V_g^{NT} = -5$ and 0 V. 84
3.13 Temperature dependence of Device 1 at constant NT doping and thermal bias at $V_g^{NT} = 5$ and 10 V. 85
3.14 Nonlinear thermal transport across nanotube bridges. 87

4.1 Energy levels as a function of magnetic flux and wavefunction amplitudes for a small graphene flake. 95
4.2 Schematic of SYK island and theoretical predictions for electrical conductance and thermopower. 98
4.3 Schematics and images of graphene quantum dot device fabrication and operation. 100
4.4 Electrical transport in dot and reservoirs at $B = 0$ T. 105
4.5 Electrical transport at $B = 0$ T with DC bias. 106
4.6 Thermopower and comparison to Mott formula at $B = 0$ T. 108
4.7 Dot electrical conductance as a function of top and bottom gate voltages at $B = 10$ T and line scans of conductance and thermopower with $\nu_{res} = 2$ 111
4.8 Calculation of ν_{dot} and illustration of different regimes of transport through the dot. 113
4.9 Evolution of electrical conductance, Mott formula calculation, and thermopower as a function of V_{bg} and B at $T_{bath} = 3$ K. 115
4.10 Evolution of electrical conductance as a function of ν_{dot} and T_{bath}. 117
4.11 Evolution of thermopower as a function of V_{bg} and T_{bath}. 120

4.12 Crossovers in transport between SYK regime and Schwartzian regime with finite-N effects. 123

A.1 Drag voltage at $T = 300$ K as a function of drive current and gate voltage, with graphene as the drive layer and SWNT as the drag layer. 130

A.2 Drag voltage versus drive current at various gate voltages for reciprocal layer configurations. 132

A.3 Individual layer transport and drag resistance as a function of back gate voltage for measurement D1-A. 134

A.4 Image and drag measurements of device D2. 135

A.5 Image, drag measurement and individual layer characterization of device D3. . . . 137

B.1 Circuit schematic for dot thermopower measurements. 139

B.2 Circuit schematic and example data for temperature gradient estimation. 142

C.1 Kataura plot of nanotube transition energies versus diameter. 147

C.2 Polarization dependence of carbon nanotube Rayleigh scattering. 149

C.3 Front view of stage and manipulators. 151

C.4 Side view of stage and manipulators. 152

C.5 Front view of imaging column. 153

C.6 Top view of imaging column. 154

C.7 Top view of camera/spectrometer coupling array. 155

C.8 White laser coupler. 156

This thesis is dedicated to my family, who have encouraged and guided my way in science for as long as I can remember.

Acknowledgments

It is truly impossible to adequately acknowledge everyone whose guidance, support, insights and other help have made my graduate research possible. I am certain to leave out some important people here, so I hope I have been able to express my gratitude to everyone over the years as well.

Most importantly, I would like to thank my advisor, Philip Kim. I am extremely lucky to have had the chance to work in his lab. Philip has a deep knowledge of physics and an amazing sense of what the important questions are. He provided the key insights into many questions, large and small, that I encountered in the course of my research. He taught me so much about how to approach physics ideas and experiments, and helped me grow into a much better and more confident scientist. He was also an exceptionally supportive mentor in more ways that I can count. I'm not sure if I have the record for the longest continuous measurement of a single device in the lab, but I am grateful that he trusted me to keep measurements running efficiently. I think it's common for graduate students to be nervous before meetings with their advisor, but I pretty much always left Philip's office feeling better than before (which is not so common!). In very tough situations, I always felt that he had my back. In so many ways, he is the kind of scientist I hope to be someday, and

I am very grateful to have been one of his students.

I would also like to thank my committee members, Amir Yacoby and Subir Sachdev, for interesting discussions, excellent questions to consider, and helpful advice over the years. I learned a great deal from talking with them and very much appreciate their guidance.

Another one of Philip's good qualities is that he encourages a collaborative and creative atmosphere in his research group, and fills it with talented and interesting scientists. There are so many people in the Kim lab who made it an exceptional place to do research over my years in the group. Austin was my main mentor in the lab and taught me how to do essentially everything in the first years of my PhD. He set high standards and pushed me to do the best work that I could, but was always encouraging. I really appreciate his enthusiasm, perseverance, insistence on scientific rigor, and good spirits in our time working together.

I also want to thank the various Kim group postdocs who have been mentors, colleagues and friends over the years. Jonah gave me a insight into carbon nanotube physics, invaluable advice about how to approach difficult experiments, and abundant moral support. Yuval also provided a great deal of advice and good ideas, as well as inspiration to better organize my research materials. My time working with Antti was challenging, but I learned a lot from the experience. Most recently, Andrew has been a fantastic colleague; I would have had a hard time getting through the SYK measurements without the help he provided in countless ways. Working with them has made me excited to be a postdoc myself.

As tempting as it is to give individual thanks to everyone who overlapped with me in the group (you are all exceptional), I will restrict myself to a few more: my year-mates Artem and Rebecca, for the problem set commiserations, experimental discussions, and general fun; Tom, for many excellent physics discussions and for teaching me various useful fabrication and experimental techniques; Frank, for helping me out with so many of the little problems that crop up in the lab; Zeyu, for interesting time at Maglab and useful feedback on data and writing; Zhongying, for lending com-

ponents and helping me understand noise measurements; and a final thanks to everyone who didn't run away during the many, many times that I wandered into the kitchen or office saying, "Can anyone give me a hand with this transfer line?"

I would also like to thank my previous research advisors, in more-or-less chronological order. Jennifer Shumaker-Parry gave me a great early taste of research (and I can't believe she let a high school student have such free rein in the lab!). My undergraduate research advisor, Chandrasekhar Ramanathan, was a great mentor, extremely patient and encouraging as well as deeply interested in fundamental science. He was the one who first got me interested in quantum chaos, and I'm delighted to have finally circled back to the subject in a roundabout way. Jordan Gerton allowed me to dip my toe into the deep waters of NV center physics; years later, helping to build the Rayleigh setup, it was good not to be a total optics novice! Finally (before Harvard), Andrew Ferguson, my MPhil supervisor, for his support and for many delightful physics conversations. On a related note, I am grateful to my high school physics teacher, Dan McGuire, for showing many of us how beautiful and fun physics can be, and for encouraging my interest in the subject.

The Harvard physics department has been an extremely supportive community during these fun, but sometimes very difficult, years of my life. I appreciate Jacob Barandes, Lisa Cacciabaudo, Hannah Belcher and Melissa Franlin for their advice; Alex Kruchkov, for being an enthusiastic and indefatiguable theory collaborator; and all of the staff in LISE, especially the CNS staff, for keeping the instruments running and providing many tips on the best ways to pursue an experimental goal. Finally, my wonderful friends in physics and adjacent fields: the Dungeons & Dragons crew (Kristine, Sasha, Cole, Nick, Ann, Linda...or perhaps should I say Amafrey, Ryth, Bharash, Akkan, Sparklegem, Greenpeace...), Grace, Elana, Abby, Delilah, David, Maya, Trisha, Olivia, and so many others.

Finally, I would like to thank my family. My grandparents were an endless source of love, and "Grandpa B." in particular helped inspire my first interest in physics by sharing telescope time and

Stephen Hawking books. My brothers, Zach and Todd, have very literally been with me from the beginning, and I'm glad our shared interests have kept us together even through cross-country relocations for college and graduate school. Last but not least, my amazing parents have been great role models as scientists and as people. Growing up, they encouraged all three of us to pursue our curiosity, and demonstrated that a life in science can be challenging, but rewarding and a lot of fun. I am immensely grateful for all their support.

Previous publications and list of authors

Results in Chapter 2 were published in:

> "Coulomb Drag between a Carbon Nanotube and Monolayer Graphene," Laurel Anderson, Austin Cheng, Takashi Taniguchi, Kenji Watanabe, and Philip Kim. Physical Review Letters 127(25), 257701 (2021).

Results in Chapter 3 were published in:

> "Electronic thermal transport measurement in low-dimensional materials with graphene non-local noise thermometry," Jonah Waissman, Laurel E. Anderson, Artem V. Talanov, Zhongying Yan, Young J. Shin, Danial H. Najafabadi, Mehdi Rezaee, Xiaowen Feng, Daniel G. Nocera, Takashi Taniguchi, Kenji Watanabe, Brian Skinner, Konstantin A. Matveev, and Philip Kim. Nature Nanotechnology 17, 166–173 (2022).

The following authors contributed to Chapter 4: Laurel E. Anderson, Andrew Zimmerman, Antti Laitinen, Alexander Kruchkov, Takashi Taniguchi, Kenji Watanabe, and Philip Kim.

More is different.

Philip W. Anderson

1 Introduction

The fundamental appeal of studying condensed-matter physics for many scientists (certainly for me) comes from the fact that when you consider large numbers of particles together, new emergent behavior arises that can be quite different from what could be predicted based on their single-particle motion. The "mesoscopic" realm, spanning length scales of hundreds of microns to a few nanometers [1], and low-dimensional systems in particular, host a menagerie of interesting quantum phases. "Zero-dimensional" (0D) quantum dots can behave as "artificial atoms" despite their much larger

size, and can demonstrate more exotic physics when coupled to larger systems[2,3]. Different velocities for collective excitations of spin and charge have been observed in effectively one-dimensional (1D) carbon nanotubes, a hallmark of Luttinger liquid physics[4]. In the two-dimensional (2D) realm, electrons in graphene can sometimes behave like a viscous fluid[5]. Even before atomically-thin materials, experimenters looked to two-dimensional electron gases (2DEGs) to study phenomena like the quantum Hall effect[6]. Why do all of these novel quantum behaviors arise in low-dimensional systems? As electrons become increasingly confined, their kinetic energy becomes less important than their potential energy (i.e. their interactions), so interaction effects are enhanced[5].

Since graphene was first isolated in 2004[7], it and other atomically-thin van der Waals materials have opened up a brand new test bed for mesoscopic physic experiments. This is in part due to the unique properties of graphene as a Dirac semimetal, which will be discussed in more detail in Section 1.1; as an atomically-thin material, it is particularly easy to tune the carrier density with electrostatic gating, and unlike most conventional 2DEGs, the carrier type can be switched between electrons and holes. Many more van der Waals materials with various electronic properties (insulators, semiconductors, antiferromagnets, ferroelectrics, and more) have since been discovered, and they can be stacked together due to their interlayer electrostatic interaction. In particular, the advent of encapsulation of graphene with insulating hexagonal boron nitride (hBN)[8] and the ability to make electrical contacts only to the edge of a fully-encapsulated sample[9] ushered in a new era of high-quality transport measurements on graphene heterostructures. More recently, the demonstration of superconductivity[10] and other strongly-correlated phases in magic-angle twisted multi-layer graphene has generated an explosion of effort to probe the new phenomena that the additional "twist" degree of freedom provides.

Various low-dimensional materials have been demonstrated as promising platforms for mesoscopic physics experiments, so why study mixed-dimensional systems? In general, the experiments I will describe were not conceived with the explicit intention of studying what happens when elec-

trons that are confined to a *different* number of dimensions interact. The aim of the first project, which measured Coulomb drag between a carbon nanotube and graphene, was to study graphene hydrodynamics, which had at that point been theoretically predicted [11,12,13] but not experimentally observed.

1.1 Introduction to graphene and carbon nanotubes

Many of the unique electronic properties of monolayer graphene and carbon nanotubes can be derived from their crystal structures with relatively simple assumptions (such as nearest-neighbor hopping in the tight-binding model). Since these concepts have been known for decades and have been explained in many excellent references (I particularly recommend Refs. 14, 15, 16, 17), I will only discuss key elements of the physics of graphene and carbon nanotubes in this section.

1.1.1 Structure and properties of graphene

Graphene is a single-atom-thick crystal of carbon atoms, arranged in a honeycomb lattice as shown in Figure 1.1(a). This can be described as a hexagonal Bravais lattice with a two-atom basis, with the two atoms typically labeled A and B. The primitive cell is a parallelogram with side length $a = \sqrt{3}a_{C-C} = 2.46$ Å, where $a_{C-C} = 1.46$ Å is the carbon-carbon bond length, and the lattice vectors are

$$\vec{a_1} = \left(\frac{\sqrt{3}a}{2}, \frac{a}{2}\right), \vec{a_2} = \left(\frac{\sqrt{3}a}{2}, -\frac{a}{2}\right). \tag{1.1}$$

The corresponding reciprocal lattice is also hexagonal (Fig. 1.1(b)), rotated 90° relative to the real-space lattice and with reciprocal lattice vectors

$$\vec{b_1} = \left(\frac{2\pi}{\sqrt{3}a}, \frac{2\pi}{a}\right), \vec{b_2} = \left(\frac{2\pi}{\sqrt{3}a}, -\frac{2\pi}{a}\right). \tag{1.2}$$

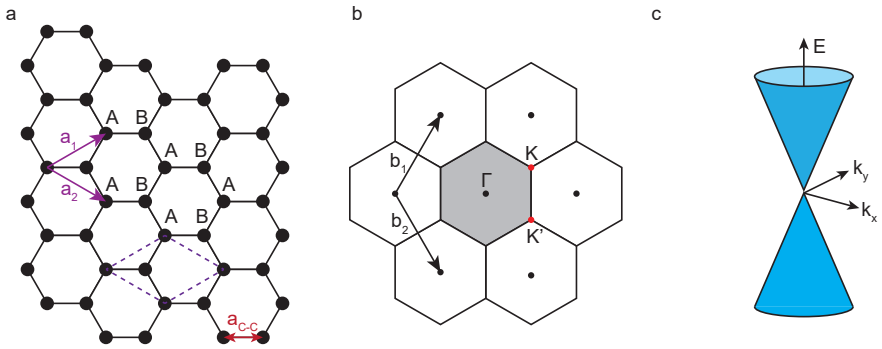

Figure 1.1: (a) Graphene honeycomb lattice. The primitive vectors $\vec{a_1}$ and $\vec{a_2}$ are indicated in purple, the primitive unit cell is the equilateral parallelogram (dashed purple lines) with a basis of two atoms labeled A and B. The carbon-carbon bond length a_{C-C} is also shown. (b) Reciprocal lattice of graphene. The first Brillouin zone is the shaded center hexagon. Reciprocal lattice vectors are $\vec{b_1}$ and $\vec{b_2}$, and high-symmetry points Γ, K and K' are also labeled. (c) Linear energy dispersion of graphene at the K point. Adapted from Ref. 15.

The most important points in the first Brillouin zone, due to their high symmetry, are the Γ point in the center and the K and K' points at the vertices of the hexagon. Since the two basis atoms of the graphene lattice are both carbon atoms, the K and K' points are identical in most respects, but they have opposite values of pseudospin. Graphene pseudospin is not related to the actual spin of the electrons; rather it describes the extra degree of freedom that describes the orbital wavefunctions sitting on either the A or B sublattices. As shown below, the two-component vector that quantifies the weight of the wavefunction on each sublattice can be treated similarly in many ways as a spin-1/2 degree of freedom, and is often described with a "pseudospinor" analogous to the spinor that describes the spin degree of freedom.

The band structure of graphene can be calculated using the tight-binding formalism, starting from a wavefunction comprising a weighted sum of the Bloch wavefunctions for the A and B sublattices:

$$|\Psi_{\vec{k}}\rangle = \sum_{\vec{R}} e^{i\vec{k}\cdot\vec{R}}(\sigma_A|\vec{R}, A\rangle + \sigma_B|\vec{R}, B\rangle), \tag{1.3}$$

where $\vec{R}$ describes the location of a particular primitive unit cell in the crystal, $\sigma_{A(B)}|\vec{R}, A(B)\rangle$ is the wavefunction for an electron to be on the A(B) site in the primitive unit cell located at $\vec{R}$, and $\sigma_{A(B)}$ are the corresponding weights. Using this wavefunction to solve the Schródinger equation, we find the dispersion relation

$$E(\vec{k})^{\pm} = \pm\gamma\sqrt{1 + 4\cos\frac{\sqrt{3}a}{2}k_x\cos\frac{a}{2}k_y + 4\cos^2\frac{a}{2}k_y}. \tag{1.4}$$

Here $\gamma = 3.7$ eV refers to the nearest-neighbor hopping energy between adjacent carbon atoms and the two solutions ($\pm$) correspond to the conduction and valence bands, respectively.

If we shift our perspective to one of the K or K' points (redefining $\vec{k} \to \vec{K} - \vec{k}$, for instance), the dispersion relation becomes

$$E(\vec{k})^{\pm} = \pm\hbar v_F|\vec{k}|, \tag{1.5}$$

where $\hbar$ is the reduced Planck's constant and the Fermi velocity v_F is given by $(1/\hbar)(\partial E/\partial k)$ at the Fermi energy E_F, and is approximately 10^6 m/s. Thus, near the K and K' points, the dispersion forms the famous "Dirac cone" shown in Figure 1.1(c), and the K and K' points where the two cones of the conduction and valence bands touch (which occurs at the Fermi energy) called Dirac points. Due to the resemblance between this relation and the Dirac equation describing the motion of massless relativistic particles, the electrons in graphene are often described as "Dirac fermions," moving at 1/300 the speed of light! This is also the charge neutrality point of the graphene, since if E_F increases, the conduction band begins to fill with electrons, and if E_F decreases, there are instead "holes" in the valence band. The pseudospin is parallel to the momentum in the conduction band and antiparallel in the valence band, analogous to the correlation of momentum and real spin in the Dirac equation. At finite temperature, when E_F is at or near zero, there will be coexisting populations of thermally-excited electrons and holes. This "Dirac fluid" is a quantum-critical hydrody-

namic liquid[18,19,20]—an unusual phase that develops near the boundary between two stable phases, in this case between electron and hole Fermi liquids, and more of its properties will be discussed as they become relevant in later sections.

The existence of the Dirac fluid and the effectively massless nature of the charge carriers in graphene are only two of its many fascinating properties. Another that is relevant to the physics that will be discussed in the rest of this chapter is the suppression of backscattering. The Fermi surface is generally confined to either the six K and K' points (in the case of intrinsic or undoped graphene) or to six small circles around each Dirac point (for lightly-doped graphene). Backscattering an electron, taking it from momentum $\vec{k}$ to $-\vec{k}$, means that in momentum space it will move to the opposite side of the first Brillouin zone. We note that the high-symmetry point opposite a K point is a K' point, with an opposite pseudospin, corresponding to the electronic wavefunction being localized on the opposite sublattice. Since pseudospin is a conserved quantity near the Dirac points, this is forbidden, so backscattering is strongly suppressed[21,22,23]. This improves the carrier mobility in graphene, with important implications for the behavior of carbon nanotubes as well.

1.1.2 Structure and properties of carbon nanotubes

Although it is not how they are formed in synthesis, many properties of carbon nanotubes can be understood by thinking of them as "rolled-up graphene." The underlying lattice is the same as that of graphene, but we now must consider exactly how this lattice is "rolled"—which atoms are mapped onto each other—in order to form the nanotube. This is described by the chiral vector $\vec{C}$, illustrated in Figure 1.2 and defined via the graphene primitive lattice vectors as

$$\vec{C} = n\vec{a_1} + m\vec{a_2} = (n, m), 0 \leq m \leq n. \tag{1.6}$$

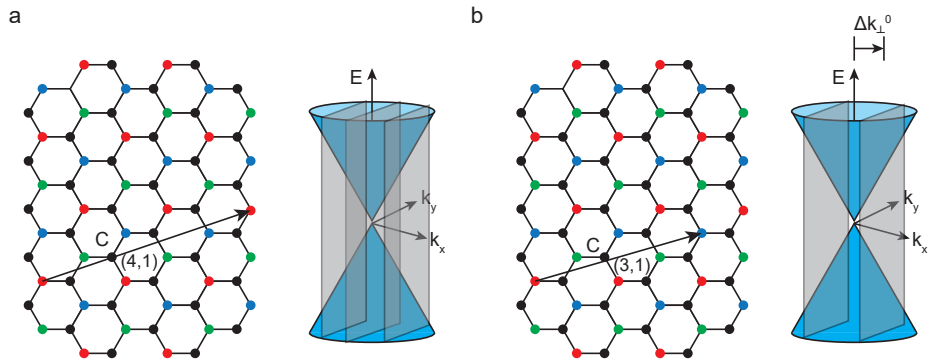

Figure 1.2: Construction of a carbon nanotube from graphene lattice. Colors indicate wavefunction phase on the A sublattice: 0 (red), $2\pi/3$ (green), and $4\pi/3$ (blue). (a) Rolling the graphene lattice such that the chiral vector $\vec{C}$ becomes the tube circumference forms a metallic carbon nanotube with chiral indices (4,1). The lowest-energy subband passes through the Dirac point. (b) Performing this operation for the chiral vector $\vec{C}$ =(3,1) results in a phase mismatch, causing the lowest-energy subband not to intersect the Dirac point. $\Delta k_{\perp}^{0}$ is the wave vector describing the shift due to this mismatch, measured from the K point. Adapted from Refs. 15, 17.

The resulting structure is referred to as an (n, m) carbon nanotube. From this, we can immediately find the nanotube diameter

$$d_t = \frac{|\vec{C}|}{\pi} = \frac{a\sqrt{n^2 + nm + m^2}}{\pi}. \tag{1.7}$$

We can see from this that different chiral vectors can result in the same diameter, so measuring the diameter (e.g. using atomic force microscopy) is not sufficient to determine the crystal structure. It is also worth noting that since the chiral vector is a linear combination of primitive lattice vectors, it cannot map an atom on the A sublattice to an atom on the B sublattice. This is disallowed by pseudospin conservation; mapping an A atom to a B atom would only be permitted if the pseudospin were the same.

To see the implications of the crystal structure for the electronic properties, it is helpful to move to reciprocal space. "Rolling up" the graphene lattice imposes an additional periodic boundary condition on the electronic wavefunctions [17], so the crystal momentum in the circumferential direction,

$k_\perp$, is quantized according to

$$k_\perp \pi d_t = 2\pi l, \tag{1.8}$$

where l is an integer. As a result, the first Brillouin zone consists of 1D line cuts of graphene's hexagonal Brillouin zone, with the length and angle of these cuts determined by the chiral vector. Each line cut contributes a 1D subband to the dispersion relation. If one of these line cuts passes through a Dirac point, the lowest-energy subband will have a linear dispersion (essentially a 1D version of the graphene dispersion) and the nanotube is metallic; if no cuts intersect with the Dirac point, the nanotube is semiconducting because all the subbands have energy gaps.

The conditions to form a metallic or semiconducting nanotube can also be seen from the graphene lattice. There are three possible values for the phase of the wavefunction on the A sublattice: 0, $2\pi/3$, and $4\pi/3$ (colored red, green, and blue in Figure 1.2). When the graphene lattice is rolled into a cylinder, it can happen that a red atom is mapped to another red atom, in which case the wavefunctions at the K (and K') points are automatically solutions to the Schödinger equation on the cylinder. Therefore, one of the line cuts must intersect with the K (and K') points, so the nanotube is metallic. On the other hand, if a red atom is mapped to a green or blue atom, there is a phase mismatch of $2\pi/3$ that must be adjusted for the wavefunction to be single-valued. This happens by using a wavefunction that some value $\Delta k_\perp^0$ away from the K point, which will have an envelope $e^{j\Delta k_\perp^0 r_\perp}$. (We use the convention that wavevectors $\vec{k}$ are measured from the Γ point; $\Delta\vec{k_\perp} = \vec{k_\perp} - \vec{K}$ is measured from the K point.) For the right value of $\Delta k_\perp^0$, this generates a phase modulation along the circumferential direction that compensates for the mismatch (i.e. $\Delta k_\perp^0 \pi d = -2\pi/3$). These nanotubes will have a lowest-energy subband that is away from the K and K' points, so they are semiconducting. Since each phase on the A sublattice occurs exactly $1/3$ of the time, a synthesized batch of nanotubes is generally $1/3$ metallic and $2/3$ semiconducting. These phase conditions can be conveniently expressed in terms of the chiral indices: if $(n - m)$ is an integer multiple of 3 or 0,

the nanotube is metallic. In practice, we can identify metallic versus semiconducting nanotubes by their transport properties or, more conveniently, by various optical spectroscopic methods [24,25,26]. We used Rayleigh scattering spectroscopy to characterize the carbon nanotubes for the experiments discussed in this thesis, which is discussed in more detail in Appendix C.

A final note on the electronic properties of carbon nanotubes: the suppression of backscattering in graphene due to pseudospin conservation can be even more important in carbon nanotubes. For metallic nanotubes, the Fermi surface is reduced from a circle to two points at k and $-k$, since the momentum is confined in one dimension, and backscattering is again forbidden [27]. As a result, metallic carbon nanotubes can have extremely long electron mean free paths, up to tens of microns [21,27]. In semiconducting nanotubes, since the lowest-energy subband does not intersect any K or K' points, the angle between the initial and final momentum states (with respect to a K point) will be less than π, so there will be more overlap of the pseudospinors and this scattering is much less strongly suppressed. The potential for higher-quality transport is one factor that led us to focus on using metallic carbon nanotubes for the devices used to study carbon nanotube-graphene Coulomb drag.

Aside from the scientific results, the nanotube-graphene drag project led to significant technical developments, most notably the Rayleigh scattering spectroscopy, imaging and transfer stage (Appendix C). With this unique tool, we could not only see individual suspended nanotubes in real time, but characterize their crystal structure and transfer them to a target substrate with high spatial precision. We took advantage of this unique capability to perform thermal transport measurements on a carbon nanotube, using sections of graphene as a all-in-one electrical contacts, heaters, and thermometers for either end of a short nanotube "bridge."

1.2 Electrical conductivity, thermal conductivity, and thermopower

The simplest way to characterize a material using transport experiments is to measure its resistance. When the electronic transport is diffusive, we quantify resistances of materials by applying a current through or voltage gradient across a material and measuring the resulting voltage or current. Formally, we write this as Ohm's law, $\vec{j} = \sigma\vec{E} = -\sigma\nabla V$, where $\vec{j}$ is the electrical current density, σ is the electrical conductivity, and ∇V is the voltage gradient, with corresponding electric field $\vec{E}$. In the hydrodynamic regime discussed above, this simple relationship acquires a more complicated dependence on the current density (for example, a highly-viscous fluid may be governed by the Stokes equation[28], $\eta\nabla^2\vec{j} = n^2e^2\nabla V$, where η is the viscosity, n is the charge carrier density, and e is the electron charge). However, Ohm's law provides a good starting point for classifying the behavior of many materials.

In a diffusive transport regime, electrons do not just carry charge; they also carry heat, and have a tendency to flow along thermal gradients from hot regions to cold ones. In the same spirit as Ohm's law, we can semi-classically define a matrix $\mathbf{L}$ that relates electrical and heat currents $\vec{j}$ and $\vec{j}^q$ to voltage and temperature gradients ∇V and ∇T[29,30]:

$$\begin{pmatrix} \vec{j} \\ \vec{j}^q \end{pmatrix} = \begin{pmatrix} L_{11} & L_{12} \\ L_{21} & L_{22} \end{pmatrix} \begin{pmatrix} -\nabla V \\ -\nabla T \end{pmatrix}. \tag{1.9}$$

In the absence of a temperature gradient, $\nabla T = 0$, then $\vec{j} = -L_{11}\nabla V = -\sigma\nabla V$, so we recover Ohm's law and see that $L_{11} = \sigma$. If we do not allow electrical current to flow, $\vec{j} = 0$, but allow (or apply) a temperature gradient $\nabla T \neq 0$, then $\nabla V = -(L_{12}/L_{11})\nabla T$, which we use to define the thermopower:

$$S = -\frac{\nabla V}{\nabla T}. \tag{1.10}$$

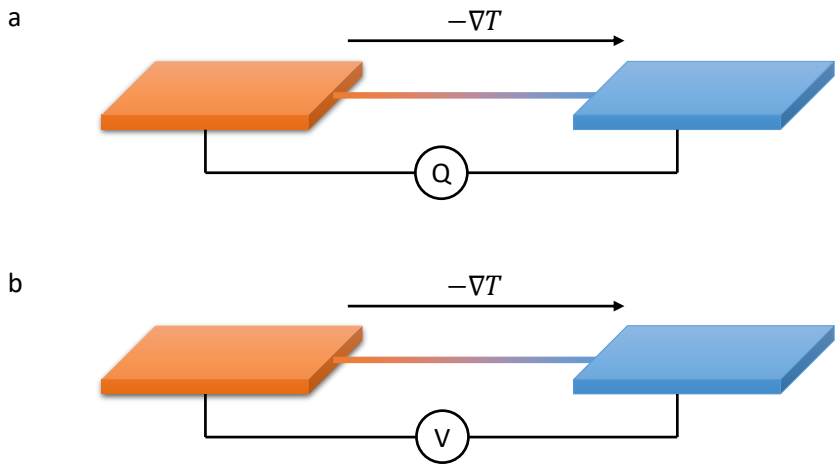

Figure 1.3: (a) Schematic of thermal conductivity measurement: electrons or other excitations carry a heat current Q from a hot thermal reservoir to a cold reservoir. (b) Thermopower measurement: a thermally-induced voltage is generated across a material subject to a temperature gradient.

This also gives us $L_{12} = -S\sigma$. From Onsager's reciprocal relations[31] (discussed in more depth in Chapter 2), the off-diagonal coefficients of the matrix are related by $L_{21} = -L_{12}T$, which means $L_{21} = S\sigma T = \Pi\sigma$, where Π is known as as the Peltier coefficient. Finally, L_{22} describes the proportionality between electronic heat current and the temperature gradient, which means L_{22} must be the electronic thermal conductivity κ_e. We can put this all together to write

$$\begin{pmatrix} \vec{j} \\ \vec{j}^{q} \end{pmatrix} = \begin{pmatrix} \sigma & -S\sigma \\ \Pi\sigma & \kappa_e \end{pmatrix} \cdot \begin{pmatrix} -\nabla V \\ -\nabla T \end{pmatrix}. \tag{1.11}$$

For weakly-interacting electronic systems that are described by Fermi liquid theory, an intriguing correlation between electronic and heat currents was empirically observed in 1853 by Wiedemann and Franz[32] and later more rigorously formalized as the Wiedemann-Franz (WF) law using quantum theory[29]:

$$\frac{\kappa}{\sigma} = \frac{\pi^2}{3}\left(\frac{k_B}{e}\right)^2 T = L_0 T, \tag{1.12}$$

where k_B is the Boltzmann constant. This defines the Lorenz number $L_0 = \frac{\pi^2}{3}\left(\frac{k_B}{e}\right)^2$. The WF law may not hold in strongly-interacting systems, when the Fermi liquid quasiparticle picture cannot accurately describe the electronic behavior. Significant examples of non-Fermi liquid physics leading to a breakdown of the WF law include quasi-one-dimensional materials[33], cuprate superconductors[34], and the charge-neutral point of graphene[18]. For low-dimensional materials like graphene and carbon nanotubes, electronic thermal transport measurements are an equally important counterpart to charge transport measurements, as their ability to probe charge-neutral excitations can reveal important details about the nature of their strongly-correlated states[35,36].

Often, measuring electronic thermal transport is difficult because thermal conductivity is frequently dominated by phonons[37,38]. Creative experimental approaches have thus been required, such as measurements of the thermal Hall effect[33], or measuring particular mesoscopic systems such as single-electron transistors[39] and quantum Hall systems[35] and exploiting known thermal properties of these systems for electronic thermometry. Later, we will discuss quantum Hall thermometry, which can be used to determine the temperature gradients for thermopower measurements, as described in Chapter 4. For low-dimensional systems, conventional techniques such as the incorporation of thermocouples into devices are unfeasible because the electronic contribution to thermal transport cannot be isolated from its phononic counterpart using these methods[37]. Johnson noise thermometry in a novel multiterminal geometry was developed to measure electronic thermal conductivity in graphene and other low-dimensional materials[37,40,41]. For the experiments described in Chapter 3, we applied this technique to carbon nanotubes.

Aside from thermal conductivity measurements, we can use slightly more conventional techniques to study the interplay of electronic charge and energy transport via the thermopower S. When thermopower is only generated by electronic diffusion due to a temperature gradient, we can semiclassically derive a relationship between the electrical conductivity and the thermopower,

known as the Mott formula[29,42]:

$$S_{Mott} = -\frac{\pi^2}{3e} k_B^2 T \frac{1}{\sigma} \frac{d\sigma}{dE}\bigg|_{E_F}, \tag{1.13}$$

where E_F is the Fermi energy. We can immediately note several features of the thermopower: it is predicted to be linearly proportional to temperature T if $\frac{1}{\sigma}\frac{d\sigma}{dE_F}$ is T-independent, and it depends on the derivative of the electrical conductivity evaluated at the Fermi energy. This makes it a highly sensitive probe of the electronic structure of a system. The Mott formula relies on several assumptions, most particularly the "relaxation time approximation," which is that the form of the non-equilibrium distribution function does not affect the distribution of electrons emerging from collisions or their collision rate[29,43]. While this is generally true for elastic collisions (typical of electron-impurity scattering), electron-electron or electron-phonon scattering can produce inelastic collisions, which can cause violations of the Mott formula. Electron-electron scattering can be extremely important in graphene, including for a special regime of electronic transport: hydrodynamics.

1.3 Graphene hydrodynamics

The framework of hydrodynamics provides a universal description of how an interacting system comes to thermal equilibrium[5], achieved by coarse-graining our viewpoint to sufficiently long length and time scales. On the microscopic level, a body of water is made up of H_2O molecules interacting with each other. Solving the Schödinger equation for all the the molecules in a tablespoon of water (just under 1 mole—5×10^{23} molecules) is clearly intractable, yet we can understand the dynamics of how that water will behave reasonably well. This is possible because our fluid dynamics equations (and our typical experiences with water) only deal with water on length and time scales much larger than those of their intermolecular interactions. As a result, we can develop an effective theory that only needs to deal with relatively simple conserved quantities such as particle number

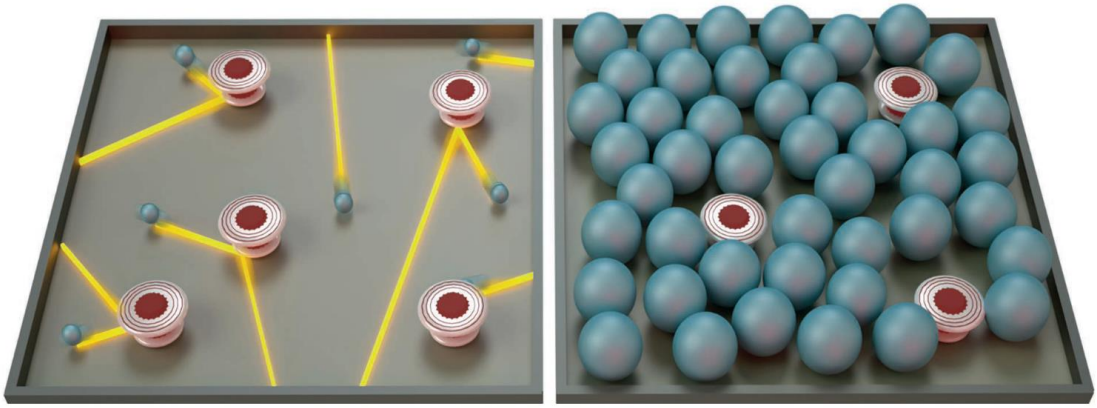

Figure 1.4: Illustration of different electronic flow regimes. In conventional Ohmic metals (left), electrical current flows due to electrons (blue balls) moving independently and occasionally scattering from impurities in the crystal (red and white sites). In a normal fluid or an electronic system in the hydrodynamic regime (right), the constituent molecules or electrons frequently collide with each other, equilibrating in a way described by the theory of fluid dynamics. Adapted from Ref. 44.

and total energy and momentum.

The initial development of fluid dynamics was to describe classical fluids, but in general the assumptions of statistical mechanics do not radically change for quantum microscopic degrees of freedom. Under the right conditions, we should also be able to describe electrons as behaving like a hydrodynamic fluid (Figure 1.4). Like the case of water molecules, the hydrodynamic theory for electrons will apply at length (l) and time (τ) scales larger than those for electron-electron scattering: $l > l_{ee}$ and $\tau > \tau_{ee}$, where l_{ee} and τ_{ee} are the electron-electron scattering length and electron-electron scattering time, respectively*. In condensed-matter systems, we must also consider the role of electrons scattering (and potentially relaxing their energy and momentum) from other sources: impurities (l_{imp}, τ_{imp}), phonons (l_{eph}, τ_{eph}), and the edges of the device (l_W, τ_W). A hydrodynamic description truly applies when electron-electron scattering is the predominant source of momentum and

*l_{ee} and τ_{ee} are linked via the relation $l_{ee} = v_F \tau_{ee}$, so they may be discussed somewhat interchangeably.

energy relaxation on the microscopic level: $l_{imp}, l_{eph}, l_W \gg l_{ee}$ (and similarly for $\tau_{ee}, \tau_{imp}, \tau_{eph}, \tau_W$). Although the application of hydrodynamic theory to condensed-matter systems has been considered since the mid-20th century[45], realization was limited by the difficulty of creating a sufficiently clean and interacting system, and relatively few successful experiments[46] were performed in subsequent decades.

Graphene turns out to be an ideal system for electron hydrodynamics in many ways, and advances in quality and fabrication techniques rejuvenated the field. Encapsulation in hBN[8,9] can dramatically reduce scattering from charged impurities on the substrate[47], so l_{imp} can be hundreds of nanometers. The small Fermi surface of graphene is also helpful because it corresponds to a shorter electron-electron scattering time[5†] and reduces Umklapp scattering (scattering into the next Brillouin zone, which is far away if the Fermi surface is small). As mentioned in Section 1.1.1, direct backscattering is also unfavorable due to pseudospin-momentum locking. These two factors extend the timescale for momentum relaxation. Electron-phonon scattering has been measured to be small[48], in contrast to semiconductor quantum wells. Different modes of electron scattering may dominate the momentum relaxation and thermalization in certain regimes; electron-electron scattering generally scales $\propto T^2$ or T in the Fermi liquid and Dirac fluid regimes, respectively[5], while electron-phonon scattering scales $\propto T^4$ or T depending on whether the temperature is below or above the Bloch-Grüneisen temperature (below which the momenta of phonons is restricted)[48], and electron-impurity scattering is relatively constant with temperature[5]. These scalings show that it is possible to open a hydrodynamic "window" in clean graphene at moderate temperatures[49], where electron-electron interactions will dominate the thermalization and the mesoscopic behavior may resemble a viscous fluid.

We aimed to study graphene hydrodynamics by taking inspiration from a classic fluid dynamics problem: Couette flow[50]. This describes the motion of a viscous fluid between parallel plates, one

[†] $\tau_{ee} \sim \frac{1}{\alpha^2} \frac{\hbar E_F}{(k_B T)^2}$ or $\sim \frac{1}{\alpha^2} \frac{\hbar}{k_B T}$ in the Fermi liquid and Dirac fluid regimes, respectively; $\alpha \sim 1$.

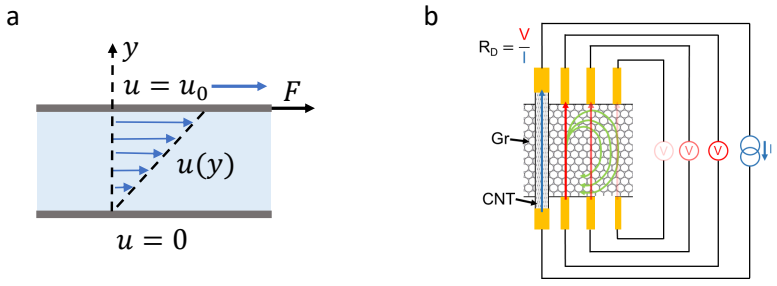

Figure 1.5: (a) Schematic of Couette flow. (b) Illustration of formation of drag current whirlpools due to viscous flow of electrons in graphene being stimulated by drag due to current in nanotube, with distance-dependent Coulomb drag measurement. Adapted in part from Ref. 14.

of which is stationary and the other of which moves at constant velocity, causing a velocity gradient in the bulk of the fluid (Figure 1.5(a)). In our carbon nanotube-graphene drag device, which will be discussed in Section 2.2, the charge carriers in the nanotube are analogous to the moving plate, imparting momentum to the graphene electrons via Coulomb drag. We could then examine the distance dependence of the drag resistance (Figure 1.5(b)) for signs of viscous electron flow. Before further discussion of the theory of Coulomb drag, we should introduce the quantum Hall effect. This regime of 2D physics in graphene has been intensely studied using Coulomb drag[51,52], and quantum Hall transport is also a key element of the experiments described in Chapter 4.

1.4 The quantum Hall effect in graphene

Graphene in a perpendicular magnetic field has long be known to host interesting quantum phases, primarily related to the quantum Hall effect[22,53,54,55]. At the simplest (non-interacting) level, the charge carriers in graphene or another 2DEG in the quantum Hall regime are organized in Landau levels (LLs), which are flat bands with energies[16]

$$E_n = \mathrm{sgn}(n)\hbar v_F\sqrt{2|n|eB/(\hbar c)}, \tag{1.14}$$

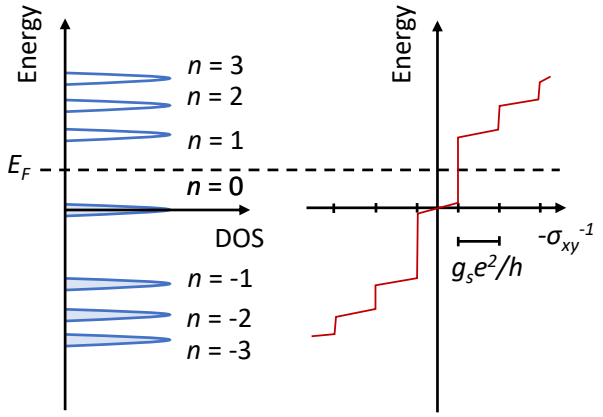

Figure 1.6: Schematic of Landau level density of states (left) and corresponding quantized Hall conductance σ_{xy} (right) in graphene, as a function of energy. LL index n is indicated next to each level. For the Fermi energy E_F shown, the filling factor $\nu = 2$. Adapted from Ref. 22.

where $v_F \approx 1 \times 10^6$ m/s is the Fermi velocity, $n = 0, \pm 1, \pm 2...$ is the electron-like ($n > 0$) or hole-like ($n < 0$) LL index, and B is the applied perpendicular magnetic field. Importantly, graphene hosts a LL with $n = 0$ at zero energy ($E_{n=0} = 0$). In the regime where the LL width broadening is larger than the Zeeman spin splitting, the degeneracy of each LL is $g_s = 4$, with a factor of two each from spin and sublattice degeneracy. Figure 1.6 shows the density of states of the g_s-fold degenerate LL spectrum and corresponding quantized Hall conductance σ_{xy}, which plateaus when the Fermi energy E_F is tuned between LLs and changes by $g_s e^2/h$ when E_F crosses a LL [22]. Graphene is a special quantum Hall system due to its robust $n = 0$ LL, which remains fixed at $E_0 = 0$ for all magnetic fields if sublattice symmetry (also called chiral symmetry) is preserved [23,56]. Chiral symmetry dictates that an eigenstate ψ_E of the (graphene) Hamiltonian, with energy E, has a "chiral partner" $\psi_{-E} = \Gamma\psi_E$ with energy E, where Γ is a chiral operator that flips the sign of the wavefunction for one of the two sublattice components [23]. As such, states at zero energy have chiral partners at the same energy, which creates topological protection for the $n = 0$ LL against broadening of the flat bands that occurs due to disorder in real quantum Hall systems. This property was described for

more generic systems at zero energy in a perpendicular magnetic field by Aharonov and Casher[57]. The quantization of σ_{xy} therefore follows[22]

$$\sigma_{xy} = \nu \frac{e^2}{h}, \ \nu = g_s(n + 1/2), \tag{1.15}$$

where we have defined the "filling factor" ν in accordance with convention for quantum Hall systems. The typical sequence of σ_{xy} in graphene has $\nu = \pm 2, 6, 10\ldots$, though in high-quality samples at higher B, spin and sublattice degeneracies start to lift and other integer and fractional ν can be observed[55]. The quantized conductance can be understood by the flat band electron-like ($n > 0$) LLs being forced to bend sharply upward at the edges of the sample due to the interface with vacuum (Fig. 1.7(a)). Each occupied LL that crosses the Fermi level generates a conducting state at the edge, contributing e^2/h to the conductance. Since electrons in a band described by potential $U(y)$ (as a function of position y) have velocities $v \propto dU(y)/dy$, and the slope of the bending LL is positive on one edge and negative on the opposite edge, the edge currents on opposite edges of the sample travel in opposite directions and are said to be chiral (Fig. 1.7(b)). Since the bands in the bulk of the sample are completely occupied, and any available states (with opposite momentum) are on the opposite side of sample, both small-angle and large-angle scattering are suppressed in quantum Hall systems, leading to zero longitudinal resistance R_{xx} in quantum Hall plateaux of Hall resistance R_{xy}[58]. This edge state picture can become substantially more complicated, particularly in the fractional quantum Hall regime[59,60] but still serves as a useful basis for understanding the behavior.

Thermopower in a quantum Hall system is also different than the diffusive electron regime. With an applied temperature gradient ∇T across a sample, the Fermi distribution $f(\varepsilon)$ of the charge carriers traveling from the hotter side to the colder side will more thermally broadened compared to that of the edge state moving from the colder side to the hotter side (Fig. 1.7). This means there are more occupied states above the Fermi level, so the magnitude of the warmer edge state is larger

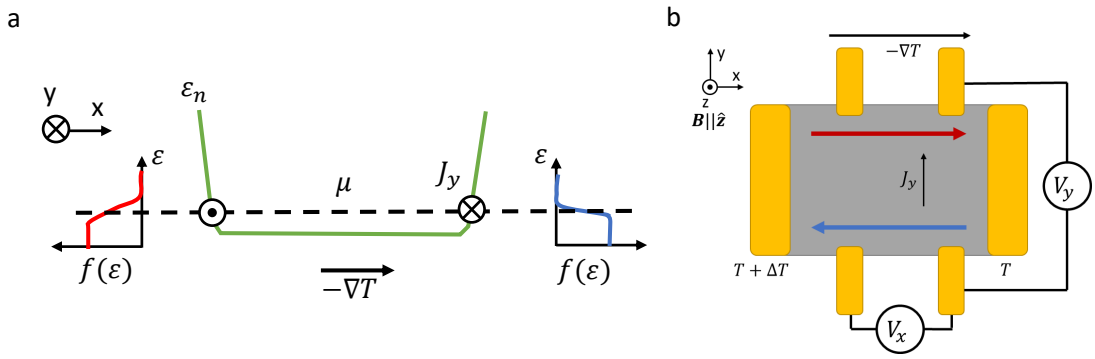

Figure 1.7: (a) Schematic of the effect of a temperature gradient $-\nabla T$ on a quantum Hall system ($n \neq 0$). The energy of a LL (green curve) is constant in the bulk and increases sharply at the edges of the sample, generating edge currents when crossing the chemical potential μ (dashed line). If there is a temperature gradient ∇T, the Fermi distribution $f(\varepsilon)$ of the charge carriers moving from the hotter side of the sample (red curve on left) will be thermally broadened compared to the edge state traveling from the colder side (blue curve on right). (b) Schematic of thermopower measurement in the quantum Hall regime. Adapted from Ref. 61.

than that of the cooler edge state, generating a thermoelectric signal. This difference should give rise to peaks in the longitudinal thermopower that are quantized according to $S_{xx} = -\Delta V_x/\nabla T = (k_B e/h)\ln(2)/\nu$[62], which has been approximately observed in graphene outside of the $n = 0$ LL[43,61].

There are many more possible avenues for discussion of thermopower in the quantum Hall regime in graphene, but we were primarily interested in using it as a probe of more unusual physics, the Sachdev-Ye-Kitaev (SYK) model[63,64]. This model describes a highly-entangled many-body quantum system in which all of the constituent excitations (which are either spinless fermions[63] or Majorana fermions[64]) are at the same energy and have random, all-to-all interactions. It has been held up as an example of possible correspondence between theories of condensed matter and quantum gravity[65], and also holds interest as a window into strange metals and quantum chaos[66]. In Chapter 4, we will explore the theoretical prediction that the SYK model can be realized in the $n = 0$ LL of a random-edged graphene quantum dot, and our electrical and thermoelectric transport measurements attempting to probe this regime.

Coulomb interactions generate a plethora of novel emergent phenomena in condensed-matter systems, particularly when electronic confinement to fewer than three spatial dimensions increases the relative strength of potential to kinetic energy[5]. We will close this chapter by introducing Coulomb drag, an important experimental tool for studying interaction-driven effects in low-dimensional systems.

1.5 Coulomb drag in graphene

When a current is driven in a conductor that is near but electrically isolated from another, Coulomb interactions between the charge carriers in the two conductors generate a voltage drop in the "passive" conductor[52,67,68,69]. The drag resistance is thus a direct probe of interlayer charge carrier interaction. Most of the past theoretical and experimental efforts have focused on drag between 2D conductors, such as electrons confined in semiconductor heterointerfaces[68,69] and graphene[51,52,70], revealing several new emergent phenomena including exciton condensation under strong magnetic fields[52]. Drag experiments have also been performed between 1D conductors[71,72,73], showing signatures of Wigner crystal and Luttinger liquid behavior.

In a system of two conductors with independent electrical contacts, small interlayer separation d and minimal charge transfer or tunneling between the two conductors, driving a current I_{drive} in one layer can induce a voltage V_{drag} in the other layer as a result of Coulomb interactions between the charge carriers in each layer[67]. The drag resistance is defined as $R_{drag} = V_{drag}/I_{drive}$, and is zero in the absence of interlayer interaction. The temperature, charge carrier density, and magnetic field dependence of R_{drag} can provide insight into the nature of the carriers, their interactions, and their environment.

The simplest mechanism for Coulomb drag to arise in two Fermi liquid conductors at finite temperature T is momentum transfer due to electron-electron scattering[67], illustrated in Figure 1.8.

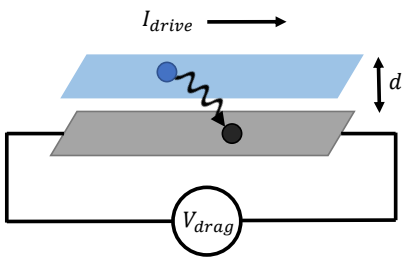

Figure 1.8: Schematic of Coulomb drag in a 2D-2D system. Charge carriers in drive layer transfer momentum, energy, or both to charge carriers in the drag layer, causing a voltage V_{drag} to develop.

Moving electrons in the "drive layer" transfer some of their momentum to the electrons in the "drag layer" via interlayer Coulomb scattering, so they start moving in the same direction. With open-circuit conditions in the drag layer, an electric field builds up to counter this "frictional force," and the corresponding voltage is measured as V_{drag}. Using the Drude model, we can describe the drag resistivity ρ_{drag} caused by this force as[67]

$$\rho_{drag} = \frac{m_{drag}}{e^2 n_{drive} \tau_D}, \tag{1.16}$$

where m_{drag} is the effective mass of the carriers in the drag layer, n_{drive} is the carrier density in the drive layer, $-e$ is the electron charge, and τ_D is the characteristic timescale for interlayer momentum transfer. τ_D can be calculated using the linearized Boltzmann formalism[67,74], leading to a more detailed expression for the drag:

$$\rho_{drag} = \frac{\hbar}{e^2} \frac{\pi^2 \zeta(3)}{16} \frac{T^2}{E_{F1} E_{F2}} \frac{1}{\aleph_1 \aleph_2 k_{F1} k_{F2} d^4}, \tag{1.17}$$

where $\zeta(3) \approx 1.202$, $E_{F1(2)}$ are the Fermi energies of the two layers, $\aleph_{1(2)}$ are the inverse Thomas-Fermi screening length in each layer, and $k_{F1(2)}$ are the Fermi wavevectors. There are some limits to

when this equation applies: we require small interlayer separation d compared to the mean free path in both layers, relatively strong screening (typically expressed as $\aleph d \gg 1$), and low temperature ($T \ll E_F/(k_F d)$).

Looking at Equation 1.17, we can gain some intuitive understanding of how the drag resistance will behave. First, $\rho_{drag} \propto T^2$, which makes sense as the drag is proportional to the electron-electron scattering rate and the phase space available for scattering increases with temperature[29]. The inverse dependence on E_F, k_F, and $\aleph$ can be understood by thinking of importance of carrier density fluctuations relative to the total carrier density. With increasing numbers of carriers in either layer, intralayer screening will compete with the interlayer drag, so ρ_{drag} is larger at lower carrier densities. The dependence on the interlayer distance d is also notable; the two conductors should be very close (as noted above) to observe an appreciable drag effect. Finally, the sign of ρ_{drag} depends on the relationship between current and momentum. If current is carried by charge carriers with the same sign (e.g. electrons) in both layers, the electric field needed to counteract the induced drag current will be in the opposite direction, so the measured ρ_{drag} will be negative. On the other hand, if electrons in the drive layer are transferring momentum to holes in the drive layer, the drag current will flow in the opposite direction and ρ_{drag} will be positive.

The first Coulomb drag experiments in semiconductor quantum wells[68,69] showed good agreement with this interlayer momentum transfer picture, particularly the T^2 dependence of the drag resistance and an interwell-spacing dependence consistent with d^{-4} scaling. For double graphene heterostructures, deviations from this theoretical model were noted[51,70], including the carrier sign dependence. In the next section, we discuss graphene-based drag experiments in more detail.

1.5.1 Previous experiments on Coulomb drag in graphene-based systems

Coulomb drag between two graphene layers was first experimentally studied in 2011[70], with the graphene layers separated by a 7 nm-thick layer of Al_2O_3 and the carrier densities in the two layers

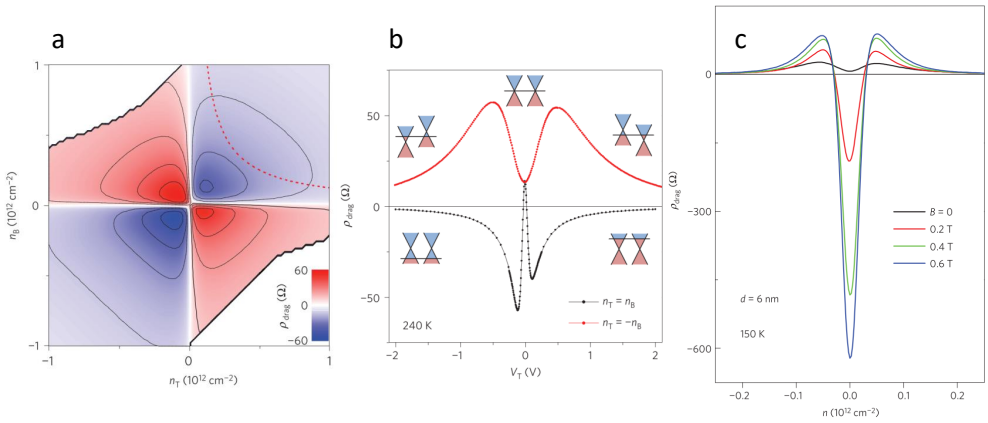

Figure 1.9: (a) ρ_{drag} as a function of n_B and n_T. Black lines are isolevels every 12Ω. (b) Line cuts of ρ_{drag} at equal carrier densities in both layers, $n_T = n_B$ (black) and $n_T = -n_B$ (red). Data are plotted versus top gate voltage V_T; bottom gate voltage V_B was simultaneously varied to realize the stated density conditions. Dirac cone diagrams illustrate different doping regimes. (c) Evolution of ρ_{drag} with applied perpendicular magnetic field. Adapted from Ref. 51.

tuned by a global bottom gate. This was soon followed by measurements of Coulomb drag between two graphene flakes encapsulated by thicker flakes of hexagonal boron nitride (hBN) and separated by a trilayer of hBN (1 nm thick), with separate gates to tune the carrier densities of each layer[51]. We can immediately see from the device geometry why graphene-hBN heterostructures are an attractive system for Coulomb drag experiments. The possible interlayer separations are on the order of a few nanometers, smaller than what can be achieved in semiconductor double quantum wells (typically tens or hundreds of nanometers)[68,69], while still keeping the two graphene layers electrically isolated, so the interlayer interactions can be much stronger. As mentioned above, the carriers can be continuously tuned from electrons to holes through the charge neutrality point via electrostatic gating, an impossibility in typical semiconductor heterostructures, allowing regimes of drag beyond the Fermi liquid regime to be explored.

The early graphene-graphene drag experiments found drag behavior consistent with interlayer momentum transfer when there was an appreciable carrier population in both layers (see Fig. 1.9(a)).

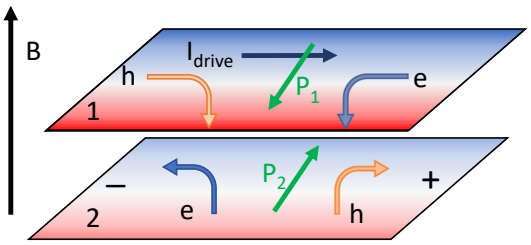

Figure 1.10: Schematic of energy drag for two graphene layers at charge neutrality. Transfer of temperature gradients between the drive layer (labeled 1) and drag layer (labeled 2) causes momentum transfer (green currents P_1 and P_2 in each layer) and thus charge transport in the drag layer, enhanced by perpendicular magnetic field. Figure based on Refs. 75 and 76.

The expression for the drag resistivity in this regime can be written as[70]:

$$\rho_{drag} = -\frac{h}{e^6}\frac{\zeta(3)}{32}\frac{(k_B T)^2}{d^4}\frac{\varepsilon^2}{n_B^{3/2} n_T^{3/2}}, \tag{1.18}$$

where k_B is the Boltzmann constant, ε is the dielectric constant of the insulating spacer layer, and $n_{B(T)}$ is the carrier density in the bottom (top) graphene layer. However, this model fails to completely capture the experimental observations of drag near the charge neutrality point (CNP). Given the $n^{-3/2}$ dependence for each layer, one might expect the magnitude of the drag resistivity to peak very close to the CNP, and go to zero exactly at the CNP, as there is no net carrier population and thus should be no way to transfer net momentum between the layers. In fact, a positive drag response was observed at the double charge neutrality point[51] (Fig. 1.9(b)), which has a non-monotonic temperature dependence, and became negative and extremely large with the introduction of a perpendicular magnetic field (Fig. 1.9(c)). Perhaps unsurprisingly, the Dirac fluid completely breaks the picture of Coulomb drag built up in the Fermi liquid regime.

Explaining this unusual behavior requires a new addition to the theory for Coulomb drag in graphene: energy drag[76,77,78]. The essential idea is that energy as well as momentum can be trans-

ferred from the drive layer to the drag layer, and spatial inhomogeneity in the carrier density can then cause charge and energy to redistribute in the drag layer. Strain and nearby charged impurities[51] can create local fluctuations in the carrier density. These are particularly noticeable near zero density, where they form "charge puddles" of electrons and holes. Although this inhomegeneity is greatly mitigated by hBN encapsulation[47], it remains a potentially significant factor for the physics of real graphene devices. When the length scale of the charge puddles, D, is small compared to the interlayer distance d, charge puddles form independently in each layer and energy drag is not significant. However, if $d \ll D$, the charge puddles in the two layers become spatially correlated (or anti-correlated, depending or whether they are predominantly caused by strain or disorder[77]) due to the interlayer Coulomb interaction. Driving a charge current in charge-neutral graphene can create a temperature gradient due to electron-hole friction. In strongly coupled graphene layers, this temperature gradient can be transferred from the drive layer to the drag layer much faster than the electrons can dissipate energy to the lattice[76]. The carriers in the drag layer then tend to equilibrate the thermal distribution, moving from hotter regions to colder ones regardless of carrier type. Since the drag layer carriers were initially (anti-)correlated with the carriers in the drive layer, the drag signal becomes positive (negative) even at the double CNP. In a magnetic field (Fig. 1.10), this tendency is further enhanced by the Nernst effect, leading to longitudinal and Hall energy drag signals[75,76].

Applying a perpendicular magnetic field also raises the more complicated question of Coulomb drag in the quantum Hall regime. One of the major motivations for Coulomb drag experiments has been the prospect of realizing an exciton condensate[67]. Excitons are bound electron-hole pairs, which typically recombine and annihilate if formed in a single conductor. However, if the electron and hole are in different layers and thus unable to recombine, these bosonic quasiparticles are much longer-lived. Like other bosons, they can form a condensate at low temperatures[79]. A condensate of magneto-excitons has been studied using double-layer graphene heterostructures in the quantum Hall regime[52,79,80], using Coulomb drag and similar measurements to explore the exciton interac-

tions. Evidence for exciton condensates has also been shown in heterostructures of van der Waals semiconductors[81]; Coulomb drag measurements may be a useful probe of their properties as well.

Coulomb drag experiments between mixed-dimensional systems, e.g. 1D-2D conductors, have also been conceived[82,83] to investigate the effects of dimensionality on electron-electron interactions. Such a system was recently probed experimentally[84] using an InAs nanowire as 1D conductor and graphene as 2D conducting layer. This recent 1D-2D drag experiment shows an anomalous temperature and density dependent drag response that might be related to energy drag[76,77,78] due to the large mismatch in thermal conductivities between InAs and graphene. However, the breakdown of layer (Onsager) reciprocity and subsequent thermopower measurements in these devices[85] suggest thermoelectric effects induced by local heating may also play a substantial role in the reported drag results. We note that these thermoelectric phenomena are nonlinear in the drive current, unlike energy drag, which is a linear effect. The role of these mechanisms in our carbon nanotube-graphene Coulomb drag measurements will be discussed in the next chapter.

Life need not be easy, provided only that it is not empty.

Lise Meitner

2

Carbon nanotube-graphene Coulomb drag

The concept of Coulomb drag can be intuitively grasped, and in the ideal case, measuring the drag between two strongly-coupled conductors seems like it should be very similar to a conventional electronic transport measurement (since scattering between charge carriers in the two layers can be theoretically described very similarly to intralayer scattering, but with a different effective interaction[67]). In reality, preventing spurious signals such as interlayer gating[69] and accounting for

contributions to the measured drag voltage in addition to typical Coulomb drag required careful efforts. One of the largest challenges proved to be fabricating 1D-2D heterostructures with an individual, metallic carbon nanotube, a thin hBN spacer layer, and encapsulated monolayer graphene. In this chapter, we will further develop the theory for Coulomb drag between a single-walled carbon nanotube and graphene, discuss its application to the study of graphene hydrodynamics, and present the results of our nanotube-graphene drag experiments.

2.1 Theory for nanotube-graphene Coulomb drag

We studied Coulomb drag in a new 1D-2D conducting system, a metallic single-walled carbon nanotube and monolayer graphene separated by an atomically thin (2-4 nm) insulating barrier of hBN. Since carbon nanotubes and graphene have similar linear dispersion relations with comparable Fermi energies and work functions [16,86], the interaction-driven momentum and energy transfer between carriers in separate layers are enhanced, which should amplify the drag signal.

The few theoretical studies of Coulomb drag in 1D-2D systems [82,83] have mostly focused on what could be achieved in conventional semiconductor heterostructures. More recently, theoretical work by Badalyan and Jauho [87] extended this framework to drag between a single carbon nanotube and graphene. They found that the mixed dimensionality of the system (in particular, the additional confinement of the momentum in the carbon nanotube) led to distinctive temperature, carrier density, and inter-conductor spacing dependence compared to the double graphene heterostructures. The degree of screening also plays a substantial role. Considering the general form

$$\rho_{drag} \propto \frac{T^{\alpha}}{n_{1D}^{\beta_1} n_{2D}^{\beta_2}}, \tag{2.1}$$

where n_{1D} and n_{2D} are the carrier densities of the nanotube and graphene, and the exponents $\beta_1 = 1, \beta_2 = 0.5$ to 1.5 depending on the degree of electrostatic screening, and $\alpha \sim 3.7$ at low tem-

peratures, transitioning to $1 < \alpha < 2$ at higher temperatures (the exact temperature scale for this transition depends on the doping level). For semiconducting nanotubes, the temperature dependence is similar, although the exact exponent depends on the interlayer spacing. Interestingly, ρ_{drag} has a kink in its density dependence (for both n_{1D} and n_{2D}); this occurs because backscattering is not suppressed in semiconducting nanotubes, and becomes particularly appreciable at lower n_{1D} as screening is reduced.

This model assumes that both conductors are in the degenerate limit (that is, $E_F \gg k_B T$); thus the applicability of this theory to our devices is somewhat limited. In reality, as the discussion in the previous chapter illustrates, the Coulomb drag response in graphene-based systems is often strongest at or near the charge neutrality point, where one or both conductors become non-degenerate. In order to understand our experimental data, we also drew on theory for graphene-graphene Coulomb drag[88] in the Fermi liquid and Dirac fluid regimes, which will be discussed further in Section 2.8 in the context of our results.

2.2 Coulomb drag as a potential probe of hydrodynamics in graphene

Beyond intrinsic interest in the 1D-2D drag system, why might we try to generate Coulomb drag between a carbon nanotube and graphene? Due to the small ($\sim$ 2 nm) diameter of a single-walled carbon nanotube, driving current in the nanotube provides an extremely localized 1D drag source in the graphene channel. The implications of this for the physics of Coulomb drag have been discussed above, but it also creates a possible opportunity to use the carbon nanotube to probe a different regime of physics in graphene: hydrodynamics. Broader context for why this unusual viscous flow of electrons might be observed in graphene is discussed in Section 1.3.

As we were conducting our nanotube-graphene Coulomb drag studies, other experiments had been recently performed that demonstrated highly viscous electronic behavior in the Fermi liquid

regime of graphene[89,90,91]. One important signature of viscous hydrodynamics is the negative potential that develops next to a contact where current is injected; the viscosity causes nearby electrons to be "dragged" along with the injected current. In a confined geometry this can lead to the formation of whirlpools of viscous electron motion[13,28,89]. Measurements at the time relied on directly injecting current into a contact and performing conventional electronic transport measurements (for example, of a negative "vicinity resistance"). Ohmic, or more typical resistive behavior, will compete with the pure hydrodynamic behavior, and stray Ohmic contributions from the injected current may mask the negative vicinity resistance. Another complication is that negative vicinity resistance can also be observed in the ballistic regime[92,93] (when electrons scatter primarily from the edges of the device, rather than with each other), and in general, it has been difficult to distinguish ballistic and hydrodynamic measurements through transport measurements alone. (More recently, scanning probe measurements[20,94] have provided a more detailed look at the hydrodynamic motion of graphene electrons, including in the Dirac fluid regime.)

Our Coulomb drag experiments aimed to study hydrodynamics in a cleaner way than the previous transport work. Due to the 1D confinement of the momentum of electrons in the nanotube, driving a current in the nanotube should be equivalent to injecting a straight line of current into the graphene, without any parasitic stray currents that appear in conventional transport measurements. Measuring the dependence of the drag resistance on distance from the nanotube would ideally enable us to detect a negative vicinity resistance or other signs of unusual conduction as signatures of hydrodynamic behavior. Our results ultimately revealed that Coulomb drag between carbon nanotubes and graphene is a complex phenomenon in its own right. While hydrodynamics may still play a role in our devices, the interplay of electronic and thermoelectric effects and significant contributions from disorder meant that our primary efforts were directed at understanding how Coulomb drag evolves in this mixed-dimensional system.

2.3 Drag device fabrication

To briefly describe the device geometry, monolayer graphene is encapsulated in hBN and then transferred on top of a metallic single-walled carbon nanotube (SWNT). The hBN flake separating the SWNT and graphene is 2-4 nm thick, so that the two conductors are sufficiently close together for interlayer Coulomb interactions, but they remain electrically isolated, without a significant tunneling current. The graphene and SWNT have individual electrical contacts, allowing them to be characterized separately. Many aspects of the device fabrication process are described elsewhere, particularly in Refs. 14, 95.

2.3.1 SWNT synthesis, characterization, and transfer

Carbon nanotubes are grown in a chemical vapor deposition (CVD) furnace using the method described in [96]. The growth substrate is a 5 mm $\times$ 5 mm silicon chip with a slit in the center (Fig. 2.2(a)), oriented perpendicular to the gas flow direction. A cobalt-molybdenum-based catalyst is applied to the chip on the side of the slit nearer to the gas inlet, so that nanotubes grow suspended across the slit thanks to buoyant forces caused by the combination of a parabolic gas flow profile in the tube furnace and heating of the growth chip [97]. Suspended nanotubes were located and characterized using Rayleigh scattering spectroscopy [96] and imaging (Fig. 2.2(d)). By matching peaks in Rayleigh scattering intensity with nanotube optical transition energies, the chiral indices (and thus diameter and metallic/semiconducting nature) of the nanotube can be determined (Fig. 2.2(c)). The scattered light is also routed to a camera, providing an image of the nanotube spanning the slit (Fig. 2.2(b)). All the SWNTs used in devices described in this paper were metallic. The Rayleigh scattering spectroscopy, imaging and transfer stage is described in more detail in Appendix C.

Electron beam (e-beam) lithography was used to define a $\sim$ 50 $\times$ 50 μm resist-free window on a SiO_2/p-doped Si chip coated with $\sim$ 100 nm of 495 K Polymethyl methacrylate (PMMA) A4 re-

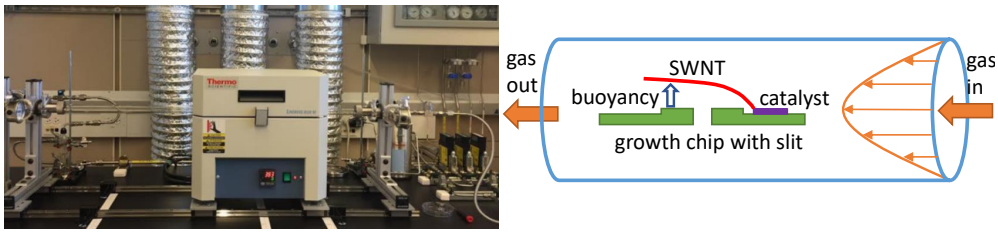

Figure 2.1: Picture of CVD furnace for nanotube growth and schematic of suspended nanotube growth mechanism (adapted from Ref. 97).

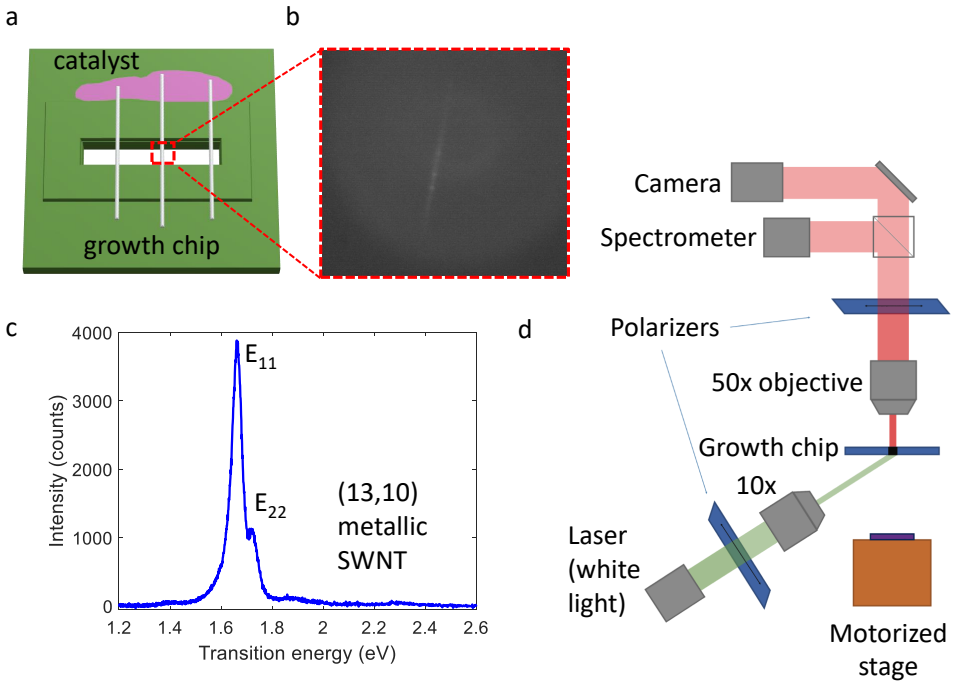

Figure 2.2: Nanotube suspended growth, imaging and characterization. (a) Schematic of nanotube growth chip with catalyst and central slit. (b) Infrared image of suspended SWNT. (c) Optical excitation spectrum of an example metallic SWNT. (d) Schematic of Rayleigh spectroscopy, imaging and transfer stage setup.

sist. The resist layer helps the SWNTs transfer to the chip[98]. When a single SWNT with the desired characteristics has been located, it is aligned with the heterostructure so that it crosses the center of the PMMA window (Fig. 2.3(a-b)). The growth chip and PMMA-coated sample are pressed together until mechanical contact is evident (Fig. 2.3(c)]), then heated to 180 °C for 5 minutes to soften the resist. The chips are then cooled to 90 °C and slowly separated (Fig. 2.3(d)). Successful SWNT transfer is confirmed by scanning electron microscope (SEM) or atomic force microscope (AFM) imaging. The same PMMA window can be reused several times in the event of unsuccessful transfer, or to transfer multiple SWNTs for parallel device fabrication. Finally, the PMMA is removed by high-temperature annealing in vacuum.

To anchor the SWNT to the substrate and confirm its suitability to be incorporated into a device, electrical contacts were made to either end of a 30-50 μm section of the SWNT, inside the window region (Fig. 2.3(e)). The mask for the contacts was defined by e-beam lithography, and metal was deposited by e-beam evaporation (10 nm Cr/60 nm Au). Many other recipes for high-quality SWNT contacts have been reported in literature, including some measurements with quantum-limited contact resistance[99,100,101,102]. However, this recipe was found to remain the most reliable through the additional fabrication steps.

2.3.2 Graphene-hBN heterostructure fabrication and transfer

Boron nitride-encapsulated graphene heterostructures were prepared using standard techniques[8,9]. The top hBN flake (20-40 nm) is picked up with a polypropylene carbonate (PPC) film on a Polydimethylsiloxane (PDMS) stamp, and then used to pick up graphene and bottom hBN (2-5 nm) flakes. It was critical to ensure that the bottom hBN flake was both thin and large enough to completely cover the graphene (at least in the region intended to be near the SWNT), in order to allow interaction between the graphene and SWNT without electrically shorting. Once assembled on a stamp, the stack was transferred on top of a contacted SWNT (Fig. 2.3(f-g)). The PPC and stack

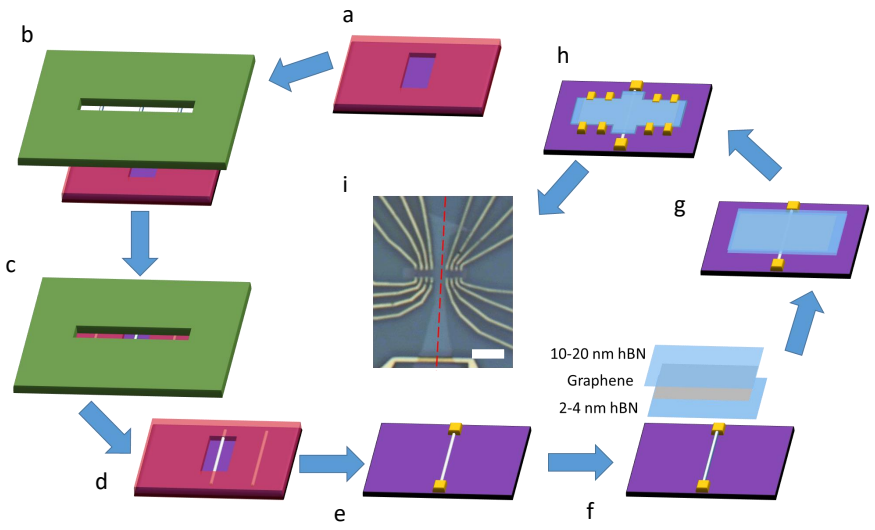

Figure 2.3: Fabrication sequence for SWNT-graphene devices. (a) PMMA window for SWNT transfer. (b) Alignment of growth chip with CNTs to window. (c) Mechanical contact between growth chip and target chip. (d) Growth chip removal; SWNTs are captured by PMMA. (e) PMMA removal and patterning/deposition of SWNT contacts. (f-g) Transfer of hBN and graphene flakes to contacted SWNT. (h) Heterostructure shaped by etching, patterning/deposition of graphene contacts. (i) Optical microscope image of a final device, with SWNT position indicated by red dashed line. Gold electrode at bottom of image is one of the SWNT contacts. Scale bar is 2 μm.

were detached from the stamp by heating to 150 °C to melt the PPC, which was then removed by high-temperature vacuum annealing.

2.3.3 Additional nanofabrication

Following stack transfer, the heterostructure was shaped into a bar (with additional extended regions above the SWNT to avoid etching it) by reactive ion etching the heterostructure with CHF_3 through a resist mask defined by e-beam lithography. A second lithography step defined the graphene contact electrodes (Fig. 2.3(h)), which were made by reactive ion etching to expose a clean graphene

edge, and then depositing a metallic trilayer (2 nm Cr/8 nm Pd/50 nm Au) using thermal evaporation (as described in Ref. 9). An optical micrograph of an example nanotube-graphene device is shown in Fig. 2.3(i), and a scanning electron microscope image of the same device in Fig. 2.4(a).

We briefly note that it is possible to invert the order of the layers in the SWNT-graphene heterostructure, so that the hBN-encapsulated graphene is placed on the substrate first, and then a CNT is transferred on top. This improves the quality of the graphene by enabling the use of a thicker hBN layer between the graphene and the SiO_2. However, the extremely low friction between SWNTs and clean hBN can result in the SWNT bending and shifting from the intended transfer position, sometimes shorting to exposed parts of the graphene or breaking due to stress in fabrication. In contrast, transferring the SWNT to SiO_2 pins the SWNT to the rougher substrate, and allows for screening out poorly-conducting SWNTs before transferring a stack. It was thus found to be a more reliable fabrication method, although the yield of working devices after SWNT transfer was still low due to poor electrical contact to the SWNT (or generally high SWNT resistance), SWNTs breaking during stack transfer, and the thin, bottom hBN flake shifting or cracking during stack transfer and allowing the graphene to short the SWNT.

2.4 Coulomb drag measurements

While we focus on one device in most of following discussion, numerous SWNT/graphene devices were measured, and similar results were obtained. Additional data can be found in Appendix A. Measurements of the drag resistance were performed by applying DC current I_{drive} through the drive layer (SWNT or graphene) while the voltage V_{drag} was measured in the drag layer (graphene or SWNT). Example data for both configurations are presented in Figure 2.4(b). When using the SWNT as drive layer, V_{drag} in graphene is typically measured with the voltage probes nearest the SWNT, at a distance $x = 800$ nm away (closed circles). At temperature $T = 300$ K, there is a linear

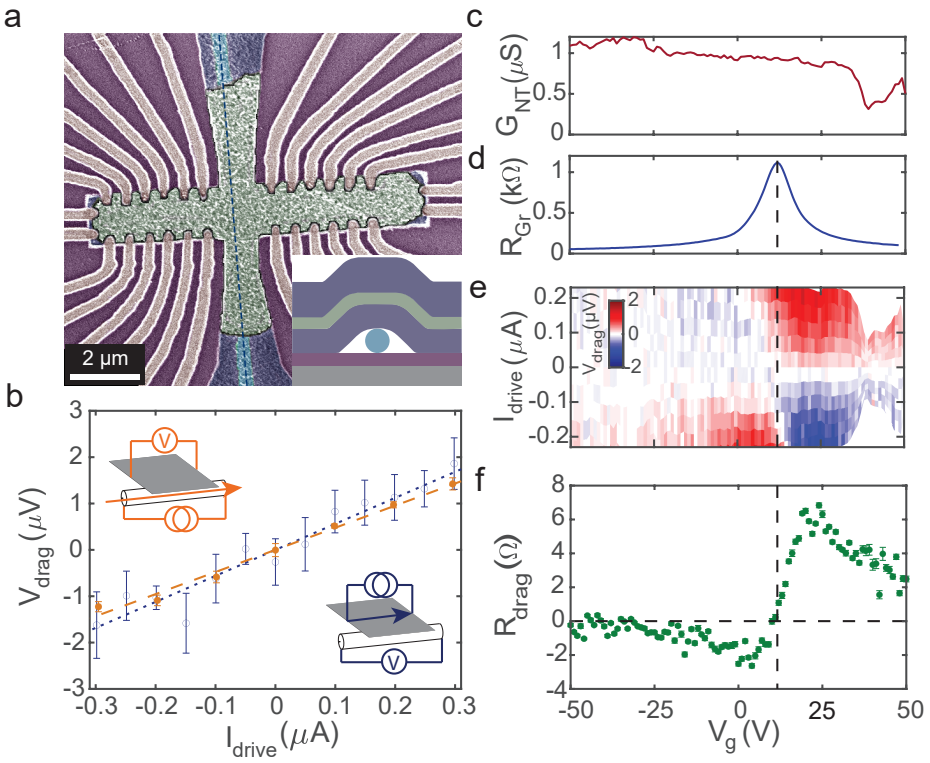

Figure 2.4: (a) False color scanning electron microscope image of a typical SWNT-graphene drag device. Graphene (green) is encapsulated in hBN (dark blue) and transferred on top of a metallic SWNT (dashed line in center of blue charged region). Electrical contacts (gold) are made to the graphene and SWNT. Inset: cross-section schematic of the device. (b) V_{drag} versus I_{drive} for reciprocal layer configurations: nanotube-drive, graphene-drag (orange, filled symbols) and graphene-drive, nanotube-drag (blue, open symbols). Data were taken at $T = 300$ K and $V_g = 21$ V, with averaging gate voltage window $\Delta V = \pm 1$ V to enhance the signal-to-noise ratio. Dashed curves are lines of best fit. (c) SWNT conductance as a function of gate voltage. The dip is a local conductance minimum, not the charge neutrality point. (d) Graphene resistance as a function of gate voltage. (e) V_{drag} in graphene versus SWNT I_{drive} and V_g. (f) R_{drag} versus V_g. Dashed line marks zero drag signal.

relationship between I_{drive} and V_{drag}, whether the SWNT or the graphene channel is the drive layer. Using the graphene as the drive layer and measuring V_{drag} across the SWNT (open circles) results in a noisier signal than the reciprocal drag scheme, due to the higher resistance of the SWNTs. Even so, both biasing configurations yield the same current-voltage relationship. This Onsager reciprocity when drive and drag layers are exchanged demonstrates that the system is in the linear response regime,[103,104] allowing the extraction of the drag resistance from the slope: $R_{drag} = \Delta V_{drag}/\Delta I_{drive}$.

In our devices, the SWNTs are beneath the graphene (Fig. 2.4(a) inset), enabling the carrier densities in both SWNT and graphene to be tuned by a voltage V_g applied to the p-doped silicon back gate across the 285 nm SiO_2 dielectric layer. Figure 2.4(c) and (d) show the conductance G_{NT} of SWNT and resistance R_{Gr} of graphene, respectively, as a function of V_g measured at $T = 300$ K. The gradual decrease of G_{NT} as V_g increases indicates the SWNT is hole-doped, as discussed further in the next section.. In the graphene, R_{Gr} exhibits a peak corresponding to the charge neutrality point (CNP) around gate voltage $V_0 = 13$ V. We also measure the drag response as a function of V_g, as shown in Figure 2.4(e). We extract R_{drag} in the linear response regime in as a function of V_g, as described above. For $V_g < V_0$, V_{drag} and I_{drive} have opposite sign, while for $V_g > V_0$, they have the same sign. As shown in Figure 2.4(f), R_{drag} thus changes sign at $V_g = V_0$ where the dominant carrier type in graphene switches from electrons to holes. This behavior is qualitatively similar to previous measurements of momentum-transfer Coulomb drag in double-layer graphene systems,[51,70] as discussed in Section 1.5.1. The higher magnitude of e-h compared to h-h drag can be attributed to the higher density of holes in the SWNT at more negative gate voltages. Due to heavy SWNT doping, the k_F's of the SWNT and graphene do not overlap within our experimental gate window, preventing us from investigating the double neutrality point, where the chiral nature of the 1D-2D Dirac system can be explored[105].

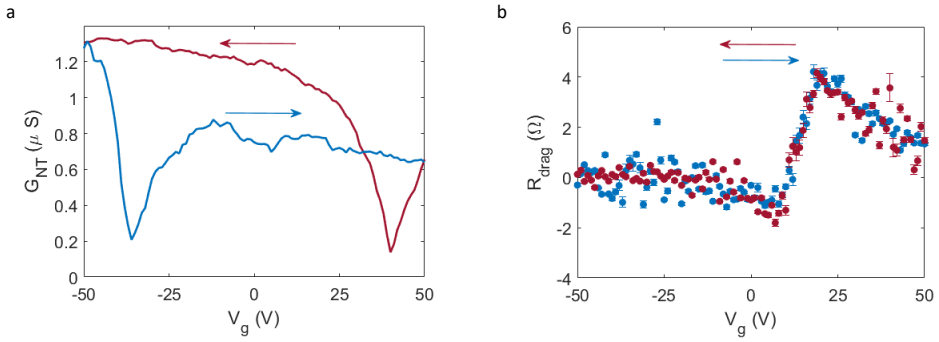

Figure 2.5: (a) Conductance of the SWNT in device D1 at $T = 200$ K as a function of gate voltage. Arrows indicate direction of V_g sweep; positive to negative (red) and negative to positive (blue). (b) R_{drag} measured simultaneously with the SWNT conductance in (a).

2.4.1 SWNT CONDUCTANCE

I will pause the discussion of results at this point to highlight a few technical points that are key to understanding the results. First, a brief note on the transport behavior of the SWNTs in our devices. As shown in Fig. 2.4(c), the conductance of the SWNT decreases with increasing gate voltage V_g, characteristic of a hole-doped nanotube. There is also a notable dip in the conductance around $V_g = 40$ V. While at first this may appear to be the charge neutrality point of the metallic SWNT, it was found to shift its position depending on the direction of the gate voltage sweep, as shown in Fig. 2.5. However, the overall SWNT conductance away from the dip generally decreased with increasing V_g, regardless of the gate sweep direction. Furthermore, the drag resistance measured during the same gate voltage sweeps does not change polarity when the SWNT conductance dip is on the left side of the graphene CNP as opposed to on the right (Fig. 2.5(b)). We therefore conclude that the SWNT appears to remain hole-doped at all accessible V_g values. The most likely origin of this conductance dip shift is doping from charges on the substrate, which are reconfigured as the silicon gate is kept at a particular voltage (as before the start of a gate sweep) and then swept. Since the nanotube rests directly on the SiO_2, it is more susceptible to this disordered electrostatic

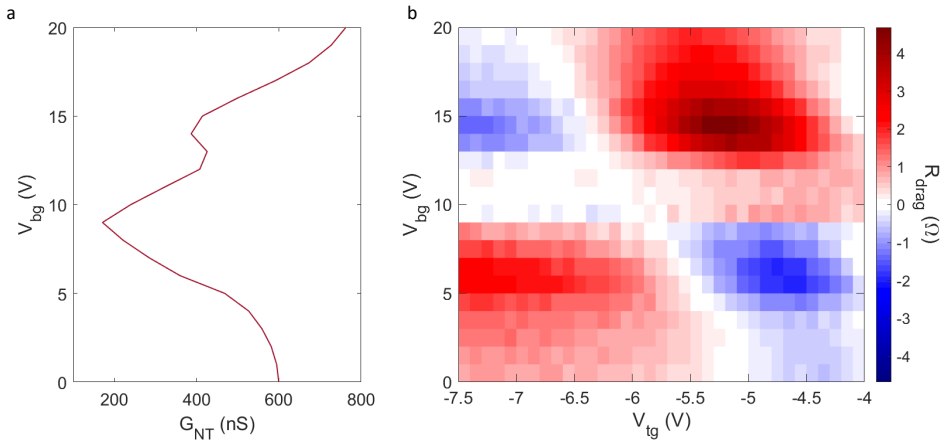

Figure 2.6: (a) SWNT conductance as a function of back gate voltage in a SWNT-BLG device (axes flipped to align with (b)). (b) Drag resistance as a function of back gate and top gate voltages.

environment than an encapsulated conductor, such as the graphene layer. The uncertainty in the nanotube CNP position is incorporated into estimates of the SWNT Fermi energy plotted in Fig. 2.9(b) below. More details of the calculation are in Section 2.7.

Due to the high hole density in the SWNT, the Fermi wavevectors of the SWNT and graphene are significantly mismatched when the drag signal is maximized near the graphene CNP (see Section 2.8 for further discussion of drag mechanisms). We could not independently tune the SWNT and graphene carrier densities effectively due to the small breakdown voltage of the thin separating hBN dielectric. Although the increased electron-electron scattering phase space when $k_F^{Gr} = k_F^{NT}$ may generically lead to an enhancement R_{drag}, we expect that the high k_F where this would occur would mean the Coulomb interaction is already quite suppressed, reducing the drag signal.

In some devices, we do observe a change in the polarity of the drag resistance on either side of a dip in SWNT conductance. We provide an example in a double-gated SWNT-bilayer graphene

(BLG) drag device, also used to estimate capacitance ratios in Section 2.7. Figure 2.6(a) shows the SWNT conductance tuned by the back gate (the top gate has almost no effect on the SWNT, as it is generally screened by the graphene) and (b) is a color plot of drag resistance as a function of back gate and top gate voltages. There is a clear sign reversal with both the graphene CNP (tuned by both top and back gates and thus diagonal on this plot) and SWNT conductance dip (tuned only by the back gate). This allows us to say with some confidence that, in this device, the SWNT conductance dip is in fact the CNP. Extensive measurements were performed in SWNT-BLG devices (some results are presented in Ref. 14, 106), but the vast majority of data were dominated by heating-induced nonlinear thermoelectric effects rather than Coulomb drag. There were significant nonlinear effects in some of the SWNT-monolayer graphene drag devices as well, which will be discussed in Section 2.5.

2.4.2 DC drag measurement technique

Low-frequency AC measurements are a standard technique for electrical transport experiments, including many Coulomb drag and other double-layer measurements (e.g. Refs. 52, 107). However, drag measurements are sensitive to parasitic effects that can obscure the behavior that truly arises from interlayer charge carrier interactions.[68,69] For example, when a bias is applied to the drive layer to initiate current flow, the layer acquires a non-zero potential due to contact and layer resistances of the drive layer, which may cause an asymmetric gating effect on the drag layer. This is particularly problematic for AC measurements, since the alternating potential on the drive layer can capacitively couple to the drag layer and generate an alternating current, which can cause a spurious alternating voltage signal in the drag layer due to its contact and layer resistances.[69]

The interlayer potential can be manually adjusted to approximately zero using resistance bridges.[68,69] However, as the gate voltage is changed during the measurement, the layer resistances change substantially, unbalancing the bridge circuit. Another problem in our system is the disparity in contact

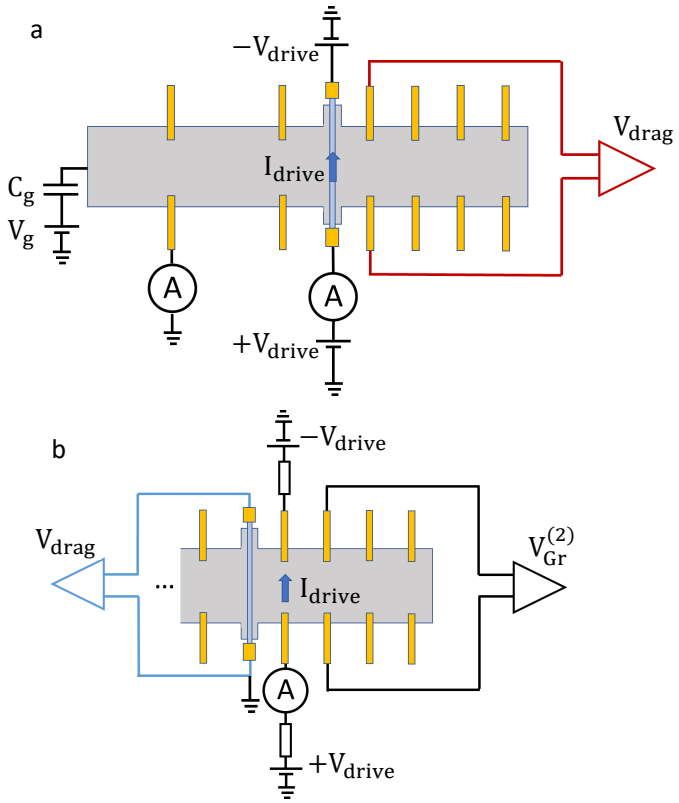

Figure 2.7: Circuit diagrams for DC measurement. (a) Schematic of symmetrically biased SWNT (drive layer) and voltage measurement on graphene (drag layer). Additional ammeters on SWNT and graphene can measure the SWNT conductance and SWNT-graphene tunneling current, respectively. (b) Symmetrically biased graphene (drive layer) and voltage measurement on graphene (to estimate graphene resistance) and SWNT (drag layer). In this case, large ($\sim$ 10 MΩ) resistors are added after the voltage sources so that the graphene is being current biased.

resistances between the graphene and SWNT; while graphene contacts typically have resistances on the order of 100 Ω, the lowest SWNT resistances we achieved in these devices were $\sim$ 100 kΩ. This renders the SWNT-graphene drag devices very susceptible to interlayer bias effects.

DC measurements avoid introducing spurious signals from capacitive coupling but are more sensitive to noise and must be carefully monitored to ensure the signal in the drag layer is not simply originate from local heating-induced thermoelectric effects, as addressed in the following section. To circumvent these issues, we performed our measurements by symmetrically DC biasing the

drive layer, applying $\pm V_{drive}/2$ to either side of the SWNT or to a pair of contacts in the graphene (adding a pair of resistors in series to limit the current; the resistor values can be modified, or an additional resistor inserted, to account for differences in contact resistance) and measuring the resulting I_{drive}. The circuits are shown in Figure 2.7. The value of V_{drive} (and thus I_{drive}) is swept through a range of values (typically $V_{drive} = 0.3\ \text{V} \rightarrow -0.3\ \text{V}$ on one contact, and $-0.3\ \text{V} \rightarrow 0.3\ \text{V}$ on the other) multiple times, and the detected V_{drag} values at each I_{drive} were averaged to reduce noise. The error for each displayed V_{drag} data point is calculated using the standard error on the mean: $\sigma_{\bar{x}} = \sigma/\sqrt{n}$, where $\bar{x}$ represents the average of a population of measurements, σ is the standard deviation, and n is the number of independent measurements.

2.5 Nonlinearity and breaking Onsager reciprocity

Since Coulomb drag is a linear process, it is important to check that the drag voltage we measure is linear in the drive current. An equivalent test is to exchange whether the same drag resistance is obtained when the drive and drag layers are exchanged (i.e. comparing R_{drag} for current driven in the SWNT and voltage measured at a particular pair of voltage probes in the graphene with R_{drag} for current driven between the same pair of probes in the graphene and voltage measured across the SWNT).

The underlying idea of this test is Onsager's principle of microscopic reversibility, also called Onsager reciprocity,[31,103,104] or layer reciprocity in the specific context of Coulomb drag.[51,76,78] For a system in local thermodynamic equilibrium that has some generalized forces $\nabla\mathbf{f}$ (in this case the voltage) that are conjugate to currents $\mathbf{J}$, we can write

$$\mathbf{J}_\alpha = \sum_\beta \mathbf{L}_{\alpha\beta} \nabla \mathbf{f}_\beta, \tag{2.2}$$

where $\mathbf{L}$ is a matrix of transport coefficients. An example that may be familiar is Fourier's law for

heat conduction, $\mathbf{j}^q = -\kappa \nabla T$ ($\mathbf{j}^q$ is the heat current density and κ is the thermal conductivity),[29] or Ohm's law for electrical conduction, $\mathbf{j} = -\sigma \nabla V$ ($\mathbf{j}$ is the electrical current density and σ is the electrical conductivity), as discussed in Chapter 1. Onsager's reciprocal relations state that the matrix $\mathbf{L}$ is symmetric when time-reversal symmetry holds ($\mathbf{L}_{\alpha\beta} = \mathbf{L}_{\beta\alpha}$), which is true in the linear response regime without an applied magnetic field (which breaks time reversal symmetry). In the case of a Coulomb drag system, the conjugate force and current are ∇V_{drag} and I_{drive} and α, β represent the two conductors. Although it is counterintuitive in a mixed-dimensional device, Onsager reciprocity should still hold in the linear response regime.

While we observed a linear drag response at room temperature, the relationship between drive current and drag voltage in our device becomes increasingly nonlinear as T decreases (Fig. 2.8(a)). To quantitatively address this change, we fit V_{drag} with a 3rd-order polynomial in I_{drive}: $V_{drag} = I_{drive} R_{drag} + \gamma I_{drive}^2 + \eta I_{drive}^3$, where γ and η are fitting coefficients. The nonlinear effect sensitively varies with V_g; Figure 2.8(b-c) shows the V_g dependence of γ and η at several fixed temperatures. We find that $\gamma > 0$ and $\eta < 0$ for all gate voltage ranges we probe, and both quantities have larger magnitude nearer the CNP of graphene ($V_g \approx V_0$) and at lower temperatures. This increasingly nonlinear effect also breaks Onsager layer reciprocity at low temperatures. As shown in Figure 2.8(d) and (e), the drag resistance from SWNT-drive and graphene-drive configurations show progressively worse correspondence at lower temperatures, as the nonlinear part of the relation between I_{drive} and V_{drag} becomes appreciable.

Higher-order dependence of V_{drag} on I_{drive} is best explained by development of a temperature gradient in the SWNT due to the Peltier effect or Joule heating, which can be efficiently transferred to the nearby graphene[76,77,78]. Such a temperature gradient in the graphene generates a thermoelectric voltage and causes a temperature-dependent change in R_{drag}. Both can give rise to nonlinear terms in V_{drag}.

To describe this relationship in more detail, we first note that driving current I_{NT} in the SWNT

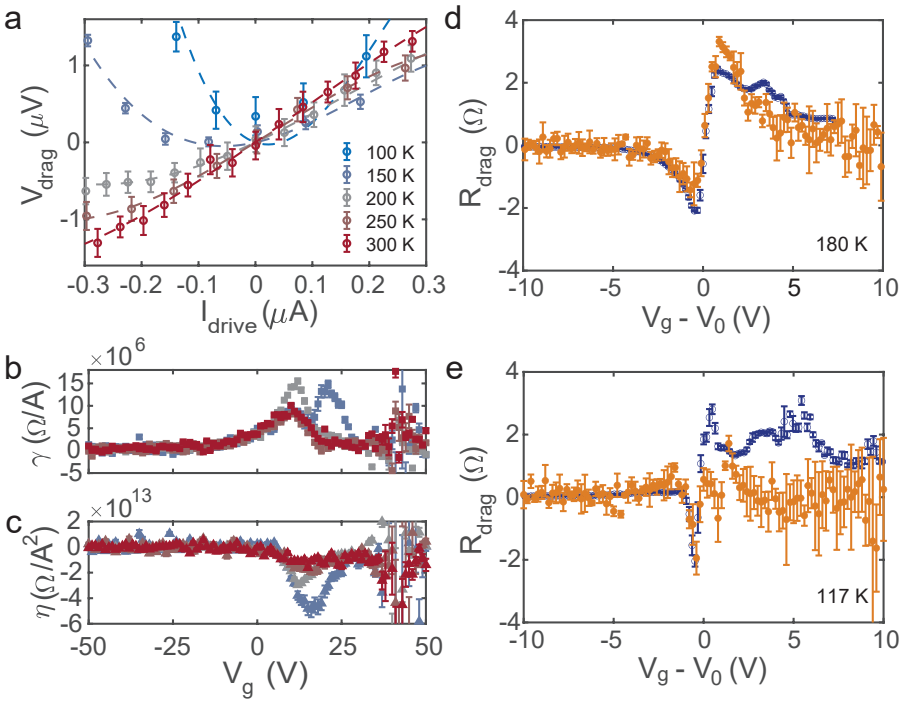

Figure 2.8: (a) V_{drag} versus I_{drive} at $V_g = 22$ V for varying temperatures. Dashed lines are 3rd-order polynomial fits. (b) 2nd-order coefficient versus V_g. (c) 3rd-order coefficient versus V_g. Regions of noisy data in (b) and (c) are due to SWNT local conductance dip limiting I_{drive}. (d) R_{drag} from linear fit versus V_g (subtracting the graphene CNP voltage) for reciprocal configurations at $T = 180$ K (same colors and symbols as Fig. 2.4(b)). (e) Same measurement at $T = 117$ K.

can produce a nonuniform temperature profile due to the thermoelectric Peltier effect ($\Delta T_P \propto I_{NT}$) and Joule heating ($\Delta T_J \propto I_{NT}^2$). As the graphene and SWNT are in close proximity, this temperature profile can be transferred from the SWNT to the graphene above, particularly when the gate voltage is tuned near the graphene CNP[76,77,78]. This energy transfer gives rise to a temperature gradient across the voltage probes in the graphene layer, $\Delta T(x) = \Delta T_P(x) + \Delta T_J(x)$, where x is the distance from SWNT to the voltage probes (fixed for any given pair of probes, and thus omitted in the following analysis).

There are two mechanisms by which ΔT can produce a nonlinear drag response: (i) generation of a thermoelectric voltage $V_{TE}(\Delta T) = -S\Delta T$, where S is the Seebeck coefficient of graphene and $\Delta T \propto I_{NT}^2$; and (ii) temperature dependent change in the drag resistance R_{drag} producing a nonlinear drag voltage: $V_{NL}(\Delta T) = \frac{1}{2}\frac{dR_{drag}}{dT}\Delta T I_{drive}$. The thermoelectric voltage $V_{TE}(\Delta T) = -S\Delta T$ is a well-known phenomenon in systems with a thermal gradient[108]. The second nonlinear contribution to the drag voltage, $V_{NL}(\Delta T) = \frac{1}{2}\frac{dR_{drag}}{dT}\Delta T I_{drive}$, merits further discussion.

This expression can be obtained by assuming a small temperature gradient between two voltage probes separated by a distance L. The local drag resistivity ρ_{drag} relates the drag layer local electric field ε and drive current density j_{drive} by $\varepsilon = \rho_{drag} j_{drive}$. Now we consider a small, constant temperature gradient dT/dx between the voltage probes where $x = 0, L$ correspond to the respective electrode positions. The temperature difference between the electrodes is then $\Delta T = L dT/dx$. The drag voltage between them can then be obtained (with T_0 the temperature of the thermal bath):

$$V_{drag} = \int_0^L j_{drive}\rho_{drag}(T(x))dx = j_{drive}\int_0^L \rho_{drag}(T(x))dx \tag{2.3}$$

$$= j_{drive}L\rho_{drag}(T_0) + \frac{1}{2}j_{drive}\frac{d\rho_{drag}}{dT}\frac{dT}{dx}L^2 \tag{2.4}$$

$$= R_{drag}I_{drive} + \frac{1}{2}\frac{dR_{drag}}{dT}\Delta T I_{drive} \tag{2.5}$$

The first term is the typical drag resistance R_{drag} between the voltage probes at $x = 0$ and $x = L$, and the second term is the nonlinear contribution (since $\Delta T \propto I_{drive}$ or I^2_{drive}, as discussed above) due to the temperature dependence of R_{drag}.

Allowing heating by both effects mentioned above, we identify terms contributing to V_{drag} that are proportional to I_{NT} (R_{drag} and $V_{TE}(\Delta T_P)$), I^2_{NT} ($V_{TE}(\Delta T_J)$ and $V_{NL}(\Delta T_P)$), and I^3_{NT} ($V_{NL}(\Delta T_J)$). The I_{NT}-linear thermoelectric response is energy drag, which is observed to be large in graphene systems when both layers are tuned very near the CNP[51,77,78,76], but is otherwise negligible. The presence of both quadratic and cubic nonlinearity in our experimental data, with peaks developed in both $|\gamma|$ and $|\eta|$ at the graphene CNP (see Fig. 2.8(b) and (c)), suggests that, at minimum, the temperature dependence of R_{drag} (i.e. (ii) above) must play a significant role. These effects are significant near the CNP, where $|\frac{dR_{drag}}{dT}|$ exhibits large fluctuations at low temperatures due to disorder (see Fig. 2.8(e)). The nonlinear contribution becomes more appreciable as the linear drag signal diminishes at lower temperature, and in SWNT devices with larger resistance (including contact resistance; see following section for additional data), which also supports the local heating-induced energy transfer picture.

2.6 Carrier density and temperature-dependent drag

To avoid the nonlinear drag phenomena discussed above, we focus on linear drag resistance measured at small drive current at relatively high temperature ($T > 100$ K). Figure 2.9(a) shows R_{drag} as a function of gate voltage V_g, referenced to the CNP of graphene V_0, at different fixed temperatures in this regime. In general, R_{drag} changes sign at the graphene CNP, and that $|R_{drag}|$ grows linearly, peaks, then rapidly decreases as the graphene carrier density, $n_{Gr} \propto V_g - V_0$, increases. Fig. 2.9(b) shows that $R_{drag} \sim (V_g - V_0)^{-\beta}$, where $1 < \beta < 2$ at different temperatures. This behavior resembles 2D-2D graphene drag, where $1 < \beta < 2$ has also been observed[70,51].

Near the CNP of the graphene channel, disorder becomes more relevant, creating charge puddles [109]. The n_{Gr}-dependent conductance of the graphene channel is accordingly expected to saturate at low temperatures for $|n_{Gr}| < \delta n$, where δn is the residual density due to charge puddles, which can be estimated from the temperature-dependent conductance G of the graphene [110]. Figure 2.9(d) shows $G(n_{Gr})$ measured in the graphene channel of our device for $T \lesssim 150$ K. From the saturation of $G(n_{Gr})$ near the CNP, we estimate $\delta n \approx 1.1 \times 10^{10}$ cm^{-2}. For $|n_{Gr}| < \delta n$, the electron and hole contributions of Coulomb drag cancel, resulting in linearly vanishing R_{drag} with n_{Gr} as observed in the experiment (shaded region in Fig. 2.9(a)). We also estimate the puddle energy scale $k_B T_d = \hbar v_F \sqrt{\pi \delta n}$ where $v_F = 10^6$ m/s is the Fermi velocity of graphene. From δn experimentally obtained above, we find the disorder temperature scale $T_d \approx 140$ K, which separates the low temperature regime where disorder effects are dominant and the high temperature regime where thermal broadening is appreciable.

We find the drag near the graphene CNP depends sensitively on temperature. Figure 2.10(a) shows T-dependent R_{drag} at fixed density (reported as n_{Gr}^{bulk}, the upper bound of the estimated graphene carrier density). For $n_{Gr}^{bulk} = \pm 1.3 \times 10^{10}$ cm^{-2}, close to the peak value of $|R_{drag}(n_{Gr}^{bulk})|$, R_{drag} increases linearly in $T - T_d$ in the high temperature regime ($T > T_d$). In the low temperature regime ($T < T_d$), however, the linear response R_{drag} is difficult to determine, due to the nonlinear drag effects and broken Onsager reciprocity discussed above. At larger density (e.g. $n_{Gr}^{bulk} = \pm 8.4 \times 10^{10}$ cm^{-2}, far from the CNP), we observe a similar trend, although $|R_{drag}|$ is reduced. A broader range of the density and temperature dependent $R_{drag}(n_{Gr}^{bulk}, T)$ is shown in Figure 2.10(b), where the magnitude of the drag resistance appears to increase approximately linearly at all densities. For $T > T_d$, the density dependence of $\frac{dR_{drag}}{dT}$ behaves similarly to $R_{drag}(n_{Gr}^{bulk})$ (Fig. 2.10(c)).

The temperature dependent drag behavior discussed above is distinctly different from 2D-2D drag in graphene, where a crossover between $R_{drag}(T) \sim$ constant and $R_{drag}(T) \sim T^{-2}$ is ex-

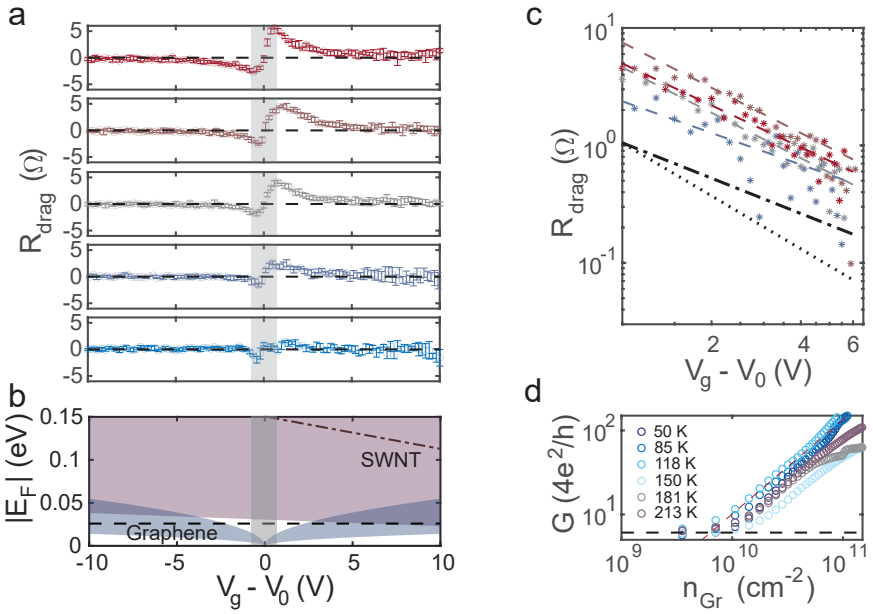

Figure 2.9: (a) Drag resistance as a function of V_g at various temperatures: 265 K (top), 235 K, 200 K, 160 K, 130 K (bottom). Disorder-dominated range is indicated by gray shading. b) Estimated range of Fermi energies for SWNT (purple) and graphene (blue) in a range of V_g near the graphene CNP. Dot-dashed line is approximate center of SWNT E_F range. (c) Log-log plot of R_{drag} versus $V_g - V_0$ at selected temperatures, with $R_{drag} \propto (V_g - V_0)^{-1}$ (dot-dashed) and $R_{drag} \propto (V_g - V_0)^{-1.5}$ (dotted) for comparison. (d) Graphene conductance versus charge carrier density for temperatures in (a). The residual carrier density δn is estimated by the intersection of the line at minimum conductivity (black) and a linear fit to log(G) away from charge neutrality (dark red dashed line shows example fit for $T = 118$ K).

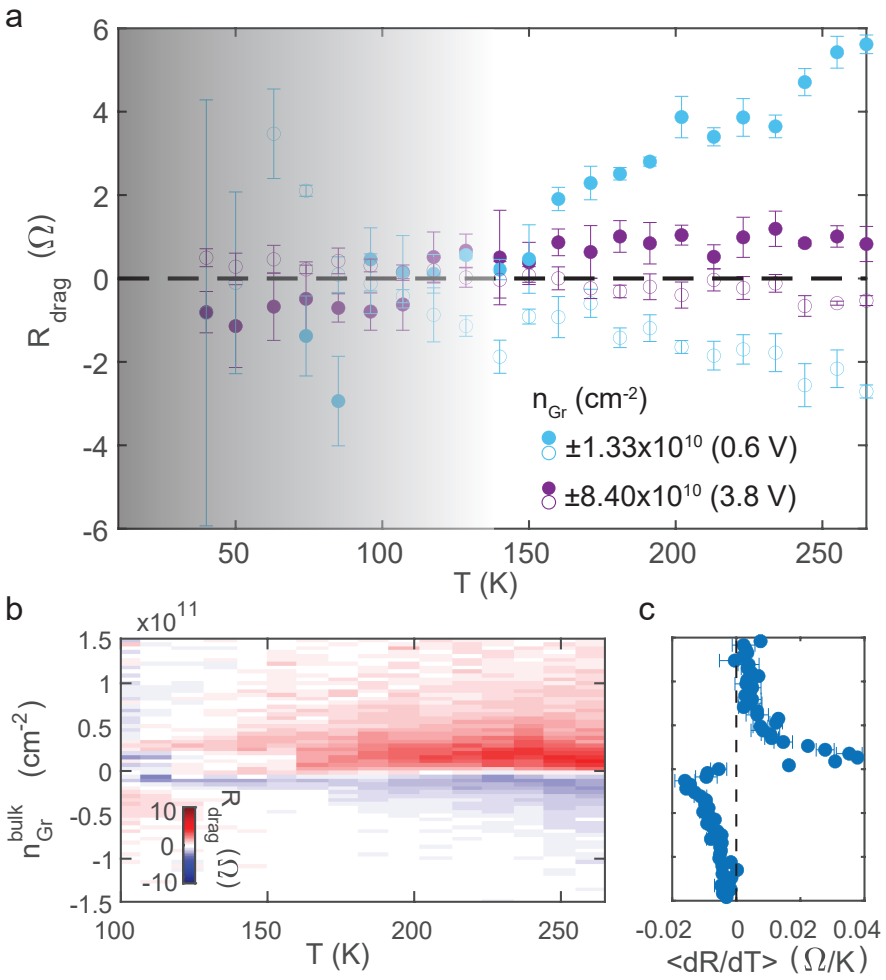

Figure 2.10: (a) Drag resistance as a function of temperature for various graphene charge carrier densities (stated value is the upper bound). For $T < 140$ K (the shaded region in the graph), nonlinear effects increasingly dominate the signal.(b) Drag resistance versus temperature and graphene carrier density. (c) Average $\frac{dR_{drag}}{dT}$ for $T > T_d$ versus temperature at a range of graphene carrier densities.

pected[88] in the parameter range of our experimental regime, $E_F^{Gr} \lesssim k_B T \sim E_F^{NT}$. As we will discuss further in Section 2.8, for 1D-2D drag between a metallic SWNT and graphene, Badalyan and Jauho calculated the Coulomb drag effect in the Fermi liquid regime of both conductors ($k_B T \ll E_F^{NT}, E_F^{Gr}$)[87], predicting $R_{drag}(T) \sim T^{\alpha}$, where $\alpha \approx 3.7$ at low temperatures. A more general theory of 1D-2D drag[83] predicts a transition to $1 < \alpha < 2$ at higher temperatures ($T > T_d$). While a more extensive model extending to the nondegenerate Dirac fluid limit in the presence of disorder is required for further quantitative comparison, our experiments show qualitatively similar behavior in the high temperature limit.

2.7 Estimation of nanotube and graphene carrier densities

To determine the carrier densities (and thus Fermi energies) of each conductor as a function of V_g, we employ a finite element analysis of the graphene channel and SWNT together with the hBN separation layers and silicon back gate (the geometry shown in Fig. 2.4(a) inset). Since the SWNT locally screens the graphene channel from the back gate, the local carrier density in graphene is reduced in the graphene channel directly above the SWNT and maximized away from the SWNT. To estimate the carrier density (and thus chemical potential) of the SWNT, we also need to consider device geometry and quantum capacitance.

Straightforward application of the analytical formulae for capacitance between parallel conducting planes (for graphene-back gate capacitance) or a wire and a ground plane (for SWNT-back gate capacitance) would not adequately account for the electrostatic environment of either the SWNT or graphene. As such, we used COMSOL Multiphysics to perform a finite-element analysis of the gate, conductors, and dielectrics and computed the induced charge on the SWNT and graphene due to an applied gate voltage. Material parameters such as the relative permittivity were found in Refs. 8, 15, 111, 112, 113, 114, 115, 116, 117, 118. Figure 2.11 shows a color map of the electric

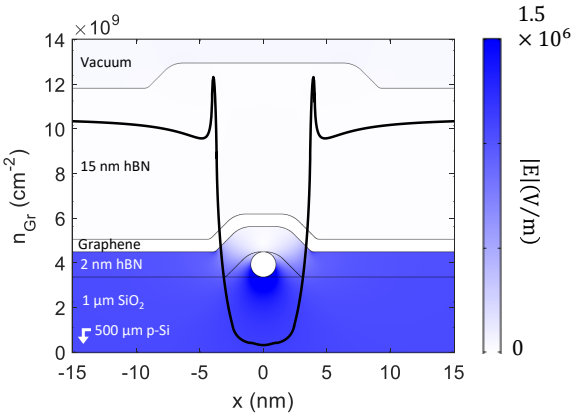

Figure 2.11: COMSOL simulation of SWNT-graphene device. Color map shows $|E|$ with 1 V applied to back gate for a device cross-section. Overlay (black line) shows calculated graphene carrier density n_{Gr} as a function of distance x from the SWNT.

field in this region due to an applied $V_g = 1$ V, along with the resulting charge carrier density in the graphene. The simulation suggests that the local electric field (and thus the local carrier density) is reduced by a factor of ~ 30 in the graphene directly above the SWNT compared to the value predicted from a parallel-plate capacitor model. Due to the local nature of the Coulomb interaction ($\propto r^{-3}$), we expect that this region of decreased carrier density is the part of the graphene that most directly contributes to Coulomb drag. We use the capacitance of this screened region as a lower bound in Fig. 2.9(b), while retaining the analytic "bulk" value as an upper bound (see Fig. 2.12 for equivalent capacitance circuits for both scenarios). Since the area of carrier depletion in the graphene is extremely narrow (the width of this "screening well" is ~ 7 nm, beyond which the graphene carrier density rapidly approaches the value predicted by the analytical model), contributions to drag from higher-n_{Gr} regions could also be important.

The same simulation was used to estimate the capacitance (and thus carrier density) of the metal-

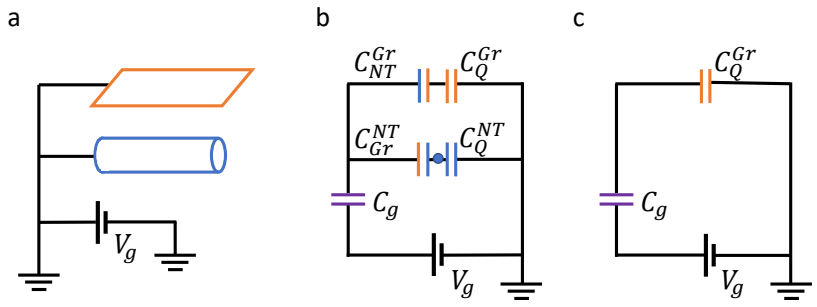

Figure 2.12: Equivalent capacitance circuit of SWNT-graphene device. (a) Schematic of conductors and gate voltage. (b) Circuit for local screening between graphene and SWNT. SWNT-graphene capacitance is illustrated as two capacitors because each conductor screens some of the gate electric field from the other. (c) Circuit for graphene capacitance far from SWNT.

lic SWNT; this is its lower bound in Figure 2.9(b). Since this value may be sensitive to material parameters, such as the dielectric permittivity of the SWNT, the precise magnitudes of which we do not know, we need an alternative approach to validate our calculation and estimate the possible range of the capacitance value. For this purpose, we employ gate dependent data from a SWNT-BLG device (Fig. 2.13(a)). Here the SWNT acts as a local gate on BLG, which was also coupled to a gold top gate and silicon back gate. Since the device geometry is close to the SWNT-monolayer graphene devices in which we measure drag, electrostatic measurements from the SWNT-BLG device allow us to infer the capacitive coupling of the SWNT to monolayer graphene in the drag devices. Particularly, by comparing the effects of the top and back gates on the BLG with the effect of the SWNT gate, we can determine the degree of SWNT-BLG coupling, and therefore how to account for the proximity of the BLG. We then rescale the results to account for the very slightly different geometry of the SWNT-monolayer graphene devices being considered.

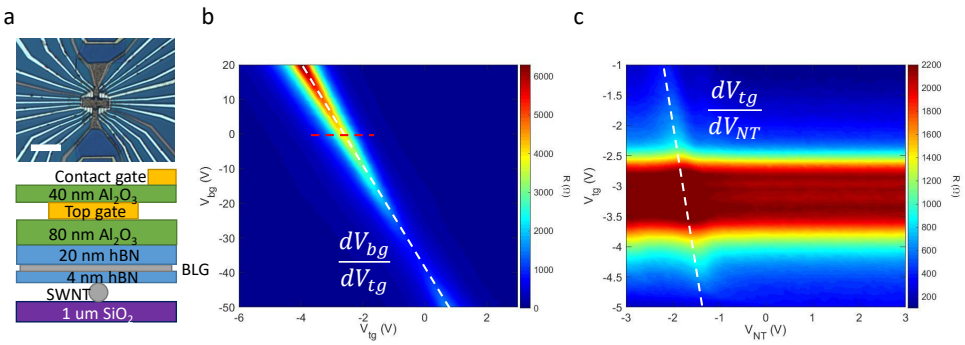

Figure 2.13: (a) Optical microscopy image (upper panel) and cross-section schematic (lower panel) of SWNT-BLG device. Scale bar is 10 nm. (b) BLG resistance as a function of back gate and top gate voltages. Dashed white line follows the charge neutrality point and has slope dV_{bg}/dV_{tg}. Dashed red line indicate back gate voltage (0 V) and top gate voltage range for panel (c). (c) BLG resistance as a function of top gate voltage and SWNT local gate voltage. Dashed white line indicates secondary Dirac peak due to local gating of the BLG by the SWNT and has slope dV_{tg}/dV_{NT}.

For the SWNT-BLG device shown, which has a 4 nm-thick hBN flake separating the SWNT and BLG and 1 μm of SiO_2 between the heterostructure and back gate, the BLG resistance as a function of back and top gate voltages (V_{bg} and V_{tg}) is shown in Figure 2.13(b). The slope of the line tracking the BLG charge neutrality point as the gate voltages are changed, $dV_{bg}/dV_{tg} = -14.66$, quantifies the strength of the capacitive coupling to the top gate compared to the back gate ($dV_{bg}/dV_{tg} = C_{tg}/C_{bg}$). Similarly, tracking the position of the side-peak caused by local SWNT gating while also varying the top gate (Fig. 2.13(c)) gives the relative coupling of the BLG to the SWNT and top gate, $dV_{tg}/dV_{NT} = C_{NT}/C_{tg} = -4.75$.

We can model the effective geometric capacitance of the SWNT to ground as a series combination of back gate and BLG coupling (Fig. 2.12(a-b)):

$$C_{\text{eff}}^{-1} = C_{NT-bg}^{-1} + C_{NT-BLG}^{-1}. \tag{2.6}$$

The first term can be calculated using the formula for wire-plane capacitance per unit length:

$$\frac{C_{NT-bg}}{L} = \frac{2\pi\varepsilon_0\varepsilon_r}{\operatorname{arccosh}\left(\frac{2d_{bg}}{d_{NT}}\right)}, \tag{2.7}$$

where $d_{bg} = 1\,\mu$m is the SiO_2 thickness, $d_{NT} = 2$ nm is the SWNT diameter, and L is the length of the SWNT. The second term is estimated by the experimentally-determined coupling of the BLG to the gate and SWNT:

$$\frac{C_{NT-BLG}}{A} = \frac{C_{bg-BLG}}{A}\frac{dV_{bg}}{dV_{NT}} = \frac{C_{bg-BLG}}{A}\frac{dV_{bg}}{dV_{tg}}\frac{dV_{tg}}{dV_{NT}}, \tag{2.8}$$

where $C_{bg-BLG}/A = \varepsilon_0\varepsilon_r/d_{bg}$ is the standard parallel-plate capacitor formula.

At this point, we must account for the difference in hBN thicknesses between the BLG device (4 nm) and the SWNT-monolayer graphene drag device (2 nm). Noting that the dielectric thickness enters the wire-place capacitance formula as $1/\operatorname{arccosh}(2d_{BN}/d_{NT})$, reducing the hBN thickness from 4 to 2 nm simply requires multiplying the BLG device result by $\operatorname{arccosh}(2\times 4\text{nm}/2\text{nm})/\operatorname{arccosh}(2\times 2\text{nm}/2\text{nm}) \approx 1.567$. Multiplying our adjusted C_{NT-BLG}/A by d_{NT} to convert it to capacitance per unit SWNT length, we find $C_{\text{eff}}/L = 6.11 \times 10^{-12}$ F/m for the geometric capacitance.

Finally, we must also account for the contribution from the quantum capacitance, which is particularly important for the SWNT. For a metallic SWNT, this has the simple form [118]

$$C_Q^{NT} = \frac{8e^2}{hv_F} \approx 310 \times 10^{-12}\text{F/m}. \tag{2.9}$$

This is substantially larger than geometrical capacitance estimated above but can easily be included in series with the geometric capacitance to give the total $C_{\text{bg-NT}}/L = 6.00 \times 10^{-12}$ F/m. The intrinsic quantum capacitance of graphene, which is relevant for the regime in which we observe an

appreciable drag signal, is given by [15]

$$C_{Qi}^{Gr} = \beta_g e^2 k_B T \ln(4), \tag{2.10}$$

where $\beta_g \sim 1.5 \times 10^6\ \mu\text{m}^{-2}\text{eV}^{-2}$ is a material constant. In the temperature range where we can access the linear response regime of Coulomb drag, $C_{Qi}^{Gr} \approx 4$ to 8×10^{-3} F/m, which is many orders of magnitude larger than the geometric capacitance and can safely be neglected.

Figure 2.9(b) summarizes the estimated upper and lower bounds of the Fermi energies of graphene E_F^{Gr} and SWNT E_F^{NT}. While the SWNT remains a heavily p-doped degenerate 1D conductor in the experimental gate voltage range, our analysis suggests that E_F^{Gr} is comparable to or even smaller than $k_B T$ in the temperature range $T > 100$ K, where k_B is the Boltzmann constant, for all V_g where the drag signal is measurable.

2.8 Comparison of SWNT-graphene Coulomb drag with theory

Having noted the similarity of our data to results in graphene-graphene systems, it is useful to more formally (if qualitatively) relate the charge carrier density dependence of R_{drag} in the SWNT-graphene system by comparison to perturbation theory for graphene-graphene drag [88,119]. Although this theory cannot account for the mixed-dimensional nature of our devices, its applicability in a broad range of carrier densities and temperatures make it a useful framework to understand some of the behavior in our system. Furthermore, the discrepancies between the 2D-2D theory and 1D-2D experiment may illuminate the ways in which dimensionality plays a role in the Coulomb drag behavior.

In comparing our experimental data with theoretical models, it is critical to know the charge carrier densities in the SWNT and graphene (n_{NT} and n_{Gr}), as well as their relationship with the chemical potential μ in each conductor. The net charge carrier density of single-gated graphene

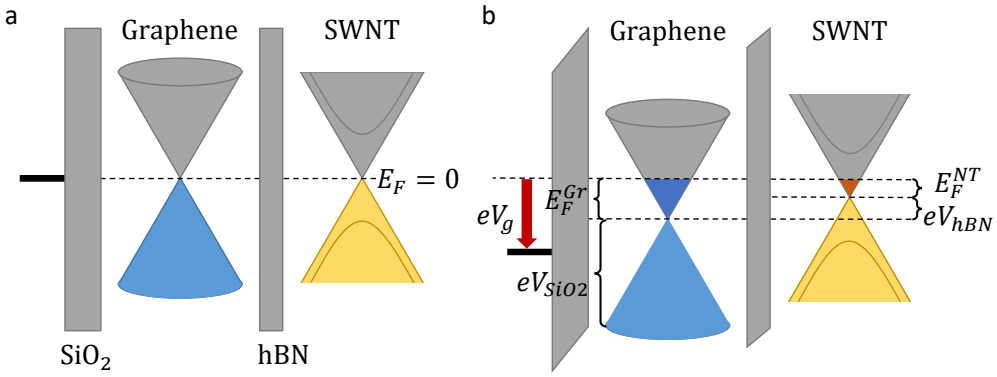

Figure 2.14: Band diagram of SWNT-graphene heterostructure (a) at $V_g = 0$ V (b) at positive gate voltage. Graphene band filling is represented in dark (light) blue and SWNT band filling is represented in orange (yellow) for conduction (valence) band. Adapted from Ref. 70.

heterostructures is generally well approximated by a parallel-plate capacitor formula:

$$n_{Gr} = \frac{C(V_g - V_0)}{e}, \tag{2.11}$$

where V_0 is the gate voltage of the graphene charge neutrality point (CNP) and C is the capacitance per unit area between the gate and graphene. However, this formula ignores the effect of the metallic SWNT on the local electrostatic environment of the graphene. Similarly, we cannot simply apply the analytic formula for the capacitance between a wire and a conducting plane [120] to estimate n_{NT} because the nearby graphene will substantially screen the electric field from the back gate, even though it is not situated between the gate and SWNT. In addition, our experiments are performed at relatively high temperature, so the approximation $\mu \approx E_F$ is not necessarily valid.

A more accurate approach to modeling the carrier densities and chemical potentials of the two layers (neglecting momentarily the local gating effect of the SWNT on the nearest region of the

graphene) starts with the coupling between the back gate and the conductors, given by:

$$eV_g = \mu_{Gr} + \frac{e^2(n_{Gr} + n_{NT}/2\pi r_{NT})}{C_1} \tag{2.12a}$$

$$\mu_{Gr} = \mu_{NT} + \frac{e^2 n_{NT}}{C_2} \tag{2.12b}$$

where C_1 is the capacitance per unit area between the graphene and back gate, C_2 is the capacitance per unit length between the SWNT and graphene, r_{NT} is the radius of the SWNT, and $\mu_{NT(Gr)}$ is the chemical potential of the nanotube (graphene). This is analogous to the single-gated graphene-graphene drag device considered in [70,88,119]. The SWNT takes the role of the "top" (more heavily screened) layer despite its position between the graphene and back gate because it is much closer to the graphene than to the back gate (2 nm versus 1 μm). In contrast, the screening effect of the SWNT on the graphene is significant but confined to < 10 nm on either side of the SWNT (see Fig. 2.11 and discussion of a finite element method based on COMSOL simulations in Section 2.7 for more details). Figure 2.14 schematically illustrates the effect of the back gate on the graphene and SWNT bands.

To verify that n_{Gr}, n_{NT} are linearly proportional to V_g, we can find the density n^*_{Gr} at which the electrical and chemical potentials become comparable (using a typical capacitance value $C_1 = 3.63 \times 10^{-5}$ F/m, obtained from our device geometry):

$$\hbar v_F \sqrt{\pi n^*_{Gr}} = \frac{e^2 n^*_{Gr}}{C_1} \rightarrow n^*_{Gr} \approx 7 \times 10^6 \text{ cm}^{-2}, \tag{2.13}$$

which is several orders of magnitude smaller than the residual impurity density, $\delta n \sim 1.1 \times 10^{10}$ cm^{-2}, and corresponds to $V_g = 0.3$ mV, smaller than the resolution of our gate voltage sweep; thus $V_g \propto n_{Gr}$ for all densities under consideration. Furthermore, the SWNT carrier density does not seem to substantially affect the drag behavior, apart from reducing the magnitude of R_{drag}

as n_{NT} increases (evident in lower magnitude of the h-h drag on the left side of the graphene CNP compared to the e-h drag on the right side of the graphene CNP, e.g. in Figure 2.4(f)). We observe essentially similar drag behavior regardless of the position of the SWNT conductance dip discussed in Section 2.4.1, as long as it does not overlap with the CNP of the graphene channel. Since experimentally, the SWNT is observed to be heavily p-doped, and remains degenerate, $V_g \propto n_{NT} \propto \mu_{NT}$, considering the constant density of states of the 1D SWNT band structure [15]. It should also be noted that, due to the chiral nature of graphene, the enhancement of electron-electron scattering at matched Fermi wavevectors (when $q = 2k_F$) that is typical in 2D electronic systems is not present in graphene-graphene drag systems [105]. Investigation of such enhancement in the SWNT-graphene system requires low-doping nanotubes and transport measurements near the nanotube CNP, an avenue for future study.

We can now consider 3 possible regimes of drag response, based on μ_{Gr} and T. When both are small ($\mu_{Gr}, k_B T < \tau^{-1}$, where $\tau(\mu_{Gr}, T)$ is the scattering time), the transport is disorder-dominated and n_{Gr} becomes temperature-independent [88]:

$$n_{Gr}(\mu_{Gr}, k_B T < \tau^{-1}) = \frac{\mu_{Gr}}{\hbar v_F^2 \tau}. \tag{2.14}$$

The relevant expression for Coulomb drag in this regime is either

$$\rho_{drag}(\mu_{Gr}, \mu_{NT} \ll T) \approx 1.41\alpha^2 \frac{\hbar}{e^2} \frac{\mu_{Gr}\mu_{NT}}{k_B^2 T^2}, \tag{2.15}$$

where $\alpha = e^2/v_F$ is the interaction strength, or at higher μ_{NT} (with $\mu_{NT} > \mu_{Gr}$ in our experiment),

$$\rho_{drag}(\mu_{Gr} \ll k_B T \ll \mu_{NT}) = 5.8\alpha^2 \frac{\hbar}{e^2} \frac{\mu_{Gr}}{\mu_{NT}}. \tag{2.16}$$

In either case, $\rho_{drag} \propto \mu_{Gr}$, and since we have established that $\mu_{Gr} \propto n_{Gr} \propto V_g$ in this regime,

the theory predicts $\rho_{drag} \propto V_g$. This prediction agrees with our R_{drag} data for gate voltages close to the graphene CNP (see for example Fig. 2.4(d),(f)). Due to the high SWNT hole density in the accessible gate voltage range in our devices, as discussed in Section 2.4.1, we expect that the regime of Equation 2.15 is not observed in our experiments.

At higher T, the graphene charge carriers close to the CNP ($T\tau > 1, \mu_{Gr} \ll T$) are in the Dirac fluid regime. In this case, the carrier density remains linear in μ but acquires temperature dependence:

$$n_{Gr}(\mu_{Gr} \ll k_B T) = \frac{1}{\hbar^2 \pi v_F^2} 4\ln(2) \mu_{Gr} k_B T. \tag{2.17}$$

A similar relationship between ρ_{drag} and V_g holds as in the disorder-dominated regime, although the temperature dependence is reduced by a factor of T (since now $\mu_{Gr} \propto n_{Gr}/T$). However, since we have relatively few data points in this regime, it is difficult to conclusively compare the theoretical and experimental temperature dependences.

Finally, $\mu_{Gr} \gg k_B T$ is the Fermi liquid regime, where n_{Gr} once again loses its temperature dependence:

$$n_{Gr}(\mu_{Gr} \gg k_B T) = \frac{1}{\hbar \pi v_F^2} \mu_{Gr}^2. \tag{2.18}$$

We must also consider the Fermi liquid expression for the Coulomb drag:

$$\rho_{drag}(\mu_{NT} > \mu_{Gr} \gg k_B T) \approx \alpha^2 \frac{\hbar}{e^2} \frac{8\pi^2}{3} \frac{k_B^2 T^2}{\mu_{Gr} \mu_{NT}} \ln\left(\frac{\mu_{Gr}}{k_B T}\right), \tag{2.19}$$

which implies $\rho_{drag} \propto T^2 / V_g^{1/2}$, neglecting any contribution from the SWNT. While this is qualitatively similar to the experimental behavior of R_{drag} at higher V_g (i.e. increasing with temperature and decaying as a power law with V_g), it does not align with a more quantitative analysis of the data (which finds $R_{drag} \propto V_g^{-1}$ to $V_g^{-1.3}$ at 140 K$< T <$ 300 K; see Fig. 2.9(c)). This disagreement suggests a more detailed theoretical analysis of the SWNT-graphene drag system is required to fully

understand the mechanisms at play.

2.9 Distance dependence of Coulomb drag response in graphene

Finally, we studied the relationship between the drag signal strength and the distance of the graphene voltage probes from the SWNT to see if we could find evidence of viscous electronic behavior. As mentioned in Section 2.2, previous experiments have demonstrated signatures of hydrodynamic electron flow from current injection into a rectangular graphene channel[20,89,91], with discernable effects even at room temperature[20,91]. Viscosity of the electron fluid causes the injected current to draw neighboring regions along with it, resulting in a negative potential near the injection contacts and creating current whirlpools in certain confined geometries[13,89,91,121]. Our SWNT-graphene Coulomb drag device geometry should provide a unique experimental probe of hydrodynamic flow of graphene charge carriers, as the current flowing in the SWNT generates a direct dragging force on the graphene carriers without injecting current in graphene. This approach should have the benefit of eliminating diffusive "spray" from the contacts that could mask hydrodynamic transport signatures.

Figure 2.15(a) shows R_{drag} measured at pairs of voltage probes in the graphene channel laterally displaced by distance x away from the SWNT. R_{drag} decreases as x increases, becoming almost unmeasurable for $x > 2$ μm. In Ohmic transport, such a diminishing drag signal can be understood with a diffusive model, where the escaping current density in the graphene just above the SWNT is expected to decay as $J_{esc}(x) \sim e^{-\pi x/W}$, where W is the channel width[122]. In the diffusive transport regime, we therefore expect driving current in the SWNT to cause a drag voltage in the probes at distance x away following $R_{drag}(x) \sim e^{-\pi x/W}$. The inset of Figure 2.15(a) shows that the measured $R_{drag}(x)$ follows such an exponential decay. We obtain the effective channel width W_{eff} by fitting this functional dependence. Figure 2.15(b) shows W_{eff} as a function of V_g. Interestingly, we find

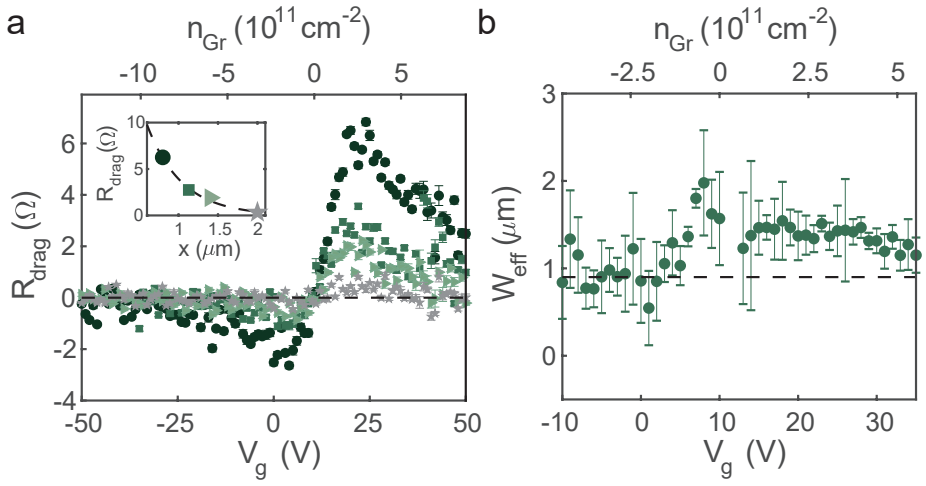

Figure 2.15: (a) R_{drag} versus V_g at $T = 300$ K for pairs of voltage probes at increasing distance x from the SWNT: 800 nm (circles), 1.2 μm (squares), 1.4 μm (triangles), and 2 μm (stars). Inset: R_{drag} at $V_g = 24$ V for increasing distances. Dashed curve is an exponential fit. (b) Effective channel width W_{eff} versus V_g, extracted from fit for R_{drag} at $T = 300$ K. Dashed line marks actual device width ($W = 1$ μm)

W_{eff} is larger than the physical channel width $W = 1$ μm in our device when the graphene is in the Dirac fluid regime, enhanced by about a factor of 2 at the CNP. Based on previous observations that the electron fluid of graphene is highly viscous in this temperature range near the CNP[89,123], the increase in W_{eff} may hint at a hydrodynamic contribution to the transport behavior. However, we cannot rule out the possibility that other effects, such as long-range currents due to edge disorder[124] may also play a role in the enhanced W_{eff}.

These results summarize our extensive experimental study of mixed-dimensional Coulomb drag between a SWNT and graphene. Our drag measurements in a SWNT-graphene heterostructure are qualitatively consistent with momentum transfer between the drive and drag layers, although we also observe an onset of nonlinearity due to local energy transfer combined with temperature dependent drag effects at lower temperatures. Within the linear response regime, the dependences on temperature, carrier density, and distance have subtleties that suggest an interplay of different mechanisms at work in this novel hybrid system. Further measurements with higher spatial resolution,

such as current imaging[20,94], would be necessary to gain a deeper understanding of the current flow patterns, and samples with less disorder should amplify hydrodynamic transport signatures in the graphene[13].

Love of learning is the most necessary passion ...in it lies our happiness. It's a sure remedy for what ails us, an unending source of pleasure.

Émilie du Châtelet

3

Electronic thermal transport in carbon nanotubes

Along with challenges, the carbon nanotube-graphene Coulomb drag experiment brought opportunities for new kinds of devices and measurements by instigating the development of the Rayleigh scattering spectroscopy, imaging and transfer tool (described in more detail in Appendix

C). The ability to see individual suspended carbon nanotubes, determine their chiral indices, and transfer them onto a target substrate with micron-level precision is rare, and we took advantage of it to perform novel measurements of the electronic thermal conductance of metallic and semiconducting carbon nanotubes using graphene-based Johnson noise thermometry.[37]

3.1 Johnson noise thermometry in graphene

A conductor with finite electrical resistance R hosting electrons with temperature T_e will experience voltage fluctuations* known as Johnson-Nyquist noise (or simply Johnson noise), that are classically given by the Nyquist theorem[40,125,126]:

$$\langle V^2 \rangle = 4k_B T_e R \Delta f, \tag{3.1}$$

where $\langle V^2 \rangle$ is the time-averaged mean-squared voltage and Δf is the measurement frequency bandwidth. Measurements of Johnson noise can therefore be used to determine the electron temperature of a system.

In two-terminal graphene devices, this method has been used to measure the electronic thermal conductance[18,40,41,127,128] by sending a current through the device, causing a temperature rise due to Joule heating (schematically illustrated in Fig. 3.1). This method works well for "self-heating" measurements of graphene because of low energy loss to phonons, the ability to make mesoscopic devices with low contact resistance, and its tunability via electrostatic gating into a diffusive conducting regime, where electronic diffusion cooling is the dominant channel for energy loss in a wide range of bath temperatures[37]. Many materials for which electronic thermal transport measurements could provide valuable information do not meet some or all of these criteria. In graphene self-heating measurements, the graphene channel serves as both the heater and as the thermometer,

*or current fluctuations, if it is held at zero voltage

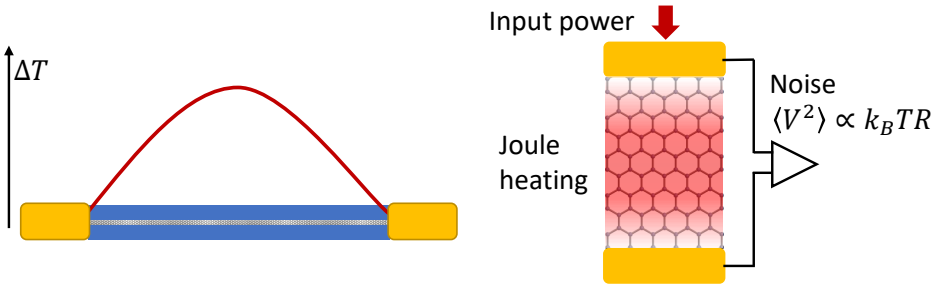

Figure 3.1: Schematic of graphene self-heating measurement with Johnson noise. Power applied in the form of current through the two-terminal graphene device causes Joule heating in the graphene channel, producing a parabolic temperature distribution in the absence of contact resistance and with the contacts fixed at the bath temperature. Measured voltage noise is proportional to the average temperature of the electrons in the device.

but for other materials, it is more ideal to be able to create a thermal gradient across a device and measure the temperature in at least two locations to determine the energy flow. Implementing this concept with Johnson noise thermometry requires local measurements of the voltage fluctuations across two resistors that are thermally coupled to two points along a mesoscopic sample (or to two edges of a finite-width sample).

3.2 Multi-terminal noise measurements of thermal conductivity

One can extend two-terminal Johnson noise thermometry into a multi-terminal noise measurement. Multi-terminal noise has been theoretically studied in a diffusive conductor with arbitrary geometry [129] (see Fig. 3.2 for an example system). The conductor has multiple leads held at a fixed bath temperature (T_{bath}), and current is injected though one of the leads. Joule heating causes a temperature increase in the main body of the conductor. The noise power between any two terminals n and m is

$$S_{nm} = \int_{-\infty}^{+\infty} dt \langle \delta I_n(t) \delta I_m(0) \rangle, \tag{3.2}$$

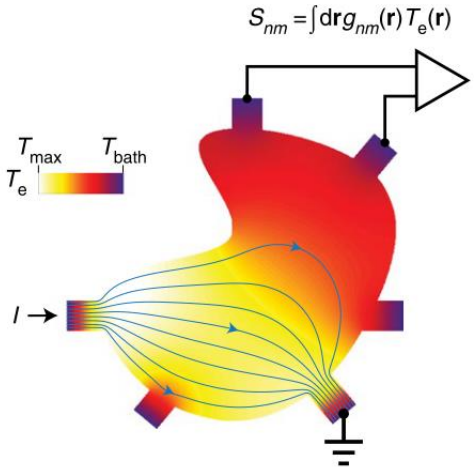

Figure 3.2: Schematic of multi-terminal noise measurement. A diffusive conductor is connected to terminals held at fixed T_{bath}. Finite-element simulation of the temperature and current distribution, assuming uniform conductivity, is shown in the color scale and streamlines, respectively. Without energy loss to phonons, the noise S_{nm} measured at any two terminals is given by a weighted function of the electronic temperature distribution T_e (see Section 3.2).

where δI_n and δI_m are the fluctuation currents at terminals n and m. If the electrons are strongly thermally equilibrated, so that a local electron temperature $T_e(\vec{r})$ can be defined (the "hot electron" regime), this relation can be written

$$S_{nm} = \int d\vec{r}(\nabla\varphi_n \cdot \hat{\sigma}\nabla\varphi_m) T_e(\vec{r}) = \int d\vec{r} g_{nm}(\vec{r}) T_e(\vec{r}), \tag{3.3}$$

with the locally-defined weighting function $g_{nm} = \nabla\varphi_n \cdot \hat{\sigma}\nabla\varphi_m$ defined via the local conductivity $\hat{\sigma}$ and the characteristic potentials φ_n and φ_m for each terminal of the device [37,129]. If energy losses to phonons and other potential heat sinks are negligible, the noise at any terminal is therefore closely linked to the energy flow to that region of the device and the associated electronic temperature distribution.

For measurements of the electronic thermal conductance of carbon nanotubes and other materials, we fabricated devices with the geometry shown in Figure 3.3(a). There are two pairs of terminals

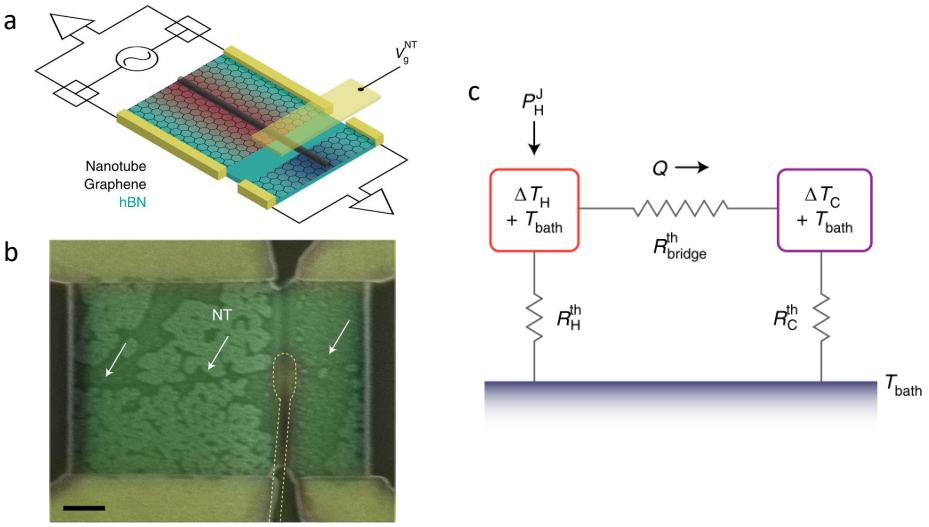

Figure 3.3: (a) Schematic of device with two graphene thermometers and carbon nanotube bridge. Monolayer graphene with an etched slit separating the two pieces rests on a bottom hBN layer. A carbon nanotube connects the hot and cold side graphene pieces, and a local metallic top gate tunes the nanotube carrier density. (b) Composite optical and scanning electron microscopy image of an example device. Scale bar is $1\ \mu$m. The dashed yellow line shows the location of the metal top gate. White arrows indicate the location of the nanotube, visible as a dark line in the composite image. (c) Thermal circuit for a thermal conductance measurement. Joule power P_H^J is injected into hot side reservoir connected by thermal resistance R_H^{th} to T_{bath}. The bridge thermal resistance R_{bridge}^{th} allows thermal current Q to cross from the hot to the cold side, connected to the bath by R_C^{th}.

on either side of a central conductor. Each pair contacts a rectangular piece of graphene, forming two diffusive electronic thermometers. The central conductor, which need not be diffusive, bridges the gap between the two rectangular thermometers at their midpoints. This configuration enables us to realize the thermal circuit shown in Figure 3.3(b). A low-frequency current is injected into the wider rectangle on the left, Joule heating the diffusive electrons. The local temperature is measured both for this "hot side" (which is defined as $T_H = \Delta T_H + T_{bath}$) and on the other rectangle on the "cold side" of the device ($T_C = \Delta T_C + T_{bath}$), where ΔT_H and ΔT_C are the temperature increases on the hot and cold sides of the device, respectively, above the bath temperature T_{bath}. Energy current Q crosses the bridge, heating the cold side at its center point. The energy current is equilibrated at the cold side contacts, generating a peaked temperature distribution and non-local voltage fluctuations. Combining measurements of these temperatures with the energy current Q across the bridge gives the two-terminal thermal conductance of the bridge, $G^{th}_{bridge} = \frac{Q}{T_H - T_C}$. The width of the bridge is designed to be small compared with the length of the hot side so that it obtains a thermal bias at the peak of the hot side temperature distribution. The wide hot side ensures a local temperature distribution that is insensitive to the bridge, while the narrow cold side maintains a maximal average T_C for a given Q.

While the measurement of the hot and cold side temperatures is the same as for a two-terminal graphene device, the extraction of the energy current across the bridge requires more analysis. All of the heating on the cold side of the device is a result of this energy current, so measuring its temperature increase relative to the bath temperature will give us a measurement of the heating power coming from the bridge, almost as if the same input power were the result of injected current in a self-heating measurement[37].

Consider energy current Q injected at the midpoint of a rectangular cold side of length L and width W with contacts thermalized to the bath, as shown in Fig. 3.4. We refer back to Fourier's law to relate the energy current density to the temperature increase via the thermal conductivity,

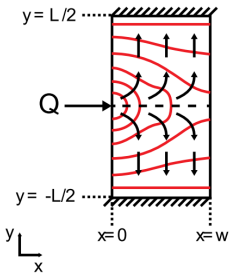

Figure 3.4: Geometry for derivation of relationship between energy current across the bridge and cold side noise measurement. Energy current Q (from the bridge) is injected at the midpoint of a rectangular two-terminal device.

$q = -\kappa \nabla T$ (note slightly different naming conventions from Section 2.5; q is the energy current density). We can obtain the total energy current by integrating over the width of the cold side:

$$\frac{Q}{2} = \int_0^W dx\, \vec{q}(x,y) \cdot \hat{y}, \tag{3.4}$$

where the factor of $1/2$ comes from the assumption that half the energy current flows to each contact. Assuming negligible energy loss to phonons, we can insert Fourier's law:

$$\frac{Q}{2} = -\kappa \int_0^W dx\, \frac{dT}{dy}. \tag{3.5}$$

If we let $T_{bath} = T(x, y = \pm L/2) = 0$ for simplicity, we can write the temperature distribution in the sample to its derivative as $T(x,y) = -\int_0^y dy'\, dT/dy'$. Then, we can integrate both sides of Eq. 3.5 over y:

$$\int_0^y dy'\, \frac{Q}{2} = -\kappa \int_0^y dy' \int_0^W dx\, \frac{dT}{dy'}, \tag{3.6}$$

which becomes

$$\frac{Q}{2} y = \kappa \int_0^W dx\, T(x,y). \tag{3.7}$$

Integrating again over y, we have

$$\int_0^{L/2} dy\, \frac{Q}{2} y = \kappa \int_0^{L/2} dy \int_0^{W} dx\, T(x,y). \tag{3.8}$$

The integrals on the right-hand side give the average of the cold side temperature distribution, ΔT_C, which can be found experimentally from a Johnson noise measurement of the cold side. Since the total energy current Q has no y-dependence, we can perform the integral on the left-hand side and rearrange terms to find

$$Q = \frac{8W}{L} \kappa \Delta T_C. \tag{3.9}$$

Finally, we can express Q in terms of the cold side thermal conductance $G_C^{th} = P_J^C / \Delta T_C^{s.b.}$, which is obtained from an independent self-heating measurement with applied Joule power P_J^C and resulting temperature increase $\Delta T_C^{s.b.}$. Combining this with Eq. 3.8 and the self-heating result $\kappa = \frac{L}{12W} G_C^{th}$ [40,41], we find

$$Q = \frac{2}{3} G_C^{th} \Delta T_C. \tag{3.10}$$

A more general derivation (for arbitrary cold side geometry) can be found in Ref. 37, along with an alternative derivation of Eq. 3.10 using the effective thermal circuit model shown in Fig. 3.3(c).

It is crucial that each thermometer measures the local temperatures T_H and T_C without cross-contaminating the signals, even though the two sides may be in electrical contact if the bridge is conducting. An important innovation for this measurement method was the development of differential noise thermometry [130]. With this technique, noise from a differential bias applied to a sample is amplified, bandpass-filtered, and integrated over a frequency range that can be adjusted by choosing different components in an LC impedance matching circuit and appropriate filters, resulting in a voltage signal proportional to the total noise power in the specified frequency band (between 100 MHz and 1 GHz). A simplified schematic of a noise measurement circuit for these devices is

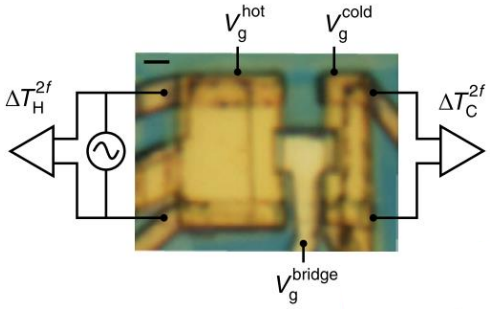

Figure 3.5: Differential noise thermometry circuit schematic overlaid on example device with graphene thermometers and graphene bridge, all with separate metal top gates.

shown in Figure 3.5. For these multi-terminal noise measurements, non-overlapping bands used for the hot and cold sides enable independent measurements of T_H and T_C. The amplified and filtered signals are sent through a power detector that generates a voltage proportional to the integrated high-frequency noise spectral density. By applying a low-frequency heating current at frequency f, the temperature of the system is modulated at frequency $2f$, and the output voltage is amplitude-modulated at frequency $2f$. The change in noise power amplitude due to the applied Joule power can be isolated using lock-in amplifiers. After calibration (achieved by separate self-heating measurements of the resistance and noise power of the hot and cold side thermometers at fixed temperatures)[130], the $2f$ noise power voltage signal is converted into a temperature rise above the bath temperature, $\Delta T_{H,C}$. This method has been previously shown to enable sub-millikelvin precision with a 30 second averaging time[37,130].

Another critical detail for these measurements is ensuring the heating circuit is balanced such that only energy current Q and not charge current can cross the bridge from hot to cold side. A schematic of the tuning circuit is shown in Figure 3.6. A low-frequency differential voltage excitation is applied to the hot side with a lock-in amplifier, passing through a biasing resistor connected to each terminal. At least one of these resistors must be tunable. The cold side terminals are con-

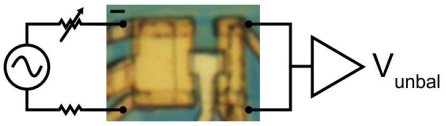

Figure 3.6: Balancing circuit schematic for example graphene device.

nected and their common mode voltage V_{unbal} is measured at the frequency of the hot side excitation. The tunable biasing resistor is adjusted to make $V_{unbal} = 0$; then we know that when a differential bias is applied to the hot side, no electrical current reaches the cold side. This circuit balancing can also be adjusted to accommodate arbitrary thermal and electrical biasing conditions[37].

From a materials perspective, graphene is an excellent choice of material for the hot and cold side heater/thermometer sections of the device due to its strong interactions leading to fast temperature equilibration, low energy loss to phonons, small electronic thermal conductance, and tunability into a diffusive conducting regime[18,37,40,41,127,130]. As mentioned above, these enable Joule heating and accurate Johnson noise thermometry for the two-terminal hot and cold side segments of the device, regardless of the behavior of the bridge. As such, the bridge material can be made not only of graphene, but many other materials of interest. Using a carbon nanotube as a bridge was an opportunity to test this measurement scheme in the ultimate 1D limit. We were also motivated by the possibility of measuring thermal transport signatures of Luttinger liquid behavior[131,132], the strongly-correlated state that can arise in 1D materials due to their extreme geometric confinement, which has been observed in other measurements of carbon nanotubes[4]. Since the Coulomb drag measurements discussed in Chapter 2 were made more difficult by large nanotube resistances ($\gtrsim 1$ MΩ) compared to the graphene resistance, I will note a few differences in the device geometry that improve the potential for high-quality electrical and thermal transport in the nanotube. The high nanotube resistances in the drag devices were due to a combination of their length (typically tens of microns), disorder on the SiO_2 substrate, and suboptimal contact resistances[17,133]. For the multi-

terminal noise measurement devices, we choose to measure nanotube bridges that are much shorter, resting on hBN instead of SiO_2, and with the electrical contacts formed by sections of graphene (the hot and cold sides), so the resistance can potentially be much lower (although, as we will see, the effects of disorder are not entirely mitigated).

3.3 Thermal transport device fabrication

The carbon nanotube (NT) growth and characterization process were the same as described in Section 2.3. For these devices, we primarily targeted metallic NTs, but some semiconducting NTs were also measured.

To form the graphene thermometer/heater sections, heterostructures of monolayer graphene on top of a 20–60 nm hBN flake were prepared using the inverted stacking technique. This entails picking up first the hBN flake, then the graphene flake using a PPC film on a PDMS stamp, then peeling away the PPC film from the PDMS and depositing it on a SiO_2/p-doped Si chip, with the PPC film underneath the flakes. The PPC is then removed by high-temperature annealing in vacuum. The result is a clean graphene flake resting on hBN. A 200–500-nm wide, $>$ 10-μm long slit was then created in the graphene by defining a PMMA mask using e-beam lithography and etching with O_2 plasma in a reactive ion etcher (see Fig 3.7(a)). A second e-beam lithography step defined a resist-free window above the heterostructure, while the rest of the chip remained coated in $\sim$ 100 nm of resist, and carbon nanotube were transferred using the same method described in Section 2.3 (see Fig 3.7(b)). Since we could prepare starting graphene/hBN heterostructures much larger than the individual devices, often several NTs were transferred to different sections of the stack, using the same resist window. Subsequent fabrication steps defined the individual devices.

Following NT transfer, electrical contacts were made at the edges of the graphene following the method reported previously[9]. The unwanted sections of the heterostructure were removed by re-

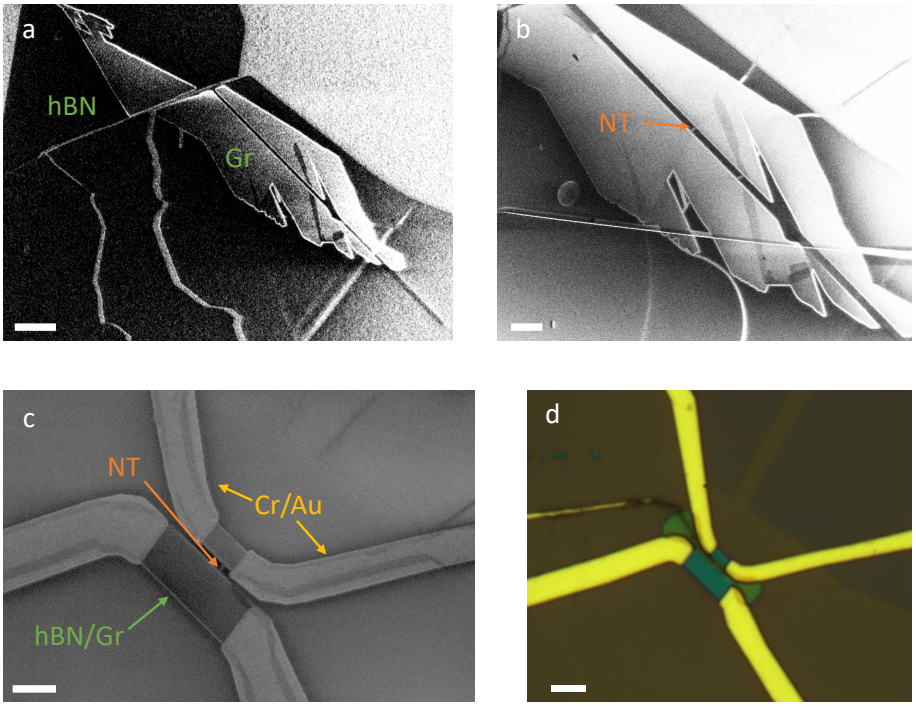

Figure 3.7: (a) SEM image of inverted graphene/hBN heterostructure, after slit etch. Scale bar is 5 μm. (b) SEM image after nanotube transfer and PMMA removal. The nanotube used for the device is indicated by the orange arrow as it crosses the slit. Another nanotube was transferred but not used and is also visible. Scale bar is 4 μm. (c) Device after fabrication of graphene contacts and etching of the hot and cold sides, before HSQ and top gate deposition. Scale bar is 2 μm. (d) Final device with top gate. Scale bar is 4 μm.

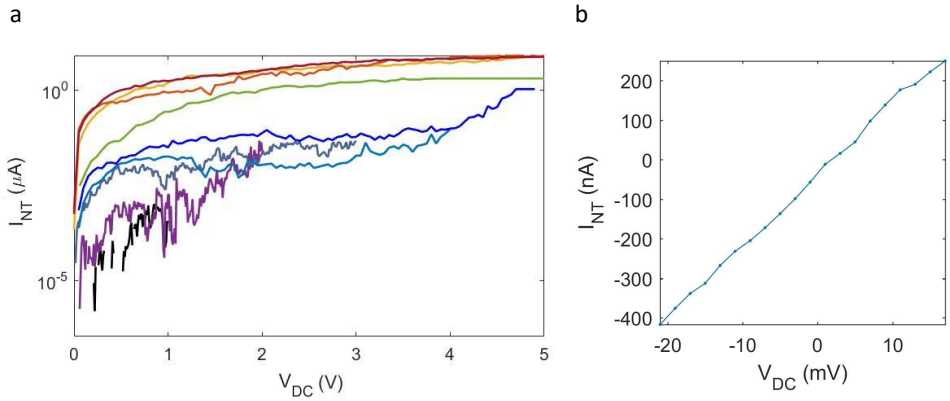

Figure 3.8: (a) Current annealing of a semiconducting NT device. DC voltage bias. Black curve shows the initial measurement of current at both cold side terminals (shorted together) as a function of DC voltage bias V_{DC} on the hot side, with subsequent annealing measurements in purple, slate blue, medium blue, royal blue, green, yellow, orange, and finally red, showing improvement in the bridge resistance from $R_{NT} \approx 850$ MΩ to $R_{NT} \approx 600$ kΩ. Measurements were performed in vacuum at room temperature. (b) Current-voltage relationship for a device with a well-coupled metallic NT; $R_{NT} \approx 10$ kΩ.

active ion etching with CHF_3 (Fig 3.7(c)). An insulating layer of 120 nm SiO_2 was made above the NT by e-beam lithography of hydrogen silsesquioxane (HSQ) resist and development with CD-26 developer. A final e-beam lithography step defined the mask for the local top gate above the NT, which was formed by thermal evaporation of 3 nm Cr/7 nm Pd/70 nm Au (using an angled, rotating stage to mitigate height differences between different parts of the structure). Figure 3.7(d) shows a final device.

3.4 Johnson noise measurements of carbon nanotube devices

During initial measurements NT-graphene thermometry devices, we frequently observed a high bridge resistance, sometimes up to hundreds of MΩ. This is attributable to disorder along the NT and at the graphene-NT interface due to fabrication residue. We could substantially reduce the bridge resistance by current annealing the NT, as shown in Figure 3.8(a). DC current was measured

on the cold side while a DC voltage bias V_{DC} applied to both contacts on the hot side was slowly increased, until an upturn in the current was observed. This process was repeated until the current-voltage relationship no longer changed between bias sweeps. Current annealing often reduced the bridge resistance by several orders of magnitude. In some cases, we were able to achieve excellent coupling between the NT and the graphene thermometers; Figure 3.8(b) shows a measured bridge resistance of 10 kΩ, which is near the quantized value of $h/4e^2 = 6.45$ kΩ allowed for the fourfold-degenerate (spin and K/K') 1D subband of a carbon nanotube [17].

3.4.1 NT-graphene device calibration

Even after current annealing, NT bridge devices remained more disordered than similar devices with a graphene bridge that were fabricated from a single graphene flake and fully encapsulated in hBN. As a result, there was additional energy loss from the electronic system to the bath in the NT bridge devices. We can see this by comparing measurements of the cold side temperature rise ΔT_C at constant applied power on the hot side P_J^H while varying the gate voltage controlling the cold side, schematically shown in Figure 3.9(a). This changes the cold side resistance, and should have a corresponding effect on ΔT_C. Fig. 3.9(b) shows the results of this measurement for a fully-encapsulated graphene device: the Dirac peak in the cold side resistance is visible in the top panel, and ΔT_C in the bottom panel is indeed correlated with the resistance. For this thermal circuit (see Fig. 3.3(c)), we expect $\Delta T_C = Q_{in} G^{th}_{bridge} / \sum_{ij} G^{th}_i G^{th}_j$, so the decrease of ΔT_C with increasing G^{th}_C is expected.

Fig. 3.9(d) shows the same measurement on a NT bridge device. The cold side Dirac peak in the resistance (top panel) has the same qualitative behavior as the monolithic graphene device, but the ΔT_C behavior is quite different. ΔT_C is lowest when the cold side resistance is highest, and increases as the resistance decreases. We therefore postulate there is an additional mechanism of energy loss to the phonon bath working to reduce ΔT_C near charge neutrality, counteracting the effect of the

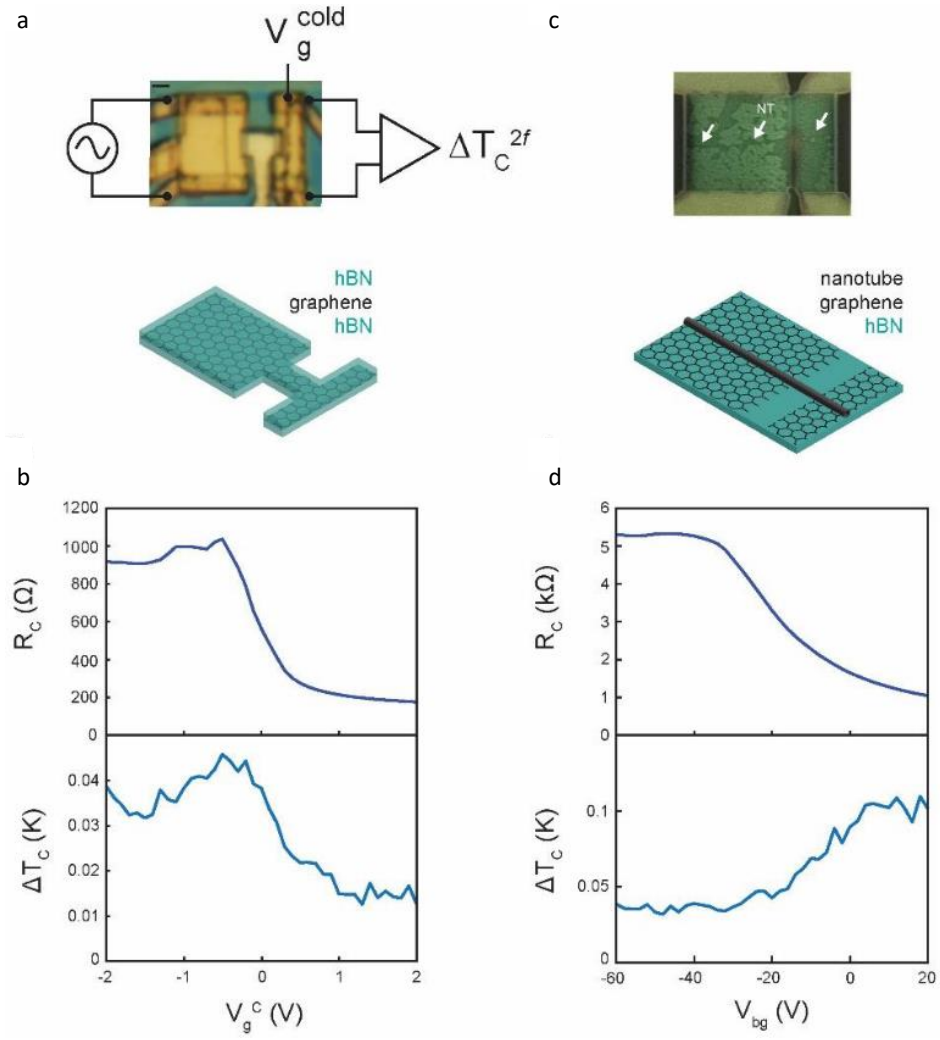

Figure 3.9: (a) Top: circuit schematic for energy loss measurements. Joule power is applied to the hot side and temperature change is measured on the cold side as a function of cold side gate voltage (for the displayed device, this is local top gate voltage V_g^{cold}). Bottom: stack for fully-encapsulated graphene device. (b) Cold side graphene resistance R_C and cold side temperature change due to hot side heating ΔT_C as a function of local cold side top gate voltage V_g^C. (c) Top: composite optical and scanning electron microscope image of device with NT bridge (see Figs. 3.3 and 3.7 for details). Bottom: device stack. (d) Cold side graphene resistance R_C and cold side temperature change due to hot side heating ΔT_C for NT bridge device as a function of global back gate voltage V_{bg}.

decreased G_C^{th}. Like the often-high initial NT resistance values, we believe that disorder due to fabrication residue on the un-encapsulated graphene plays a significant role in the excess energy loss to the phonon bath, since previous work has shown larger energy loss in disordered, un-encapsulated graphene compared to fully-encapsulated, cleaner devices [18,40,41,127,130]. When measuring NT bridge devices, we kept the cold side near charge neutrality to minimize its thermal conductance, therefore maximizing its sensitivity as a power meter for small amounts of heat flowing through the nanotubes. Since this is precisely where the excess heat loss is most pronounced, we must interpret our measured electronic thermal conductance values as lower bounds. While such a parasitic heat path makes estimation of the absolute value of the thermal conductance challenging in our devices, relative measurement is possible by tuning the local top gate voltage V_g^{NT}, keeping the hot and cold sides at fixed carrier density.

3.4.2 Doping- and thermal bias-dependent thermal transport

We simultaneously measured the electrical and thermal conductances, G_{NT} and G_{NT}^{th}, of NT bridges as a function of local top gate voltage V_g^{NT}, shown in Figure 3.10. We found the two conductances to be generally well correlated. In a device with relatively low channel resistance (Device 1, Fig. 3.10(a)), the electrical conductance shows a global minimum at $V_g^{NT} = 15$ V at $T_{bath} = 70$ K, corresponding to a small electronic bandgap; the thermal conductance shows similar behavior. With decreasing bath temperature, rapid modulations were observed in both the electrical and thermal conductance, becoming more pronounced at lower temperature. This oscillatory conductance indicates the onset of Coulomb blockade through the disordered NT [27]. For temperatures above the Coulomb blockade regime, the conductance was nearly temperature independent, demonstrating the previously-observed weak electron-phonon coupling in carbon nanotubes (discussed further in Section 3.4.3).

In a device with a larger bandgap and higher channel resistance (Device 2, Fig. 3.10(b)), the NT

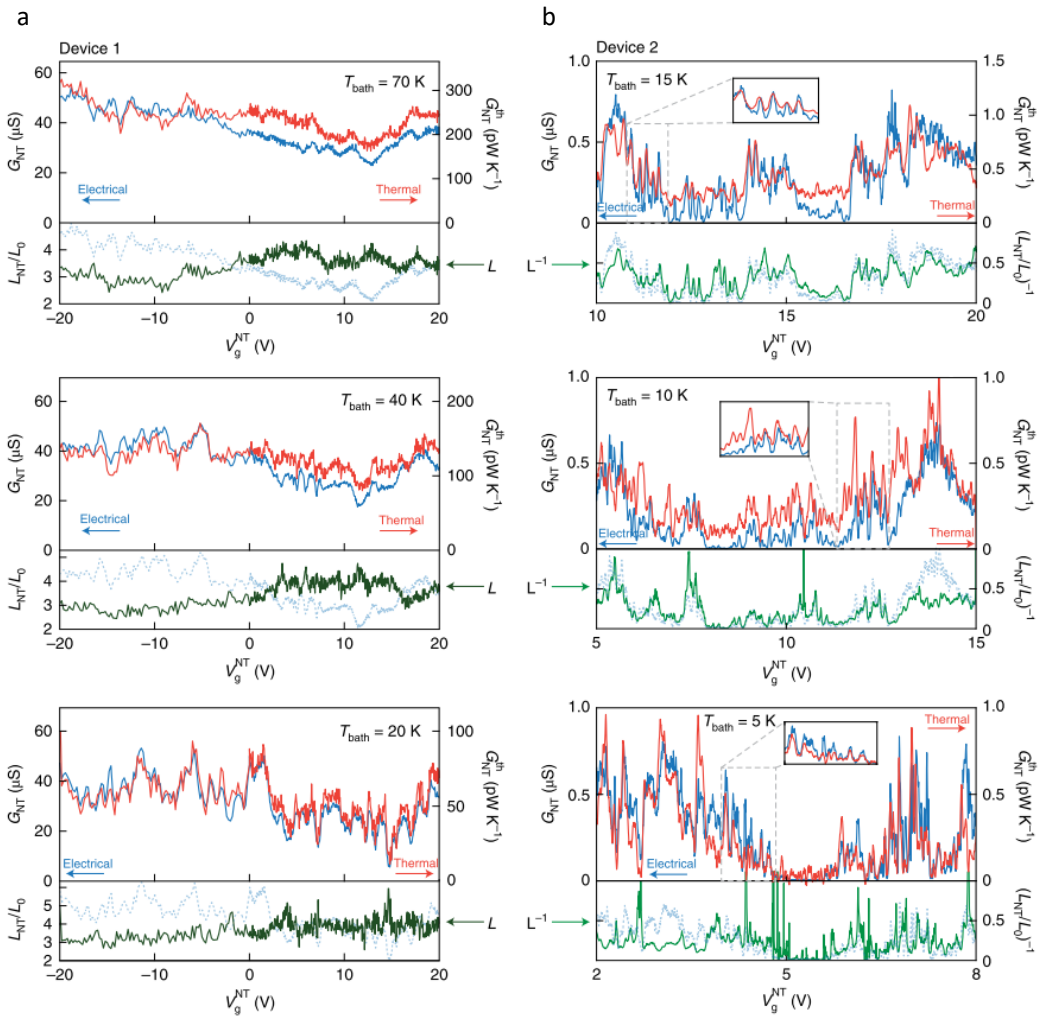

Figure 3.10: (a) Two-point electrical and thermal conductance measurements of Device 1, which has a small-bandgap (metallic) NT, as a function of local top gate voltage V_g^{NT} at different bath temperatures. Lower panels in each plot show the corresponding Lorenz ratio L_{NT}/L_0 (green), together with the electrical conductance from the upper panel (dotted light blue) to facilitate explicit comparison with L_{NT}/L_0. All thermal quantities are lower bounds, and the thermal bias for all plots in $\Delta T_H/T_{bath} = 0.1$. (b) Two-point electrical and thermal conductance measurements of Device 2, which has a high-resistance NT, at different bath temperatures. The corresponding inverse Lorenz ratio $(L_{NT}/L_0)^1$ is shown (green) in the lower panels, together with the electrical conductance reproduced from the respective upper panel (dotted light blue). Top and middle panels have $\Delta T_H/T_{bath} = 1$; bottom panel has $\Delta T_H/T_{bath} = 0.5$. A DC voltage of 30 mV was applied across the NT to overcome the contact barrier; the corresponding measured DC current on the nanoampere scale led to negligible background heating and did not affect the measurements at the $2f$ heating frequency. The insets show magnifications of Coulomb blockade peaks.

is in a disordered Coulomb blockade regime. We observed sharp peaks alternating with vanishing electrical conductance at lower temperatures (Fig. 3.10(b) bottom, inset). The thermal conductance remains highly correlated with the electrical signal, despite the much higher channel resistance ($R_{NT} > 1\,\mathrm{M}\Omega$, equivalent to to $G_{NT} \approx 10^{-3}\ e^2/h$). We were able to measure the corresponding thermal conductance down to $\sim 1\%$ of the thermal conductance quantum at $T_{bath} = 5$ K. The ability of detect electronic thermal transport in a system with far less than a single open quantum channel demonstrates the high sensitivity of the graphene noise thermometers.

We can quantify the relationship between G_{NT} and G_{NT}^{th} by comparing it to the WF law (Eq. 1.12), computing the Lorenz ratio

$$L_{NT}/L_0 = G_{NT}^{th}/L_0 T G_{NT}. \tag{3.11}$$

For the higher-conductance device (Device 1), L_{NT}/L_0 was significantly higher than 1 for all measured gate and temperature ranges (lower panels in Fig. 3.10(a)), indicating a violation of the WF law. This is consistent with previous measurements of quasi-1D systems[33] and with several theoretical predictions for 1D thermal transport[131,132,134]. We note that the Lorenz ratio peaks when there is a dip in G_{NT}, indicating enhanced thermal conduction when electrical conductance is suppressed. In the more resistive device (Device 2), this increased thermal conduction is easier to see in the inverse Lorenz ratio $(L_{NT}/L_0)^{-1}$ (lower panels in Fig. 3.10(b)), which is strongly correlated with G_{NT}. The gate dependence of both signatures excludes contact resistance as the source of the WF violation.

3.4.3 Electron-phonon coupling in NT bridge devices

Before discussing further measurements, I will show evidence that electron-phonon coupling is negligible in our NT bridge devices. We should first note that electron-phonon coupling in graphene

is weak in the temperature range we are considering ($T_{bath} < 70$ K)[48], which means the thermal bias is predominantly electronic and the energy injected into the device by Joule heating remains in the electronic subsystem. As for NTs, it has previously been shown that they exhibit ballistic electronic transport up to room temperature, with neglible electron-phonon coupling and temperature-independent electrical conductance[135,136,137,138]. Our data at temperatures higher than the Coulomb blockade regime (Fig. 3.10(a)) are consistent with these findings.

Electron-phonon coupling in the NT would cause some of the electrons' energy due to Joule heating to transfer to phonons in the bridge. Since the cold side thermometer is, like the hot side, simply made out of hBN-supported graphene, it measures only the electronic part of the energy transported across the bridge. In the event of energy loss to phonons in the NT, less energy current would reach the cold side thermometer, resulting in a lower apparent G^{th}_{NT} and correspondingly a suppressed Lorenz ratio L_{NT}/L_0. We instead observe an *enhanced* Lorenz ratio, consistent with minimal energy loss to phonons in the NT. Some energy transfer could still be possible by coupling NT phonons to graphene electrons, but this is a higher-order process requiring either remote coupling of an NT phonon to a graphene electron or two weak coupling events (NT phonon to graphene phonon and graphene phonon to graphene electron), and therefore highly unlikely.

This discussion has been premised on the idea that the hot and cold side thermometers do not have appreciable electron-phonon coupling. It is possible for this to change, for example at higher bath temperature, particularly near charge neutrality[49]. If that is the case, the hot side could excite both electrons and phonons in the bridge, and the cold side would measure energy transport due to both electrons and phonons. To confirm that these additional energy transfer mechanisms do not come into play, we perform measurements of Device 2 with the NT tuned into the single-particle gap, shown in Figure 3.11. In this case, no charge should be present in the NT and no electron transport is allowed, so we can shut off electrical conduction over a wide temperature range. We apply a large thermal bias, $\Delta T_H/T_{bath} = 0.4$, and simultaneously measure the nanotube's DC re-

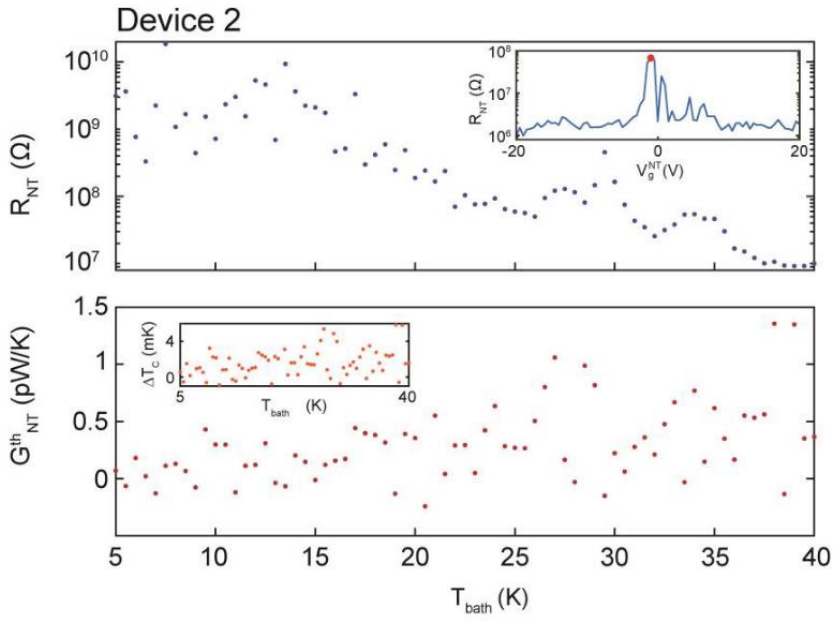

Figure 3.11: Nanotube electrical and thermal conductance in the bandgap. Top panel: nanotube resistance R_{NT} as a function of bath temperature T_{bath}. Inset shows R_{NT} as a function of local top gate voltage V_g^{NT}, with red dot indicating the gate voltage used in other panels. Bottom panel: G_{NT}^{th} as a function of T_{bath}, with thermal bias $\Delta T_H/T_{bath} = 0.4$. Inset: measured cold side temperature rise ΔT_C vs. T_{bath}.

sistance R_{NT}, cold side temperature rise ΔT_C, and NT thermal conductance G^{th}_{NT} as a function of T_{bath}. R_{NT} (top panel) remains high over the entire temperature range, but decreases from $\sim$ 10 GΩ to $\sim$ 100 MΩ with increasing temperature. In contrast, both G^{th}_{NT} and ΔT_C (bottom panel and inset) remain almost indistinguishable from zero, with appreciable scatter in the data that only slighly increases with temperature. The measured value of ΔT_C of $\sim$ 1 mK remains close to the noise floor of the measurement. We conclude that non-electronic heat transport does not play a significant role in the temperature range we have studied.

3.4.4 Temperature dependence of the Lorenz ratio

We continue our analysis of the NT bridge devices by considering the temperature dependence of the electrical and electronic thermal conductances at constant NT doping and thermal bias, shown in Figures 3.12 and 3.13 for four different values of V_g^{NT}. We consistently find that the electrical conductane G_{NT} remains nearly constant upon sweeping the bath temperature between 5 K and $\sim$ 70 K (top panels). During the same measurement, G^{th}_{NT} is almost linearly increasing (middle panels). The resulting Lorenz ratios $L_{NT}/L_0 = G^{th}_{NT}/L_0 T G_{NT}$ (bottom panels) show a uniform trend for all V_g^{NT} studied, decreasing from $\sim$ 6 at $T_{bath} = 5$ K until $\sim$ 20 K, then remaining approximately constant at $\sim$ 3. This sometimes appears to arise from decreased G_{NT} at low T_{bath} (Figs. 3.12(b) and 3.13(b)) and sometimes from slightly sublinear behavior of G^{th}_{NT} (Figs. 3.12(a) and 3.13(a)) in the same temperature range.

We can consider how our observations fit into theoretical predictions for electronic thermal transport in 1D systems. Several models of Luttinger liquid thermal transport [132,139,140] have L/L_0 decreasing with increasing T_{bath} in a qualitatively similar way, in some cases saturating at the lowest temperatures [139] in addition to flattening out at higher temperatures. However, we do not find quantitative agreement between our data and the theoretical models for thermal transport in a disordered Luttinger liquid (due at least in part due to the thermometry issue discussed in Section 3.4.1).

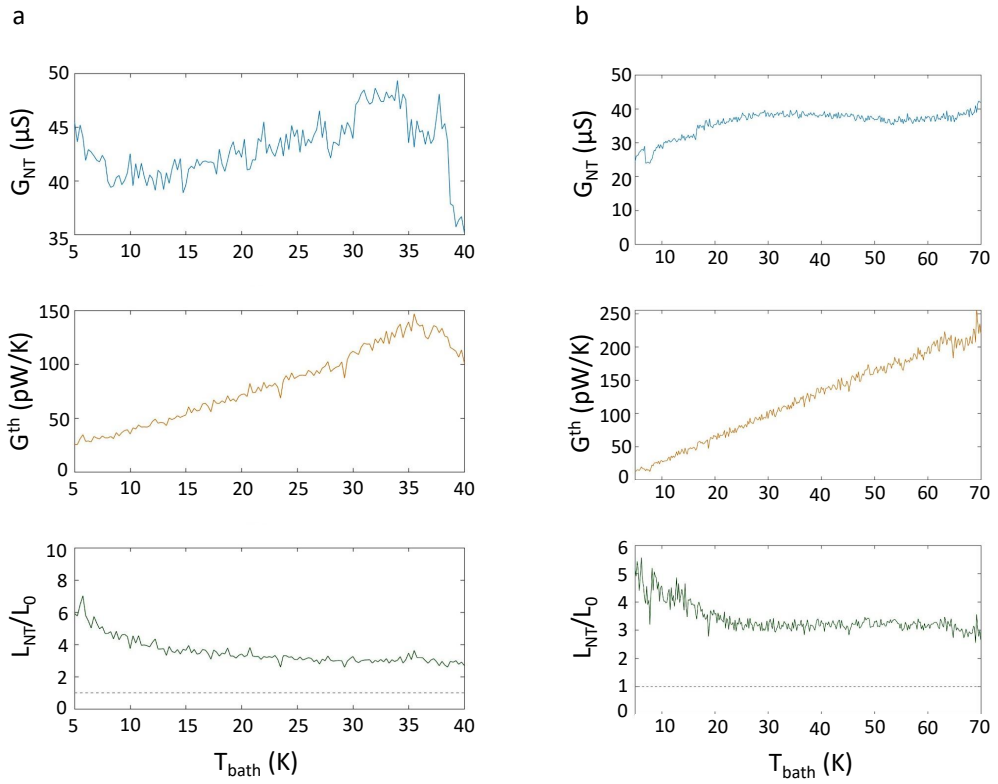

Figure 3.12: Temperature dependence of Device 1 at constant NT doping and thermal bias $\Delta T_H/T_{bath} = 0.1$. (a) G_{NT} (top panel), G^{th}_{NT} (middle), and L_{NT}/L_0 (bottom) as a function of T_{bath} at $V_g^{NT} = -5$ V. (b) Same measurement as (a), with $V_g^{NT} = 0$ V. NT channel resistance $R_{NT} = 1/G_{NT}$ is shown.

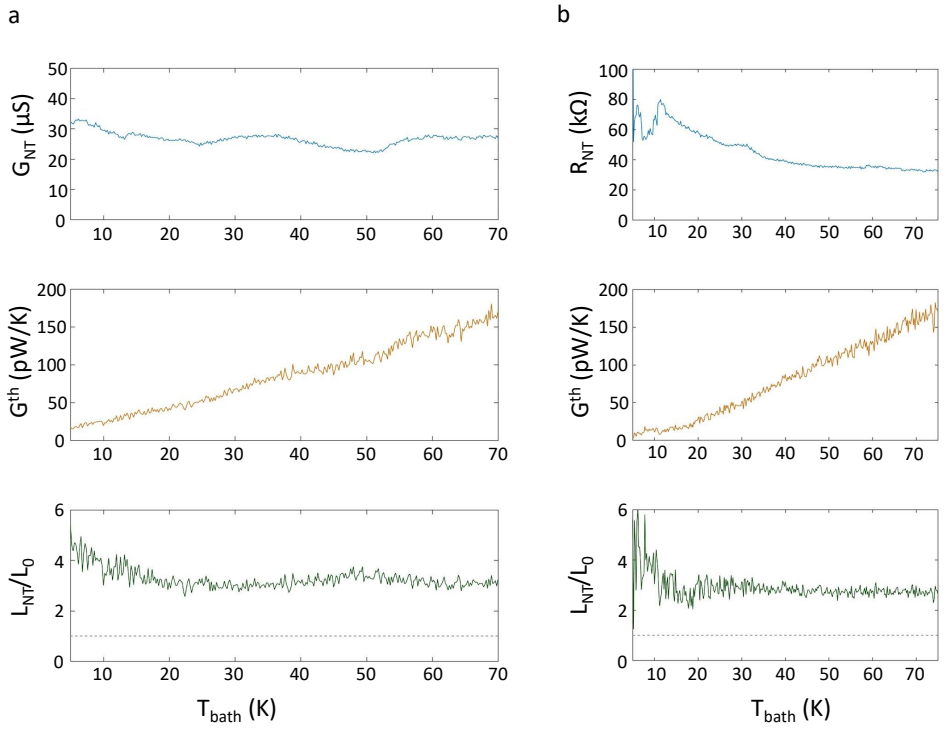

Figure 3.13: Temperature dependence of Device 1 at constant NT doping and thermal bias $\Delta T_H/T_{bath} = 0.1$. (a) G_{NT} (top panel), G^{th}_{NT} (middle), and L_{NT}/L_0 (bottom) as a function of T_{bath} at $V_g^{NT} = 5$ V. (b) Same measurement as (a), with $V_g^{NT} = 10$ V.

Our experiment provides a general guide to some possible connections with the theory.

3.4.5 Plasmon hopping through long-range interactions

In the highly-disordered limit, charge transport can be strongly suppressed. However, long-range Coulomb interactions, which have previously been shown to significantly impact NT behavior[4,141], can open a new channel for energy transfer. We now discuss a new theory for plasmon hopping mediated by long-range Coulomb interactions. The minimal version of the model consists of a 1D conducting electronic system with an impenetrable barrier separating it into two parts. Without electrons passing through the barrier, there is no energy transport via hot electrons, the typical heat flow channel accounted for by the WF law. However, long-range Coulomb interactions can mediate energy transfer across the barrier even without electrons tunneling through it. Specifically, plasmons (density fluctuations) from the hot side couple to electrons across the barrier and induce density fluctuations in turn, generating an energy current. This is schematically depicted in the inset of Figure 3.14(b). This energy current depends on the temperatures on each side of the 1D conductor as

$$Q \propto T_H^2 - T_C^2, \tag{3.12}$$

which is modified to $Q \propto T_H^4 - T_C^4$ when the model accounts for screening from a nearby metal gate.

We can test the applicability of this model to our NT bridge devices by performing nonlinear thermal transport measurements, shown in Figure 3.14. Previous measurements shown had small thermal bias relative to bath temperature ($\Delta T_H / T_{bath} \lesssim 1$) to ensure the system remained in the linear response regime. Analogously to an electrical current-voltage curve measurement, we measure the NT energy current Q_{NT} up to a large thermal bias ΔT_H. In Figure 3.14(a), showing Q_{NT} as a function of $\Delta T_H / T_{bath}$ for Devices 1 and 2 at representative local NT gate voltages and

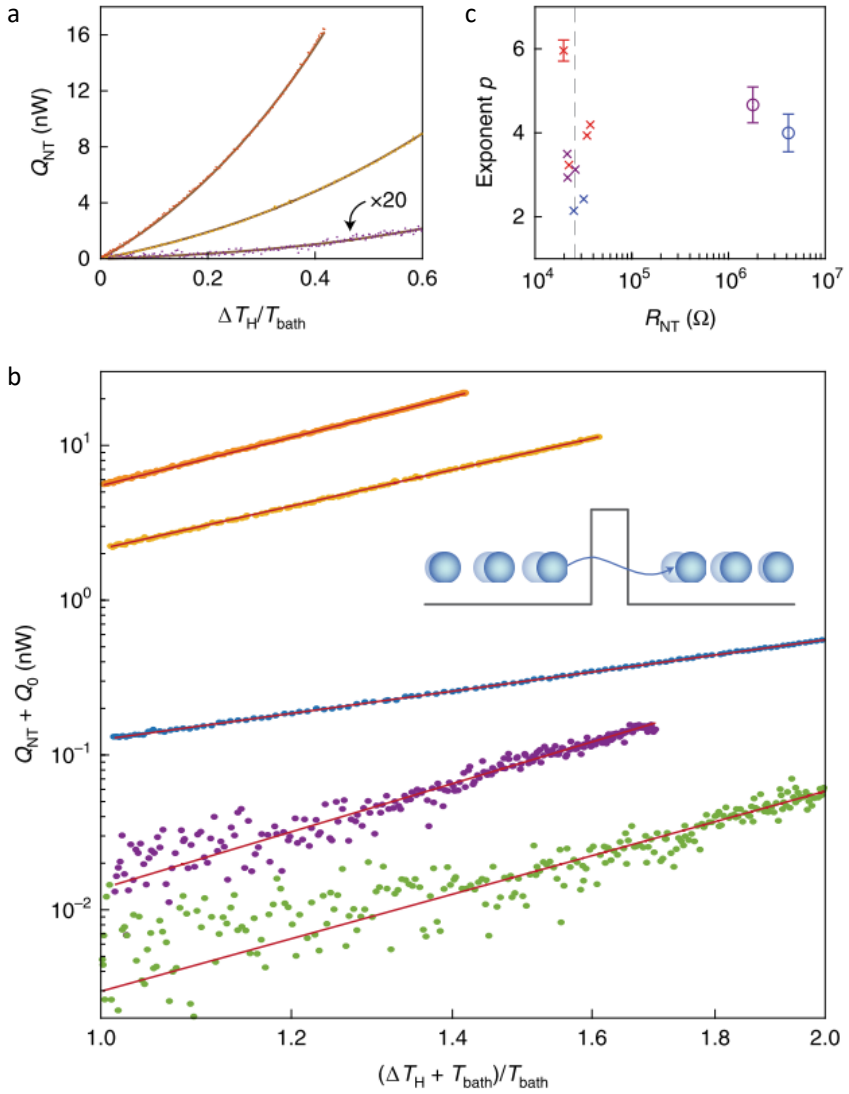

Figure 3.14: (a) Thermal current across the NT, Q_{NT}, as a function of scaled thermal bias $\Delta T_H/T_{bath}$ for Device 1 at $T_{bath} = 70$ K and $V_g^{NT} = 0$ V (orange) and $T_{bath} = 40$ K and $V_g^{NT} = -10$ V (yellow), and for Device 2 at $T_{bath} = 50$ K and $V_g^{NT} = -19.4$ V (purple, multiplied by 20 to enable comparison with Device 1 data). The brown lines are fits to the plasmon hopping model. (b) Log-log plot of NT thermal current versus thermal bias. Orange, yellow and purple data sets are those shown in (a); also shown are data from Device 1 with $T_{bath} = 6$ K and $V_g^{NT} = -10$ V (blue) and from Device 2 with $T_{bath} = 30$ K and $V_g^{NT} = -19.9$ V (green). Red lines are fits to the plasmon hopping model. Inset: schematic of plasmon hopping process. (c) Exponents extracted from the plasmon hopping model fit versus R_{NT} for Device 1 (crosses) at $T_{bath} = 6$ K (blue), 40 K (purple), and 70 K (red), and Device 2 (circles) at $T_{bath} = 30$ K (blue) and 50 K (purple). Symbols without error bars have statistical error smaller than the symbol size. Dashed vertical gray line is at $R_{NT} = h/e^2$.

bath temperatures, we see a clearly superlinear increase in Q_{NT} for all data sets. Figure 3.14(b) relates these measurements to the plasmon-hopping model via a log-log plot of $Q_{NT} + Q_0$ versus $(\Delta T_H + T_{bath})/T_{bath}$, where $Q_0 = a T_{bath}^p$ is a fitting parameter, and a is the proportionality constant in $Q \propto T_H^p - T_C^p$. The fits to the plasmon hopping model in Figure 3.14(a-b) are excellent, with the linearity in (b) particularly suggesting well-defined power law behavior for Q_{NT}. Figure 3.14(c) shows the exponents p extracted from the slopes of these linear fits, which is between 2 and 6 and varies with the NT resistance R_{NT}. For Device 2, which has a more resistive NT such that $R_{NT} \gg h/e^2$, we find $p \approx 4$, as predicted by the plasmon hopping model. This suggests that when direct electron transport is highly suppressed, plasmon hopping with screened long-range Coulomb interactions is an important contribution to energy transport through the bridge. For Device 1, the NT is more conductive ($R_{NT} \approx h/e^2$) and p is typically between 2 and 4. Since electron transport is significant in this regime, further theoretical consideration will be required to fully explain the behavior. Our experiments do not correspond well with an existing theory for a disordered Luttinger liquid with only short-range interactions [140], which predicts $Q \propto (T_H - T_C)^{4/3}$ and would give $p < 2$. There is also one point at high NT conductance and high temperature that gives $p \approx 6$, suggesting yet additional mechanisms for energy transport beyond the theories considered. These results highlight the need for further study of the relationship between long-range interactions and electronic and heat transport in 1D systems.

3.5 Outlook

Through the measurements described in this chapter, and even more extensive experiments with monolithic graphene devices, we have seen that it is possible to non-locally measure voltage noise induced by electronic heat transport. Graphene noise thermometers enable highly-sensitive measurements of electronic thermal transport in 2D van der Waals materials, 1D carbon nanotubes, and

0D localized systems (the highly-resistive regime of NTs), in which we found evidence of interaction effects changing the energy transport behavior. This technique makes it possible to study electronic thermal transport in an array of low-dimensional systems. With careful consideration of their coupling to the graphene thermometers, this thermometry method could provide insight into energy transport in a wide variety of quantum materials.

The universe is full of magical things patiently waiting
for our wits to grow sharper.

Eden Phillpotts

4

Toward realization of the Sachdev-Ye-Kitaev model in graphene

In the preceding chapters, we have seen that disorder played an accidental but important role in the physical phenomena we were able to study. In the nanotube-graphene Coulomb drag experiments, disorder led to high resistances in the nanotubes and suboptimal graphene carrier mo-

bility, restricting the temperature ranges for our measurements and reducing the chances of conclusively observing signatures of hydrodynamics. In the thermometry experiments, disorder along the nanotube bridge created barriers to electron flow that could be overcome by the energy current via Coulomb-coupled plasmons.

Some degree of disorder is all but inevitable in a real mesoscopic sample, and it is usually regarded as a negative factor to be minimized. However, recent theory work [142,143] suggests that engineered disorder in a small graphene flake may, when tuned into a particular regime, enable us to experimentally realize truly exotic and novel quantum physics: the Sachdev-Ye-Kitaev (SYK) model. Inspired by these calculations and later predictions for specific charge and energy transport signatures of SYK physics [144], we made etched graphene quantum dot devices and studied the electrical conductance and thermopower in the $n = 0$ Landau level of the quantum Hall regime, where SYK physics was predicted to occur. This represents the first experimental attempt to generate SYK physics in a mesoscopic system.

4.1 "Black hole on a chip:" the Sachdev-Ye-Kitaev model

The SYK model [63,64] describes a strongly-interacting, many-body quantum system in which all of the constituent excitations (spinless fermions in the original version of the model proposed by Sachdev and Ye [63], Majorana fermions in Kitaev's later modification [64]) are at the same energy and have random, all-to-all interactions. The complex fermion version of the model is described by the Hamiltonian [142]:

$$\mathcal{H}_{SY} = \sum_{ijkl}^{N} J_{ijkl}\, c_i^\dagger c_j c_k^\dagger c_l - \mu \sum_j c_j^\dagger c_j, \tag{4.1}$$

where N is the number of fermions, $c_i^{(\dagger)}$ are fermionic annihilation (creation) operators, μ is the chemical potential, and J_{ijkl} are zero-mean complex random variables that satisfy $J_{ijkl} = J_{klij}^*$ and $J_{ijkl} = -J_{jikl} = -J_{ijlk}$. In the limit of large N, the model is exactly solvable and describes a non-

Fermi liquid (NFL) state, meaning the properties deviate from the expectations of Fermi liquid theory due to strong quantum fluctuations near the Fermi surface [145]. This leads to exotic behavior such as non-vanishing entropy in the low-temperature limit [144,146]. The SYK model has generated tremendous interest among diverse subsets of the physics community, due to its potential applicability to quantum critical phases in high-temperature superconductors, quantum information, and quantum gravity.

A widely-found feature of unconventional superconductors, such as the cuprates, is a region of linear-in-temperature resistivity over a broad range of temperatures above the superconducting dome at T_c, known as the strange metal phase. Since the boundary between the superconducting phase and the strange metal is defined by balancing the free energies of each phase, understanding strange metals is key to unlocking the secrets of high-T_c superconductors. Strange metals have also been suggested as a form of "holographic quantum matter" or "matter without quasiparticles" [65]. Typical metals (described by Fermi liquid theory) have well-defined quasiparticles: long-lived, low-energy elementary excitations which can be combined to create composite excitations. As a simple example, an electron and a hole can pair to form an exciton; however this framework can be used for much more complex and unusual composite excitations, such as composite fermions in the fractional quantum Hall regime [60].

What, then, is "matter without quasiparticles?" To understand this, we can think about the characteristic behavior of quasiparticles. Part of our concept of quasiparticles as well-defined excitations is that they can collide with each other and eventually come into local thermal equilibrium, with a characteristic timescale τ_{eq}. We can also think of this timescale as the time after which local quantum phase coherence will be lost after a quasiparticle is initially created by an external perturbation [65]. Using Fermi's golden rule, it can be shown that this timescale has a $1/T^2$ divergence as $T \to 0$:

$$\tau_{eq} \sim \frac{\hbar E_F}{(k_B T)^2}. \tag{4.2}$$

This leads to the $\rho \propto T^2$ resistivity observed in (metallic) Fermi liquid systems[29]. In a system where the elementary excitations are *not* well-defined quasiparticles, τ_{eq} could conceivably be much shorter. A lower bound on τ_{eq} has been proposed from several angles. One approach, derived from quantum chaos[66], relates it to the Lyuapunov time τ_L, which is the characteristic timescale for a chaotic quantum many-body system to lose all information about its initial state; a hallmark of chaotic systems is that measurements of an observable with an infinitesimal difference in initial conditions will diverge as $\sim\exp(t/\tau_L)$. The theoretical lower bound on τ_L is[65,66]:

$$\tau_L \geq \frac{1}{2\pi}\frac{\hbar}{k_B T}. \tag{4.3}$$

Separately, observations of T_c in a wide range of unconventional superconductors[147] revealed a simple relationship between T_c, the superfluid density ρ_c (essentially, the strength of the superconducting state at $T = 0$), and the electrical conductivity σ measured at roughly T_c; namely, $\rho_c \propto \sigma(T_c)T_c$. By recasting ρ_c and σ in terms of the superconducting and normal state plasma frequencies, respectively, one finds that the characteristic timescale for dissipation near T_c is set by the temperature and Boltzmann's and Planck's constants[148]:

$$\tau(T_c) \approx \frac{1}{2\pi}\frac{\hbar}{k_B T_c}. \tag{4.4}$$

This empirical relation tells us that these strange metal systems have "Planckian dissipation," approaching the quantum speed limit for how fast the energy of their excitations can be turned into heat. Linear-in-temperature resistivity and Planckian or near-Planckian dissipation have since been observed in a wide range of systems[149,150,151], including above the superconducting dome in magic-angle twisted bilayer graphene[152]. Understanding the origins of this remarkably simple relationship is a key motivation in the study of strange metals. It also holds a great deal of interest for quantum

information physicists probing the limits of entanglement processes and thermalization in quantum systems[153].

The discussion in the last few paragraphs has relied on general definitions of matter without quasiparticles (a system in which $\tau_{eq} \sim 1/T$ as $T \to 0$) and empirical laws for some of their characteristics (Planckian dissipation), without reference to a specific model that describes these systems. In fact,there are two theoretical systems that exactly reach the lower bound on τ_{eq} given by Eq. 4.3: the SYK model, and the holographic duals* of black holes in many theories of quantum gravity[65,146,154]. Given their close connection, realizing the SYK model in a condensed-matter system could provide some insight into quantum gravity (which is otherwise extremely difficult to experimentally test), in addition to maximally-chaotic quantum systems more broadly and strange metals in particular.

4.1.1 Realizing the SYK model in a graphene dot

While the SYK model is predicted to describe several quantum systems of interest, there has not yet been an experiment that explicitly realizes the SYK or SY Hamiltonian (Eq. 4.1) in a condensed-matter system. There have been numerous proposals for possible condensed-matter SYK platforms, including ultracold atomic gases[155], arrays of semiconducting wires (with Majorana fermions localized on the ends of each wire) coupled to a disordered quantum dot[156], and 3D topological insulators proximitized with a thin superconducting film[157]. Recently, nuclear magnetic resonance experiments on short spin-1/2 chains[158] that were engineered to simulate the SYK Hamiltonian with $N = 8$ Majorana fermions successfully demonstrated some key signatures of NFL dynamics, including instability with respect to certain types of four-fermion perturbations[159]. We focused on a proposed realization of the Hamiltonian in a more familiar system: graphene.

*Holography duality refers to two systems that are related by the holographic principle, which states that quantum gravity degrees of freedom in a d-dimensional space–time can be represented by a many-body

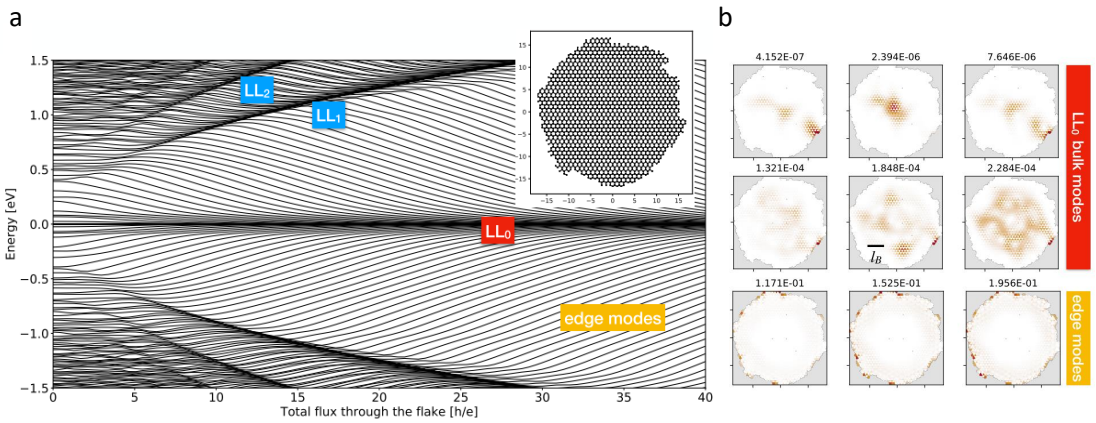

Figure 4.1: (a) Single-particle energy levels as a function of magnetic flux Φ, calculated for a small graphene flake (inset). The $n = 0$ LL is labeled LL_0. (b) Typical wavefunction amplitudes $\Psi_j(\vec{r})$ inside the $n = 0$ LL at $\Phi = 40\Phi_0$ (bulk modes) and outside (edge modes). Numbers above each panel display the energy of the state in eV, and the scale bar shows the magnetic length $l_B = \sqrt{\hbar c/eB}$ Adapted from Ref. 142.

In 2018, Chen *et al.* [142] predicted based on symmetry arguments and numerical simulations that, for a small graphene flake with an irregular boundary in a strong perpendicular magnetic field, the behavior of the electrons in the $n = 0$ Landau level (LL) is described by the complex SYK model. As mentioned in Chapter 1, the $n = 0$ LL of graphene is is a flat band that is particularly robust to disorder due to chiral symmetry, making it a promising starting point for generating SYK physics. Working in this topologically-protected flat band should minimize the most important perturbation that would typically prevail over the SYK interaction, the two-fermion coupling term $\mathcal{H}_2 = \sum_{ij} K_{ij} c_i^\dagger c_j$ (where K_{ij} is the two-body interaction strength). The theory of Aharonov and Casher [57] showed $N_0 = BA/\Phi_0$ zero-energy states in the LLL, where A is the flake area and $\Phi_0 = h/e$ is the magnetic flux quantum. An irregular boundary on the flake brings in a source of randomness that can approximately preserve chiral symmetry [142,154]; in a small enough flake, this randomizes the spatial structure of the electronic wavefunctions throughout the bulk of the flake, as shown in Figure 4.1(b). The Coulomb potential $V(r)$ generates the leading-order term in the

system defined on its $(d-1)$-dimensional boundary. [154]

Hamiltonian, which in the absence of $\mathcal{H}_2$ has the exact form of the SY Hamiltonian (Eq. 4.1) with

$$J_{ijkl} = \frac{1}{2} \sum_{\vec{r_1}} \sum_{\vec{r_2}} \Psi_i^*(\vec{r_1}) \Psi_j^*(\vec{r_2}) V(\vec{r_1} - \vec{r_2}) \Psi_k(\vec{r_1}) \Psi_l(\vec{r_2}), \tag{4.5}$$

where $\Psi_j(\vec{r})$ are the electronic wavefunctions and without loss of generality $V(r)$ can take the form of the Yukawa potential describing screened Coulomb interactions,

$$V(\vec{r}) = \frac{e^2}{\varepsilon r} e^{-r/\lambda}, \tag{4.6}$$

with dielectric constant ε and screening length λ. The simulations of Chen *et al.* found that the resulting J_{ijkl} were sufficiently random[†] to produce many-body level statistics characteristic of a chaotic system, and saturating (near-constant above $T = 0$) entropy, critical hallmarks of the SYK model. These simulations were carried out for an extremely small flake ($\sim$ 10 nm diameter) in a much larger magnetic field ($\sim$ 3200 T) than is reasonably achievable, in order to produce sufficient magnetic flux through the flake to generate a large number $N \approx N_0$ of SYK modes. However, they predicted that their results could be straightforwardly rescaled to larger flakes. More recent theoretical work [161] modeling 60-100 nm diameter flakes in magnetic fields up to 20 T suggests some important qualitative differences in this more experimentally-accessible regime. Notably, the $E \sim \sqrt{B}$ LL spectrum is replaced by a more quantum-dot-like energy distribution, although there remains a flat band of states at zero energy that does not shift with B. Their simulations still showed spatially randomized wavefunctions and sufficiently strong and random four-fermion interactions J_{ijkl} to expect that SYK physics could be observed in a graphene quantum dot flake under realistic experimental conditions.

[†]This work shows that J_{ijkl} have zero mean and are statistically uncorrelated pairwise, but not necessarily at higher orders [160]. The numerical studies nonetheless reproduce key features of the SYK model.

4.2 Theoretical predictions for transport observables of an SYK dot

Since an experimental realization of the SYK model in a small graphene flake seems within reach, the next question is how to measure it. Various theoretical studies of an island or "dot" of SYK matter with N SYK modes coupled to some number M of peripheral "normal" Fermi liquid conducting modes [143,144,162,163] (schematically depicted in Fig. 4.2(a)) suggest it is important to have $N > M$ and for the coupling to the peripheral Fermi liquid modes to be not too strong; typical models take SYK-FL tunneling strength $V \leq J/2$, where $J = \sqrt{2}N^{3/2}\langle J_{ijkl}J^*_{ijkl}\rangle^{1/2}$ is the normalized real-valued strength of the SYK interaction. In realistic systems, SYK physics is expected to exist at intermediate temperatures, where the thermal energy k_BT is smaller than J, but J is larger than all of several possible lower cutoff energy scales. First of all, $J > k_BT > E_{coh} = t^2/J$, where t is the bandwidth of single-particle states in the dot; if $k_BT < E_{coh}$, the system contains coherent quasiparticles and is described by FL physics. A further requirement is $J > t$; otherwise SYK physics will not appear at any temperature. Second, $J > k_BT > E_C$, where $E_C = e^2/C$ is the charging energy (C is the capacitance of the dot). For $k_BT < E_C$, Coulomb blockade begins to impact the behavior, although it does not necessarily preclude observation of SYK physics [144,162]. Finally, $k_BT > J/N$; the opposite limit represents a different regime of quantum criticality dominated by Schwartzian quantum gravity fluctuations [144,164]. These criteria inform the experimental design discussed in Section 4.3.

To distinguish between the regimes dictated by these energy scales, we are concerned with the temperature dependence of quantities that can be measured with transport experiments; some key theoretical predictions for this system from Ref. 144 are shown in Fig. 4.2 (b) and (c). Electrical conductance is one of the simplest transport characteristics to measure, and is expected to scale as $\sigma \sim 1/\sqrt{JT}$ in the SYK regime (Fig. 4.2 (b)). While this is different from a pure Fermi liquid ($\sim 1/T^2$), this temperature scaling is not nearly as distinctive as that of the thermopower S (Fig. 4.2 (c)). In the "pure SYK" regime, the expectation is $S = \frac{4\pi}{3e}\mathcal{E}$, where $\mathcal{E}$ is the electron-hole asymmetry

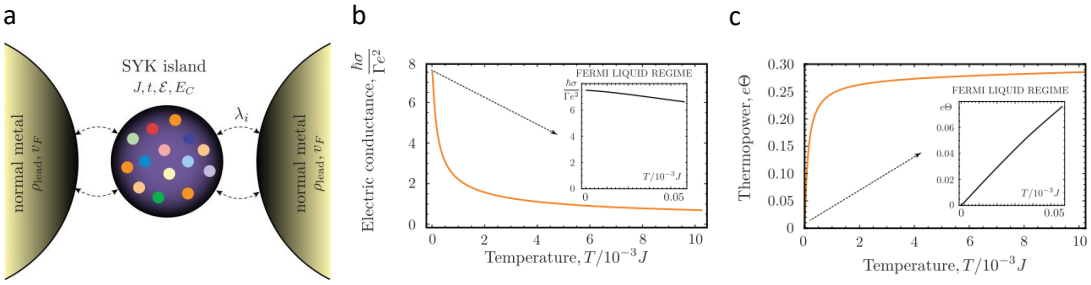

Figure 4.2: (a) Schematic of an island of SYK matter with random four-fermion interaction of mean-squared strength J, electron-electron hopping of strength t, dimensionless particle-hole asymmetry parameter $\mathcal{E}$, and charging energy E_C. It is coupled to normal metal leads by hopping λ_i, characterized by an energy scale $|\lambda_i|^2 \times$ (DOS in leads). (b-c) Crossovers in electrical conductance (b) and thermopower (c) from the SYK regime at $T > E_{coh}$ to the FL regime at $T < E_{coh}$. Calculation assumes $T, E_{coh} \gg E_C, J/N$. Adapted from Ref. 144.

in the SYK model [146,144,162] defined by the derivative of entropy $\mathcal{S}$ with respect to carrier density $\mathcal{Q}$: $d\mathcal{S}/d\mathcal{Q} = 2\pi\mathcal{E}$. Since $\mathcal{E}$ is a temperature-independent constant of the system (for any particular carrier density), this relation directly connects the finite low-temperature entropy of SYK system to the temperature-dependent thermopower (although when $k_B T < t^2/J$, the system enters the FL regime and the thermopower regains the typical FL temperature dependence $S \sim T$). It should be noted that that the predicted behavior shown in Fig. 4.2 assumes $E_{coh} \gg E_C, J/N$ in order to produce FL behavior at low temperature; the predictions are modified if this assumption breaks down, but the thermopower remains a relatively robust signature of SYK physics [144]. If we can meet the energy scale and other coupling strength criteria, measurements of the electrical conductance and thermopower as a function of temperature should provide good evidence of SYK physics in a graphene quantum dot.

4.3 Experimental design and dot device fabrication

Based on the considerations discussed in previous sections, we can delineate a set of requirements for a graphene quantum dot device in which we hope to realize the SYK model. The "bulk" of the dot should be clean, to minimize the single-particle bandwidth t and reduce chiral symmetry-breaking disorder, but the edges should be irregular in order to create randomness in J_{ijkl}. The dot should be large enough that a significant number of SYK modes $N \sim BA/\Phi_0$ can be generated by easily-available magnetic fields ($B \leq 10$ T), yet small enough that the disordered edges can still randomize the electronic wavefunctions throughout the bulk of the flake. We should attempt to minimize the charging energy E_C. Finally, the dot must be somewhat weakly coupled to two reservoirs with a small ($M < N$) number of conducting modes to probe the transport of charge and heat across the dot.

These requirements are well-met by a quantum dot defined by reactive ion etching a rounded constriction in a graphene Hall bar, with bottom and etch-separated top graphite layers to enable independent control of the carrier densities in the dot and two coupled reservoirs. A schematic of the fabrication process and device concept are shown in Figure 4.3(a-d), along with images of a final device (4.3(e-f)). We have already noted that encapsulation of graphene in hBN significantly increases carrier mobility[8,9,47]; adding graphite outside of the hBN layers further improves the device quality by screening additional impurities[165,166,167]. Using a relatively thin hBN layer to separate the graphene from the bottom graphite gate, we can increase the capacitive coupling between them and hence reduce E_C. Conventional electron-beam lithography and reactive ion etching methods are known to generate disorder on the edges of etched graphene structures[168,169], and can be consistently used to fabricate etched graphene dots with diameters of approximately 100 nm. This corresponds to roughly $N \approx 30$ to 40 at $B = 10$ T. The remaining sections of the Hall bar on either side of the dot are used as reservoirs of normal FL charge carriers. By etching away the top graphite

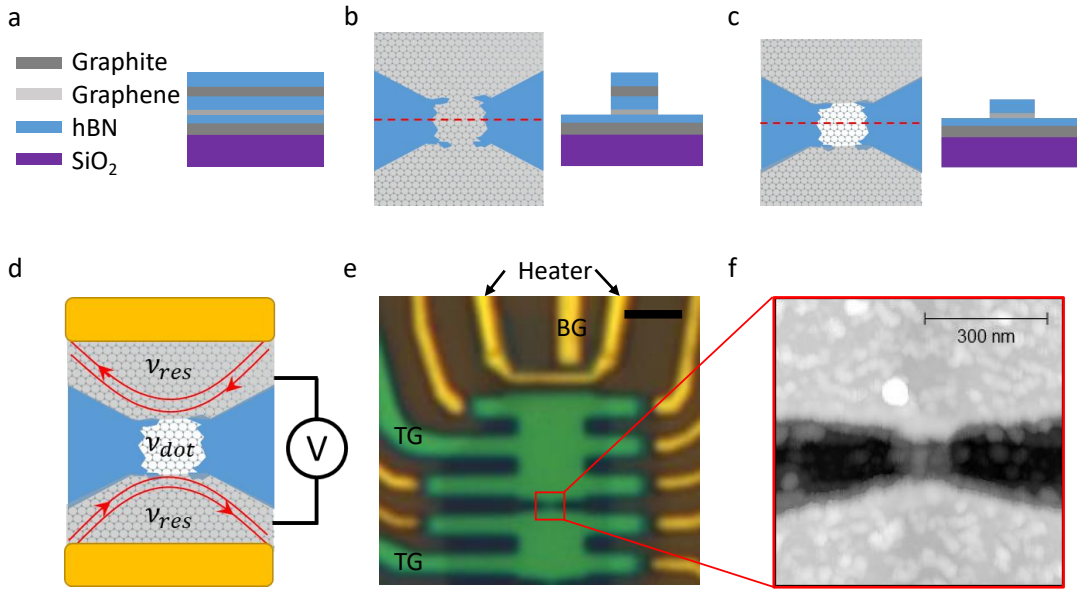

Figure 4.3: (a-c) Schematics of dot fabrication process. (a) Stack of van der Waals flakes used for the device: cover hBN, top graphite, top hBN, graphene, bottom hBN, bottom graphite (listed from top to bottom), resting on SiO_2/Si substrate. (b) Detail of dot definition by etching away cover hBN, top graphite, top hBN, and graphene, leaving an island of graphene connected to two larger graphene reservoirs. A cross-section of the etched stack along the red dashed line is shown at right. (c) Detail of definition of separate reservoir top gates and ungated dot region by etching cover hBN and top graphite above dot, with cross-section. (d) Simplified schematic of device operation: separate top gates independently tune the filling factors of the dot and reservoirs (ν_{dot}, ν_{res}), and measurement of the voltage across the dot upon application of electrical bias (temperature gradient) enables extraction of the electrical conductance (thermopower). (e) Optical micrograph of an example device, with indications of substrate heater and bottom gate (BG) and top gate (TG) contacts. Scale bar is 2 μm. (f) Atomic force microscopy image of the red-outlined region in (e), showing etched dot and separation of reservoir top gates.

gate above the dot, we can separately tune the carrier densities of the dot and reservoirs such that, in an applied magnetic field, the dot remains in the $n = 0$ LL ($|\nu_{dot}| < 2$) and the reservoirs can be set at constant integer quantum Hall filling (for example $\nu_{res} = 2$, where $\nu_{dot(res)}$ is the LL filling factor of the dot (reservoir)). This provides a small number of charge-carrying modes to probe the dot ($M = 2\nu_{res}$), which can be easily kept with $N > M$ at accessible magnetic fields. The coupling between the dot and reservoirs can be tuned by adjusting their relative carrier densities as well. For this device geometry, estimates of the relevant energy scales [142,143,144,161] give $t \sim 0.35$ to 1 meV and $J \sim 3$ meV, corresponding to lower cutoff energy scales t^2/J and J/N both around 1 K and an upper energy scale of around 30 K, a temperature range easily accessible in liquid helium cryostats. The charging energy E_C can vary significantly between devices, as it is determined by the dot size and coupling to the graphite gates through the hBN dielectric layers.

We should note that numerous previous experiments have studied etched graphene quantum dots [169,170], including in high magnetic fields [171,172,173,174], yet did not report any of the signatures of SYK physics that we seek. Part of the explanation may be that the majority of this work was carried out prior to the advent of hBN encapsulation, with devices resting on SiO_2 substrates; too much charged bulk disorder could have broadened all of the LLs too much to satisfy $J > t$. Another factor is that the studies carried out with applied magnetic field did not include temperature-dependent measurements, as they were focused on the evolution of the Coulomb blockade behavior. Some earlier work [169] demonstrated energy level statistics characteristic of chaotic Dirac billiards, but was carried out in zero magnetic field. More recent studies of graphene quantum dots have shifted toward electrostatically-defined dots in graphene [175,176,177,178,179], in order to access single-electron physics that is highly sensitive to disorder. While an intriguing area of study, this is movement away from the putative SYK regime.

4.3.1 Device fabrication

Many of the details of the fabrication process are the same as for other graphene-based devices detailed in Sections 2.3 and 3.3. Graphene, graphite and hBN are mechanically exfoliated. Thicknesses of all of the van der Waals flakes except for graphene (i.e. hBN and graphite) are confirmed using atomic force microscopy; monolayer graphene thickness is determined from optical contrast with the 285 nm SiO_2 substrate[95]. As before, a large hBN flake is picked up with a PPC film on a PDMS stamp. This "cover hBN" flake is used to pick up subsequent layers: top graphite, top hBN, graphene, bottom hBN, and bottom graphite. The final stack is represented in Fig. 4.3(a). We use "top hBN" to denote the layer separating the graphene from top graphite to remain consistent with the nomenclature for "bottom hBN" separating graphene from bottom graphite. The "cover hBN" is necessary if using PPC, since PPC will not pick up graphite. Some other polymers, such as polycarbonate (PC) can pick up graphite as the first layer, in which case the cover BN can be omitted. The PPC and stack were detached from the stamp by heating to 150 °C to melt the PPC, which is then removed by high-temperature vacuum annealing.

The e-beam lithography and etching processes were slightly modified from previous devices to incorporate the graphite gates and improve the resolution and selectivity of several steps. We use a higher acceleration voltage lithography tool (125 kV as opposed to 30 kV) so as to to reliably create higher-resolution features, such as $\sim$ 100 nm diameter dots. In the first lithography and reactive ion etching step, the cover hBN and top graphite are etched away everywhere except for the region above the future Hall bar and contacts, and a region where the top graphite protruded from the graphene and bottom graphite (to be used for contacting the top graphite without shorting to the other layers). We use chemically-selective reactive ion etching processes to ensure the lower layers would not be affected: SF_6 to etch hBN and a weak (30 W) O_2 plasma for graphene and graphite. Next, we deposit a substrate heater, in the shape of a narrow ($\sim$ 400 nm wide, few-micron long)

rectangle of metal (5 nm Cr/70 nm Au) connected to two wider leads, on top of the stack where the top graphite is etched, with the rectangle running parallel to the shorter end of the future Hall bar and roughly 500 nm from the remaining top graphite gate. By passing a current through the heater, we can create a temperature gradient across the dot, provided that the narrow rectangle is the most resistive part of the heater and thus experiences the most Joule heating. The subsequent nanofabrication steps (definition and deposition of contacts to the graphene and etching the stack into a Hall bar) are the same as described previously, although care must be taken to ensure that the top and bottom graphite layers and the graphene are all contacted separately, and none are shorted to the others. It is necessary to define at least one contact to the bottom graphite gate and at least two contacts to the top graphite gate on opposite sides of where the dot will be defined.

The final steps are removing the top graphite from above the dot region and etching to define the dot. Compared to previous steps in the process, we use different resist recipes baked on a hot plate for a longer period of time (for the gate etch, 950 PMMA A4 spun at 1000 rpm and baked for 10 minutes; for the dot etch, 950 PMMA A4 spun at 5000 rpm and baked for 20 minutes; typical gate or stack etching processes used 950 PMMA A6 spun at 3000-3500 rpm and baked for 2 minutes) to improve the sturdiness of small features in the resist throughout the etching process. The use of the selective etching recipes mentioned above also helps prevent accidentally etching through additional layers of the stack. We first etch a $\sim$ 100 nm-wide line across the width of the Hall bar through the cover hBN (using SF_6) and top graphite (using O_2). The top graphite etch is performed in $\sim$ 30 second steps, stopping when the top graphite has been completely etched, as determined by resistance measurements between the two top graphite contacts between each step (Fig. 4.3(c)). A similar process is used to etch the dot, repeating the etch recipes and required etch times to remove the cover hBN and top graphite, followed by another SF_6 step to remove the top hBN and successive short (15 to 30 second) weak O_2 steps to remove the graphene (Fig. 4.3(b)), stopping once the graphene two-terminal resistance across the dot region increased dramatically (typically from a few

kΩ to tens of kΩ). A final device with a 140 nm wide by 90 nm long dot (as determined by atomic force microscopy) is shown in Figure 4.3(e), with an atomic force microscopy image of the dot region in Figure 4.3(f). For some devices, multiple dots were defined along the same Hall bar, with independent contacts to the top graphite gates for each of the reservoir regions and typically a substrate heater on each end of the device, so that the heater closest to the dot being measured could be used to define the temperature gradient across the dot.

4.4 Electrical and thermoelectric response at zero magnetic field

We will now discuss the results of electrical and thermoelectric transport measurements in etched graphene dot devices. Unless otherwise noted, the data presented are from the device shown in Fig. 4.3(e-f). The dot and reservoirs are separated from the bottom graphite gate by 5 nm of hBN, and the hBN flake separating the reservoirs from the top graphite gate is 18.2 nm thick. The p-doped Si beneath the SiO_2 substrate is used to gate the regions of graphene immediately adjacent to the metal contacts, which are not directly above or below graphite gates to avoid shorting. We refer to the larger reservoir closest to the heater as the "upper" reservoir and the smaller reservoir on the other side of the dot as the "middle" reservoir. There is a second, similar-sized dot and "lower" reservoir with its own heater that was measured independently; the lower reservoir was kept floating during measurements of the upper dot. The measurements were performed in a He-3 cryostat with a base temperature of 345 mK and a maximum magnetic field of 10 T perpendicular to the sample.

Characterization of the electrical transport response for each of the three main regions of the device to the top and bottom graphite gates is shown in Figure 4.4. The resistance through the dot, $R_{dot} = 1/G_{dot}$, is measured using the circuit sketched in Fig. 4.4(a) and shown in Fig. 4.4(b). We see a main diagonal feature with the highest resistance ($\sim$ 100 kΩ) and additional high-resistance regions in two triangles above and below the main diagonal, outside of which the dot resistance drops

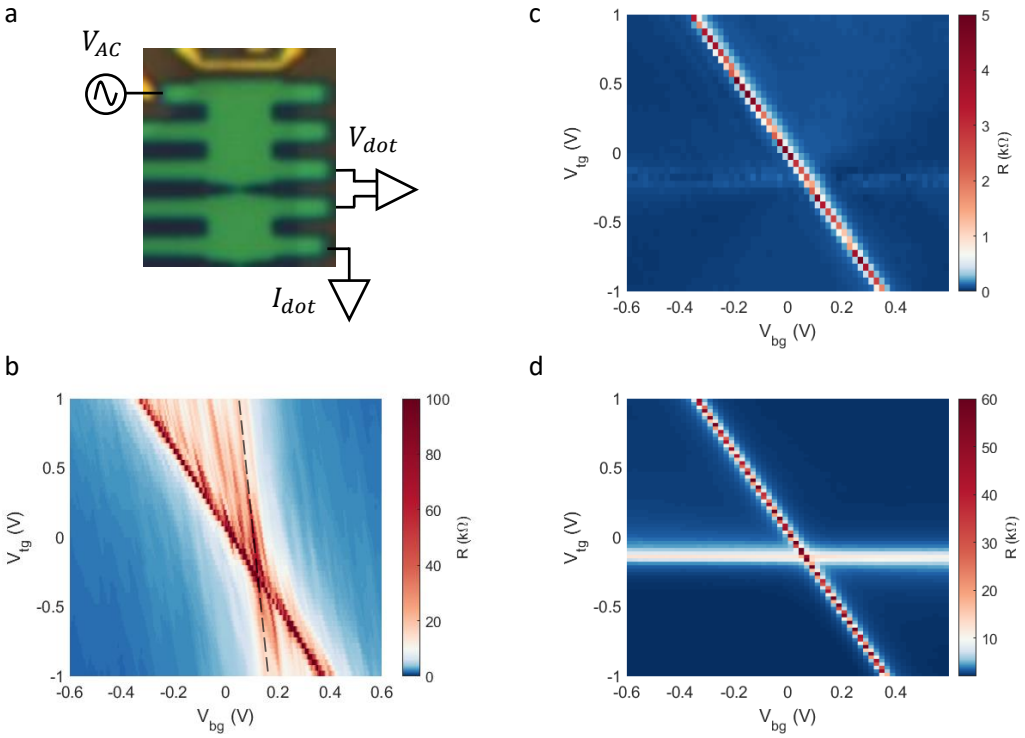

Figure 4.4: Electrical transport in dot and reservoirs at $B = 0$ T, $T = 350$ mK. (a) Schematic of circuit for dot resistance measurements. (b) Four-terminal dot resistance $R_{dot} = V_{dot}/I_{dot} = 1/G_{dot}$, as a function of bottom gate voltage V_{bg} and top gate voltage V_{tg}; silicon gate voltage $V_{Si} = 28$ V. Dashed line indicates approximate charge neutrality in the dot. (c) Four-terminal resistance of upper reservoir as a function of V_{bg} and V_{tg}; silicon gate voltage $V_{Si} = 0$ V. (d) Three-terminal resistance of middle reservoir as a function of V_{bg} and V_{tg} with $V_{Si} = 0$ V. Resistances are higher because one of the voltage probes is the same as the source contact. The resistance peak around $V_{tg} \approx -0.13$ V is caused by a region near the graphene contacts that is overlapped by the top graphite but not the bottom graphite. Increasing V_{Si} dramatically improves the resistance between the reservoirs and metal contacts and was employed for all measurements except those shown in (c-d).

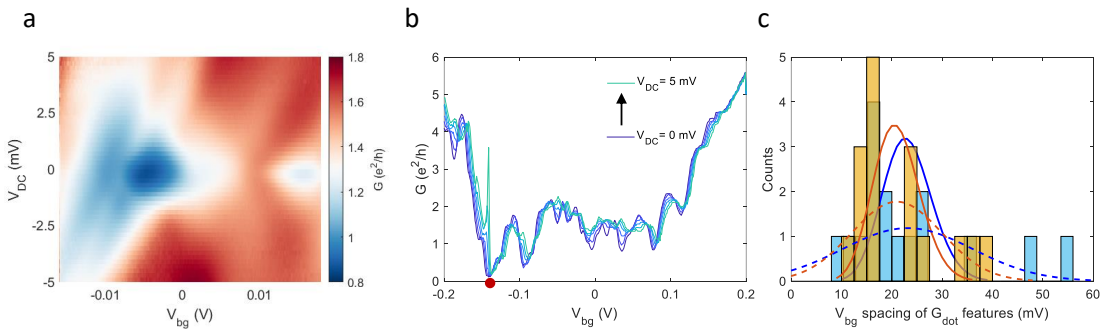

Figure 4.5: Electrical transport at $B = 0$ T with DC bias. (a) Four-terminal dot conductance G_{dot} at $V_{tg} = 0.5$ V as a function of V_{bg} and DC bias voltage V_{DC}. (b) G_{dot} at $V_{tg} = 0.5$ V and several values of V_{DC} as a function of V_{bg} in a wider gate voltage range. The charge neutrality point of the reservoirs is indicated by the red circle. (c) Histogram of spacing of features in (b) data at $V_{DC} = 0$, with peaks in G_{dot} plotted in blue and minima in yellow. Poisson distribution fits (solid lines) and Gaussian fits (dashed lines) are displayed in blue and orange for peaks and minima, respectively.

to $\sim 1\,\mathrm{k}\Omega$. Comparing this to resistance measurements of the reservoirs shown in Fig. 4.4(c-d), we can see that the main diagonal corresponds to the charge neutrality point (CNP) of the graphene reservoirs. We further note that two reservoirs have the same capacitive coupling to the top and bottom gates and essentially the same CNPs and electron mobility ($\sim 60,000\ \mathrm{cm}^2/\mathrm{Vs}$ at high carrier density). The remaining higher-resistance features in Fig. 4.4(b) must therefore have their origins in the dot. The correspondence of the two high-resistance regions on opposite sides of the reservoir CNP, approximately delineated by the reservoir CNP and a nearly-vertical line crossing it (which would correspond to the CNP of the dot region), suggests the peaks and dips in these regions originate from resonances in the dot when it has the opposite carrier type from the reservoirs ("pnp" and "npn" regimes on the left and right sides of the reservoir CNP, respectively)[180]. This also matches expectations based on the device geometry; the carrier density in the dot should be tunable via bottom gate voltage V_{bg}, and relatively insensitive to the top gate voltage V_{tg}, though there will still be some coupling due to fringing electric fields.

To further investigate the resonances in the dot, we measured the four-terminal conductance G_{dot} as a function of V_{bg} and DC bias voltage V_{DC}, shown in Figure 4.5. Focusing on a small range of V_{bg} inside the npn regime (Fig. 4.5(a)), we find that G_{dot} does not display a clearly-defined diamond pattern typical of Coulomb blockade [37,95,169,171,173,174]. In particular, the conductance is never strongly suppressed; expanding the range of V_{bg} under consideration (Fig. 4.5(b)), the only point at which G_{dot} is near zero coincides with the reservoir CNP. This suggests that the features are more like Fabry-Pérot resonances, which have been known to occur in similar electronic "cavity" regions with different electron/hole density than their surroundings [181,182]. As an initial indication of the degree to which chaotic dynamics are important in this dot, we track the spacing statistics as a function of V_{bg} in the npn regime (Fig. 4.5(c)). Level spacing for a non-chaotic quantum dot should be described by the Poisson distribution, whereas for a chaotic system the level spacing statistics should follow one of the Gaussian random ensembles [169,183]. While the number of features we were able to track (determined by the voltages that could be applied to the graphite gates before the hBN dielectric would start to break down) was too small to provide definitive statistics, the distributions seem to fall between the Poisson and Gaussian fits, which is consistent with previous observations of similarly-sized etched graphene quantum dots [169] and suggests an emergence of chaotic behavior in the dot due to disorder. Additionally, the typical feature spacing shows that the dot charging energy E_C is suppressed relative to similarly-sized graphene quantum dots without graphite gates.

We also measured the thermopower in various sections of the device at $B = 0$ T before embarking upon a detailed study of its temperature dependence at high magnetic field. Details of the thermopower measurement technique are given in Appendix B. Briefly, we apply a symmetric AC bias on the substrate heater to generate a temperature gradient ΔT, which we quantify by measuring the lifting of R_{xx} minima in the reservoirs as a function of T_{bath} at zero bias on the heater or of the heater excitation at constant T_{bath}. Since the Joule power in the heater is proportional to I_h^2, measuring the voltage across the dot (or another part of the device with known ΔT) at the second har-

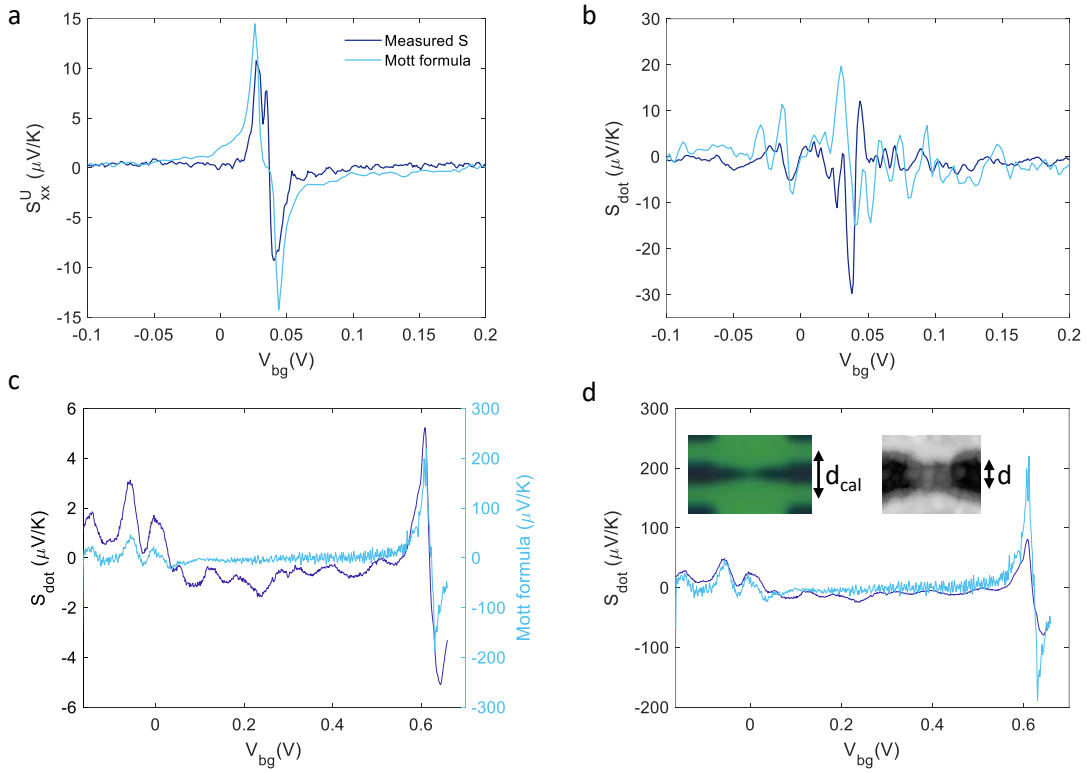

Figure 4.6: Thermopower and comparison to Mott formula at $B = 0$ T. (a) Thermopower in upper reservoir S^U_{xx} (dark blue) and Mott formula calculation (light blue) from measurements at $T = 3$ K and $V_{tg} = 0$ V. (b) Thermopower across dot S_{dot} and corresponding Mott formula calculation from measurements at $T = 3$ K and $V_{tg} = 0$ V. (c) S_{dot} (dark blue, left y-axis) and corresponding Mott formula calculation (light blue, right y-axis) from measurements at $T = 31.4$ K and constant reservoir density $n_{res} = 4.8 \times 10^{11}$ cm^{-2}. (d) Same data as (c) but with S_{dot} rescaled by a factor of 15.55 to account for difference in distance between calibration contacts d_{cal} and actual dot length d, illustrated in inset.

monic of the heater frequency, ΔV_{th}, and dividing by ΔT enables calculation of the thermopower, $S = -\Delta V_{th}/\Delta T$.

Figure 4.6(a) shows the thermopower in the upper reservoir S_{xx}^{U} at $T_{bath} = 3$ K and $V_{tg} = 0$ V. The shape and magnitude are consistent with previous measurements[43,61,184]. We compare the measured thermopower to the semiclassical Mott formula (Eq. 1.13), which can be recast into a more useful form by substituting electrical conductance G for conductivity σ and noting the Fermi energy is tuned by V_{bg}:

$$S_{Mott} = -\frac{\pi^2}{3e}k_B^2 T\frac{1}{G}\frac{dG}{dV_{bg}}\left(\frac{dE_F}{dV_{bg}}\right)^{-1} = -\frac{\pi^2}{3e}k_B^2 T\frac{1}{G}\frac{dG}{dV_{bg}}\frac{2}{\hbar v_F}\sqrt{\frac{e(V_{bg}-V_{bg}^0)}{\pi C_{dot}/A_{dot}}}. \qquad (4.7)$$

For the second half of Eq. 4.7, we have made the additional substitution $E_F = \hbar v_F\sqrt{\pi n_{Gr}} = \hbar v_F\sqrt{\pi(V_{bg}-V_{bg}^0)/e(C/A)}$, where V_{bg}^0 is the bottom gate voltage at the CNP and C/A is the capacitance per unit area. We find good agreement between the measured thermopower and the Mott formula prediction in the reservoir; however, the agreement worsens when repeating the same thermopower measurement across the dot at $T_{bath} = 3$ K (Fig. 4.6(b)). While some of the oscillatory features appear correlated and the overall magnitude is similar, there are significant discrepancies between the Mott formula prediction and the measured signal. Since the Mott relation is often better obeyed by graphene at higher temperatures, we repeated the comparison at $T_{bath} = 31.4$ K and constant reservoir density ($n_{res} = 4.8 \times 10^{11}$ cm^{-2}), with the results shown in Fig. 4.6(c). The thermopower measurement at higher temperature qualitatively showed a much closer correspondence with the Mott formula calculation, but remained roughly the same magnitude as at $T_{bath} = 3$ K, while the Mott relation has conventional scaling of thermopower with temperature, $S \sim T$.

A possible explanation for this quantitative discrepancy could lie in a difference in where the thermal voltage ΔV_{th} experiences its most dramatic change, compared to where we determine ΔT. Since we are measuring at constant n_{res}, the resistance (and thermopower) of the reservoirs is con-

stant, which means all the changes in the ΔV_{th} signal come from the dot. However, we calculate ΔT across the dot based on resistance measurements at the closest pairs of voltage probes in the upper and middle reservoirs, which are $d_{cal} = 1.4$ μm apart. This is much larger than the the "length" of the dot, $d = 90$ nm. The heater has no electrical connection to the graphene and should produce a nearly-linear temperature gradient across the region of interest[61,185,184], so the measured temperature difference ΔT must be rescaled. The same consideration does not apply to the reservoir thermopower measurement in Fig. 4.6(a), since ΔV_{th} and ΔT were measured using the same contacts and there is no constriction or junction between them to cause a more localized voltage drop. When we rescale the measured thermopower by the ratio d_{cal}/d, we find near-perfect agreement in the npn regime (Fig. 4.6(d)) and good agreement elsewhere. Of course, applying such a rescaling to thermopower data at all temperatures would make the disagreement between the measured S_{dot} and Mott relation in Fig. 4.6(b) quantitatively much worse. However, we note that Mott formula violations in this direction ($S_{meas} > S_{Mott}$) have been observed in 100 nm graphene constrictions[186] as a result of scattering from edge disorder, which is precisely what we have engineered in our system. Furthermore, the Mott formula is not necessarily expected to predict the thermopower at finite magnetic field, particularly if the system has entered the SYK regime[144]. For the remaining thermopower data presented in this chapter, we will use the geometrically-determined rescaling factor in reporting measured values of S_{dot}, with the assumption that the appropriate value depends only minimally with B and T. This may impact quantitative agreement with the Mott formula, but not the relative signal or the temperature dependence.

4.5 Dot measurements at finite magnetic field

We will now move on to discuss the behavior of the device in a perpendicular magnetic field. Figure 4.7(a) shows a simplified schematic of the measurement circuit for longitudinal resistance across

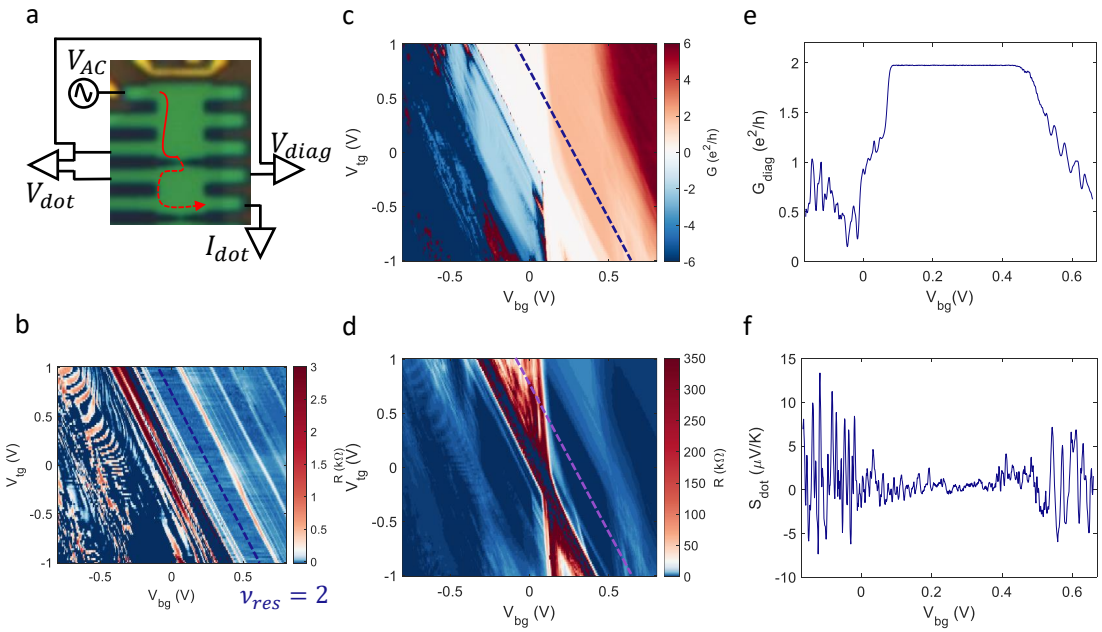

Figure 4.7: (a) Simplified circuit schematic for dot electrical conductance measurements. $R_{xx}^{dot} = V_{dot}/I_{dot}$ contains contributions from the dot and reservoirs, while $G_{diag} = I_{dot}/V_{diag} = \nu_{dot}e^2/h$ for $\nu_{dot} < \nu_{res}$. (b) Upper reservoir R_{xx}^{U} as a function of V_{bg} and V_{tg} at $B = 10$ T, $T_{bath} = 350$ mK, and $V_{Si} = 28$ V. Resistance fluctuations on left side come from pn junctions between the hole-doped main channel and electron-doped contacts. Dashed purple line indicates center of $\nu_{res} = 2$. (c) G_{diag} as a function of V_{bg} and V_{tg} at $B = 10$ T. Dashed purple line is the same as in (b). (d) R_{xx}^{dot} as a function of V_{bg} and V_{tg} at $B = 10$ T. Dashed purple line is the same as in (b). (e,f) Line cuts of G_{diag} (e) and dot thermopower $S_{dot} = \Delta V_{th}/\Delta T$ (f) along the dashed lines in (b-d), plotted versus V_{bg}. V_{tg} was simultaneously varied to maintain constant reservoir filling $\nu_{res} = 2$.

the dot $R_{xx}^{dot} = V_{dot}/I_{dot}$ and the diagonal conductance $G_{diag} = I_{dot}/V_{diag}$. Separate measurements of the longitudinal Hall resistance of the reservoirs at $B = 10$ T (Fig. 4.7(b) for upper reservoir data; similar results were obtained for the middle reservoir) show the expected minima at $\nu_{res} = 2, 6, 10$, with less robust minima at the symmetry-broken integer fillings. Measuring electrical transport through the dot in different configurations, we found that R_{xx}^{dot} (Fig. 4.7(d)) bears an initial resemblance to the zero magnetic field data (Fig. 4.4(b)), with the high-resistance npn regions becoming even more prominent and additional parallelogram-like features of near-zero resistance ($R_{xx}^{dot} \sim 30\ \Omega$) coinciding with parts of the most robust integer fillings in the reservoirs. The dot controls the transmission of quantum Hall edge states from one reservoir to another depending on its doping relative to the reservoirs, acting essentially as a quantum point contact [1,187]. We focus on the diagonal conductance G_{diag} (Fig. 4.7(c)) in the subsequent discussion because, except when $|\nu_{dot}| \gg |\nu_{res}|$, it only depends on the number of edge channels transmitted through the dot: $G_{diag} = \nu_{dot} e^2/h$. Looking at G_{diag} as a function of V_{bg} and V_{tg} at $B = 10$ T, we see near-vertical strips of $G_{diag} \approx 2, 6$ when $\nu_{dot} \leq \nu_{res}$. Regions of quantized conductance for symmetry-broken integer states in the dot are generally less well-defined. Fig. 4.7(e) shows a line cut of G_{diag} through the center of the $\nu_{res} = 2$ region. The reservoir edge states are fully transmitted for a significant range of gate values, resulting in $G_{diag} \approx 2e^2/h$. On either side of this plateau, the conductance drops significantly and displays a series of peaks and dips. Measurements of the dot thermopower S_{dot} along the same line (Fig. 4.7(f)) also show larger-amplitude oscillations in these regions, with a smaller signal coinciding with the $G_{diag} \approx 2e^2/h$ plateau. The thermopower results will be discussed in more detail below.

First, since we are interested in the behavior of the dot in the $n = 0$ LL, it is important to identify the corresponding gate voltage range. By comparing the electrical transport behavior in the quantum Hall regime across the dot (for example, R_{xx}^{dot} shown in Fig. 4.8(a)) and in the reservoirs (for example, G_{xy} in the upper reservoir shown in Fig. 4.8(b)) as a function of the graphite gate volt-

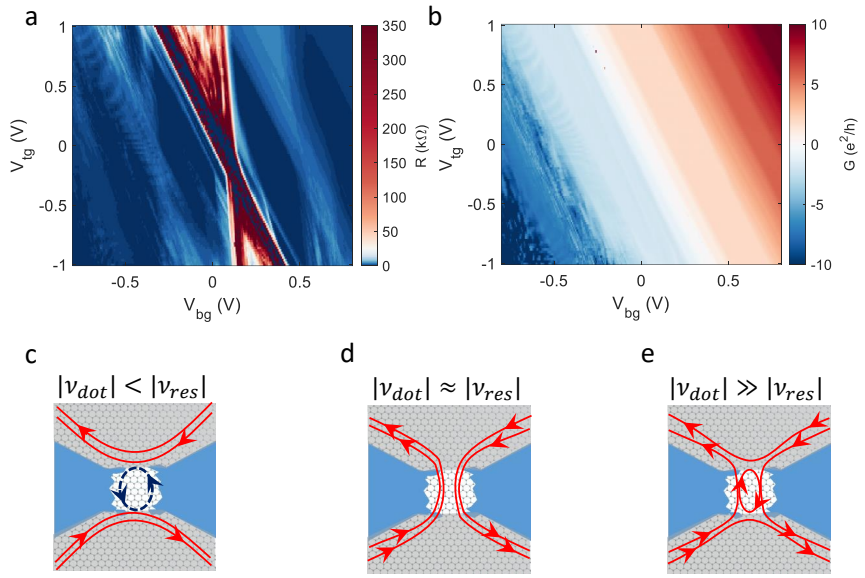

Figure 4.8: (a) R_{xx}^{dot} as a function of V_{bg} and V_{tg} at $B = 10$ T (duplicated for reference from Fig. 4.7(d)). (b) Upper reservoir G_{xy} as a function of V_{bg} and V_{tg} at $B = 10$ T. (c-e) Illustrations of several different regimes of transport through the dot. (c) For $\nu_{dot} < \nu_{res}$, reservoir edge states are completely or partially blocked. (d) For $\nu_{dot} \approx \nu_{res}$, reservoir edge states are fully transmitted. (e) For $\nu_{dot} \gg \nu_{res}$, reservoir edge states are partially reflected.

ages V_{bg} and V_{tg}, we can deduce the filling factor in the dot from its transmission or reflection of quantum Hall edge states impinging on it from the reservoirs. Since the centers of quantum Hall plateaux occur at $B = n_e h/e\nu$[60], and the carrier density in the dot (n_{dot}) and reservoirs (n_{res}) varies as a function of V_{bg} and V_{tg}, we can rewrite this relation to in terms of the relevant parameters:

$$B = \frac{1}{\nu_{dot(res)}} \frac{h}{e} \left(\alpha (V_{bg} - V_{bg}^0) + \beta (V_{tg} - V_{tg}^0) \right), \tag{4.8}$$

where V_{bg}^0, V_{tg}^0 account for shifts of zero carrier density away from zero gate voltage and α, β are constants proportional to the capacitance between the dot (reservoirs) and the bottom and top gates, respectively.

The electrical transport through the dot can be classified into several regimes, illustrated in Fig. 4.8(c-e). When the filling in the dot is small compared to the reservoirs (c), particularly in the npn

regime ($\nu_{dot} < 0$, $\nu_{res} > 0$), there is low transmission of edge states through the dot, except at certain peaks, similar to the npn regime at $B = 0$. For small integer dot fillings with the same carrier type as the reservoirs ($0 < |\nu_{dot}| < |\nu_{res}|$), the dot transmits an integer number of edge states equal to ν_{dot}. When $\nu_{dot} \approx \nu_{res}$ (d), the dot becomes almost completely transparent to the reservoir edge states. For the "nn'n" regime with higher dot filling $|\nu_{dot}| \gg |\nu_{res}|$ (e), the additional electron density in the dot will start scattering the reservoir edges, reducing the conductance, which has also been observed in graphene quantum point contacts [187,188]. Importantly for our efforts to realize the SYK model in the dot, these results demonstrate that the gates can adjust the dot and reservoir fillings such that we can access the $n = 0$ LL in the dot ($|\nu_{dot}| < 2$) and several integer quantum Hall states in the reservoirs. In order to probe the maximum range of filling factors in the dot while remaining in a well-defined quantum Hall state in the reservoirs, we performed most of the electrical conductance and thermopower measurements through the dot at constant reservoir filling $\nu_{res} = 2$.

We return to examine the electrical and thermoelectric transport at varying n_{dot} and B, shown in Figure 4.9 for $\nu_{res} = 2$. The x-axis of these plots is given in terms of V_{bg}; the top graphite gate voltage V_{tg} is simultaneously adjusted to keep the reservoirs at constant filling, with the exact relation between V_{bg} and V_{tg} changing at each B. The G_{diag} measurement (Fig. 4.9(a)) shows both reservoir edge states are transmitted through the dot in a fairly wide range of densities down to $|B| \approx 4$ T. The npn and nn'n regimes show shifting patterns of oscillations as a function of B and V_{bg} ($\propto n_{dot}$), reminiscent of previous studies of larger quantum Hall pn and npn junctions [189]. At lower magnetic fields, the region of maximal conductance through the dot shrinks and the transport becomes completely dominated by oscillations.

We can apply the Mott formula (Eq. 4.7) to these data and compare the result to our measurements of S_{dot} in the same range of carrier density and magnetic field (Fig. 4.9(b) and (c), respectively.) While the magnitudes differ significantly, partly due to the ΔT calculation and rescaling questions discussed in Section 4.4, many patterns in the thermopower exhibit similarity between

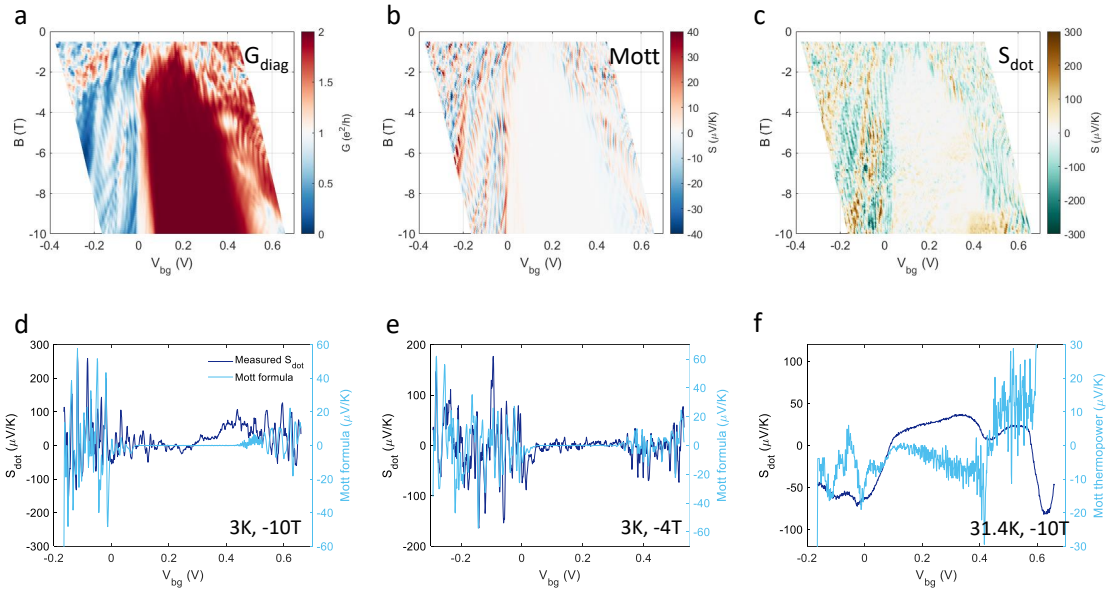

Figure 4.9: (a-c) Evolution of G_{diag} (a), Mott formula calculation for S_{dot} (b), and measured S_{dot} (c) as a function of V_{bg} and B, with V_{tg} simultaneously varied to keep the reservoirs at constant filling $\nu_{res} = 2$. Measurements were taken at $T_{bath} = 3$ K, $\nu_{res} = 2$, $V_{Si} = 20$ V. (d-f) Comparison line scans of measured S_{dot} (dark blue, left y-axis) and Mott formula calculation (light blue, right y-axis) with $\nu_{res} = 2$ at various T_{bath} and B. (d) $T_{bath} = 3$ K, $B = -10$ T. (e) $T_{bath} = 3$ K, $B = -4$ T. (f) $T_{bath} = 31.4$ K, $B = -10$ T. Thermopower data in (c-f) has been scaled using the geometric factor illustrated in Fig. 4.6(d).

the calculation and the measurement. In the same region where $G_{diag} \approx 2$ and $R_{xx}^{dot} \approx 0$, the thermopower is approximately zero; this makes intuitive sense, as a voltage change should not appear when the quantum Hall edge states can move unimpeded through the dot. We also observe many similar patterns in the oscillations in the npn and nn'n regimes. Taking a closer look at the correspondence by examining line cuts as a function of V_{bg} at $B = -10$ T (Fig. 4.9(d)), we note excellent qualitative agreement between the calculated and measured S_{dot} features for $V_{bg} < 0$ (the npn regime), some degree of correspondence for $0 < V_{bg} < 0.3$, and generally worse agreement at higher dot carrier densities. At $B = -4$ T (Fig. 4.9(e)), the agreement is better overall, although for $V_{bg} < -0.2$ there are more discrepancies in the relative peak magnitudes. On the quantitative level, the measured thermopower S_{dot} exceeds the prediction of the Mott formula, particularly at low temperatures. In addition to the edge disorder effects discussed previously, quantum dots with an appreciable charging energy are expected to have a much larger thermopower than would be expected from the Mott formula (by a factor of $k_B T/E_C$ in the "classical" regime $k_B T \gg E_C$)[190]. Although previous thermopower measurements in graphene have generally found better agreement with the Mott relation at higher temperatures[30,184], we actually observe larger deviations from the Mott formula prediction in the qualitative features (Fig. 4.9(f)). In particular, the measured thermopower modulations in the npn regime are much broader and smoother than would be expected from the derivative of the electrical conductance. For a fuller picture of the transport behavior through the dot, we must examine the temperature dependence of the electrical conductance and the thermopower.

Figure 4.10(a) shows G_{diag} with $\nu_{res} = 2$ at $B = -10$ T as a function of V_{bg}, with corresponding adjustments to V_{tg}, and T_{bath} between 1.4 K and 31.4 K. (At higher temperatures, the doped silicon back gate developed a significant leak current to the device when sufficient voltage was applied to effectively dope the contacts.) The $G \approx 2e^2/h$ region retains a nearly constant width and conductance value across the entire temperature range. For the remaining analysis, we consider the longi-

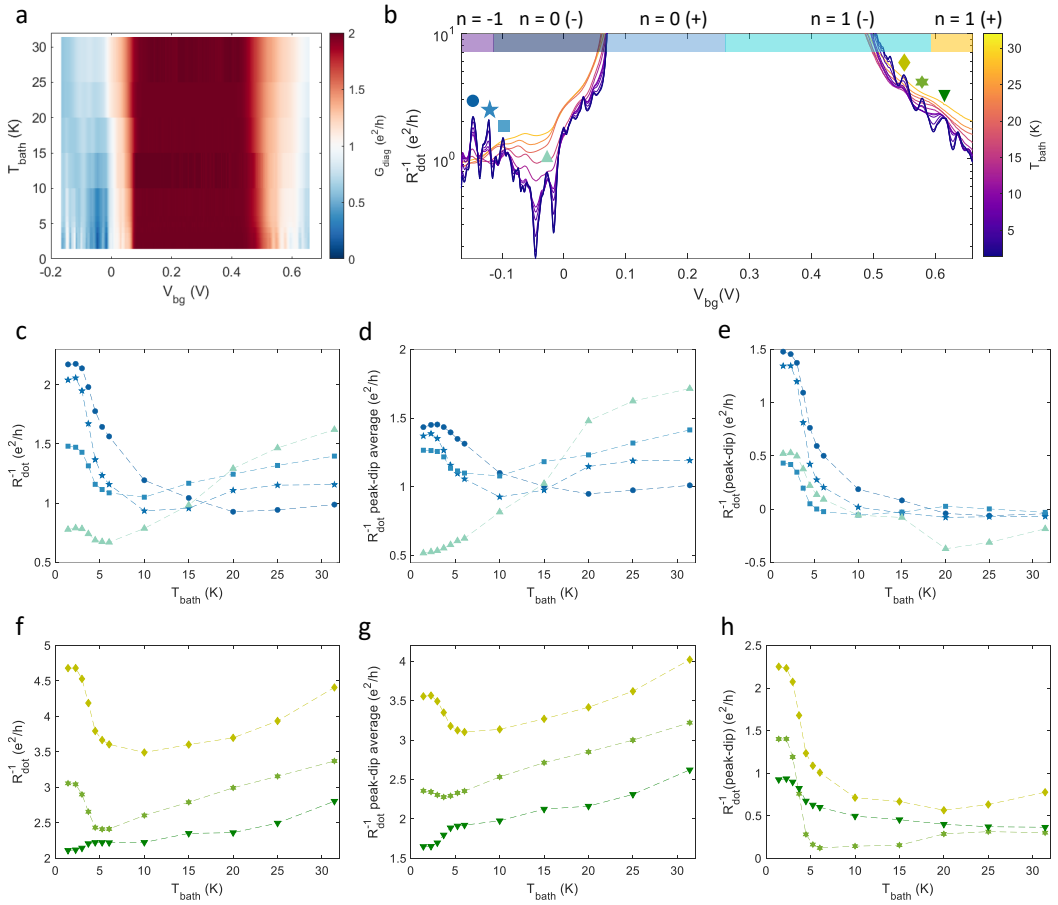

Figure 4.10: (a) G_{diag} at $B = -10$ T and $\nu_{res} = 2$ as a function of ν_{dot} and T_{bath} between 1.4 K and 31.4 K. (b) Line plots of R_{dot}^{-1} versus V_{bg} at various T_{bath}, indicated by the color bar. Gate voltage ranges for various Landau levels in the dot are marked by color-coded rectangles across the top of the plot. Purple: $n = -1$ LL. Dark blue: $n =$ LL (hole side). Light blue: $n = 0$ LL (electron side). Turquoise and yellow: $n = 1$ LL. (c-e) Scatter plots of selected R_{dot}^{-1} peak and dip values (c), average R_{dot}^{-1} between selected peaks and adjacent minima (d), and difference in R_{dot}^{-1} between selected peaks and adjacent minima (e), as a function of T_{bath}, for features in the npn regime ($n = -1$ LL and hole side of $n = 0$ LL) indicated by symbols in (b). Circles: $V_{bg} = -0.147$ V. Pentagrams: $V_{bg} = -0.121$ V. Squares: $V_{bg} = -0.099$ V. Upward triangles: $V_{bg} = -0.027$ V. (f-h): Same plots as (c-e) for features in the nn'n regime ($n = 1$ LL) indicated by symbols in (b). Diamonds: $V_{bg} = 0.548$ V. Hexagrams: $V_{bg} = 0.578$ V. Downward triangles: $V_{bg} = 0.611$ V.

tudinal conductance across the dot, $G_{dot} = 1/R_{xx}^{dot}$ (written as R_{dot}^{-1} to avoid confusion with G_{diag}). This has the same qualitative features as G_{diag} in its temperature and carrier density dependence in the npn and nn'n regimes, and is more analogous to the thermopower measurement geometry than G_{diag}. Focusing on the npn and nn'n regimes (left and right sides of Fig. 4.10(b), respectively), we can track evolution of the R_{dot}^{-1} oscillations previously noted for G_{diag} in Fig. 4.7(e). We should compare similarities and differences between the npn and nn'n regimes; at $|B| = 10$ T, the npn regime contains the hole-doped side of the $n = 0$ LL ($-2 < \nu_{dot} < 0$) as well as the upper part of the $n = -1$ LL, while the nn'n regime ($\nu_{dot} \gg 2$) is in the $n = 1$ LL. Since the initial theory proposal emphasizes the importance of the $n = 0$ LL for the emergence of SYK physics in graphene [142], it is essential to determine whether or not the behavior in that regime differs from other Landau levels.

To better quantify trends in the temperature dependence, we select some representative R_{dot}^{-1} peaks in each doping regime (indicated by symbols above peaks in Fig. 4.10(b)). In the npn regime (Fig. 4.10(c)), R_{dot}^{-1} at each peak location stays at a nearly constant height between 1.4 K and 3 K, decreases until at least 6 K, then eventually starts rising again. R_{dot}^{-1} at the peak position $\nu_{dot} \approx -2$ (circles) decreases for the largest temperature range, up to $20 - 25$ K, while the adjacent peaks at smaller $|\nu_{dot}|$ (pentagrams, squares) have their lowest points at 10 K and the feature in the middle of the hole-doped side of the $n = 0$ LL ($\nu_{dot} \approx -1$, upward triangles) begins rising at even lower T_{bath}. We can see similar behavior in the nn'n regime (Fig. 4.10(f)), although the second transition appears to uniformly occur at $T_{bath} \approx 5$ K. Referring back to the traces of R_{dot}^{-1} as a function of V_{bg}, it becomes evident that simply tracking the value of R_{dot}^{-1} at constant dot filling convolves two separate trends: changes in the local average value with temperature, and the tendency of the peaks and dips in the conductance to grow or shrink relative to the average value. To separate these, we plot temperature dependence of R_{dot}^{-1} averaged between the selected peaks and adjacent dips (Fig. 4.10(d) for npn regime, (h) for nn'n regime) as well as the difference between adjacent peak and dip values (Fig. 4.10(e) for npn regime, (h) for nn'n regime). Now we can see that, in the npn regime,

the peak-dip differences all start at different values but follow essentially similar trends in the temperature dependence, while the average value of R_{dot}^{-1} above 10 K rises faster and starting at lower T_{bath} for smaller $|\nu_{dot}|$. In the nn'n regime, the R_{dot}^{-1} behavior follows similar trends, although the oscillations smooth out more completely by $T_{bath} = 10$ K and R_{dot}^{-1} rises more uniformly after that. The generally increasing local average R_{dot}^{-1} with higher T_{bath} may have its origins in a decrease in the tunneling resistance between the reservoirs and the dot, which is not accounted for in the theoretical predictions for electrical conductance of an SYK dot [143,144]. Overall, the temperature dependence of the electrical conductance at constant dot filling does not qualitatively match the theory for the pure FL-to-SYK transition [144] particularly well, and we note that similar behavior is observed for conductance peaks in the $n = 0$ LL (npn regime) and the $n = \pm 1$ LL (nn'n regime and more negative V_{bg} range in the npn regime).

We repeat the same temperature dependence analysis for the thermopower, shown in Figure 4.11. In both a color plot of S_{dot} as a function of V_{bg} ($\nu_{res} = 2$) and T_{bath} and individual line scans (Fig. 4.11(a,b)), there is a clear transition from rapid, sign-changing oscillations in both the npn and nn'n regimes at $T_{bath} \lesssim 6$ K and broader modulations for $T_{bath} \geq 10$ K that remain negative for the visible part of the $n = -1$ LL and the hole-doped side of the $n = 0$ LL ($\nu_{dot} < 0$), are positive for the electron-doped side of the $n = 0$ LL and into the $n = 1$ LL ($0 < \nu_{dot} < 4$), and become negative again further into the $n = 1$ LL ($\nu_{dot} > 4$). At low temperatures, each peak in R_{dot}^{-1} splits into a peak and a dip roughly centered at the corresponding filling, which we already saw manifested as the good qualitative correspondence between the measured thermopower and the Mott formula (see Fig. 4.9). We track the behavior of the peaks and dips corresponding to the R_{dot}^{-1} peaks marked in Fig. 4.10(b). In the npn regime (Fig. 4.11(c-e)), both the local average and the peak-dip difference increase to peak at $T_{bath} \approx 3$ K, with the peak-dip difference then decreasing to zero and the average settling to a negative value by 10 K. Fig. 4.11(d) also tracks the average value of S_{dot} on both the hole-doped and electron-doped sides of the $n = 0$ LL, with error bars reflecting the magnitude of the

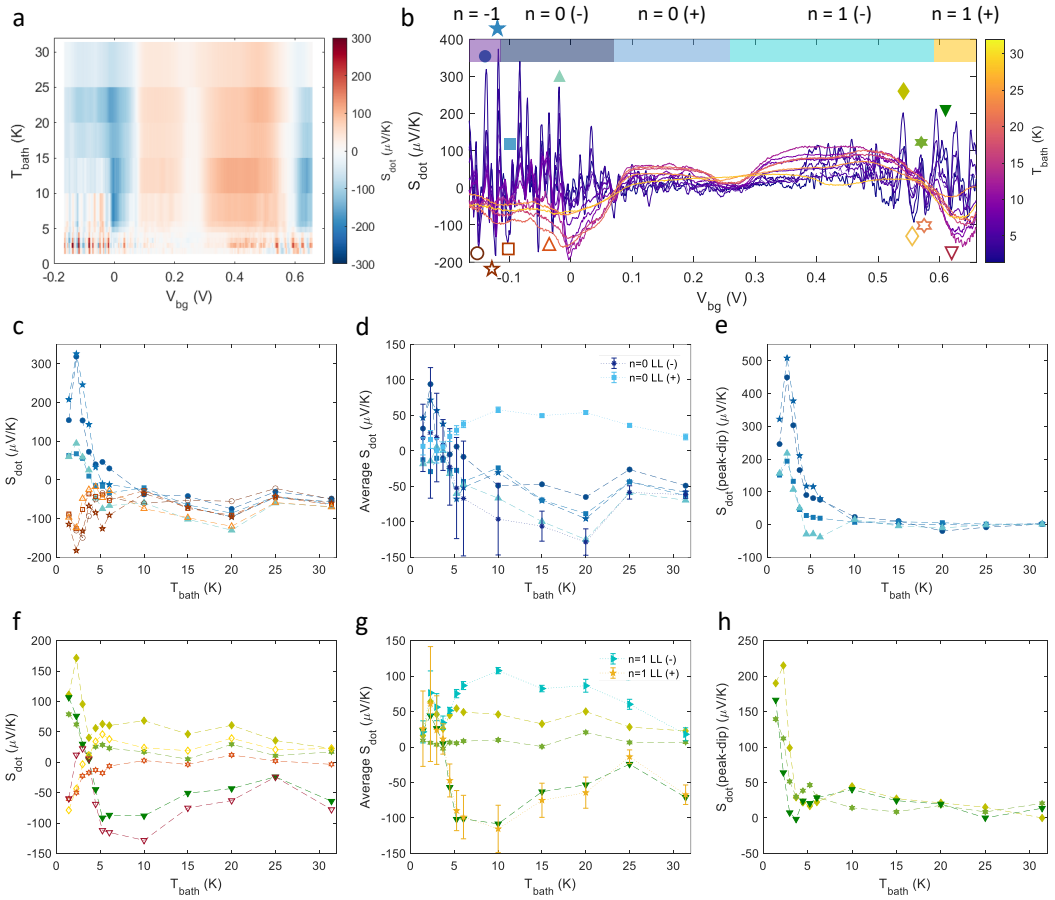

Figure 4.11: (a) S_{dot} at $B = -10$ T and $\nu_{res} = 2$ as a function of V_{bg} and T_{bath} between 1.4 K and 31.4 K. (b) Line plots of S_{dot} versus V_{bg} at various T_{bath}, indicated by the color bar. Gate voltage ranges for various Landau levels in the dot are marked by color-coded rectangles across the top of the plot. Purple: $n = -1$ LL. Dark blue: $n = 0$ LL (hole side). Light blue: $n = 0$ LL (electron side). Turquoise and yellow: $n = 1$ LL. (c-e) Scatter plots of selected S_{dot} peak and dip values (c), average S_{dot} between selected peaks and adjacent dips (d), and difference in S_{dot} between selected peaks and adjacent dips (e), as a function of T_{bath}, for features in the npn regime ($n = -1$ LL and hole side of $n = 0$ LL) indicated by symbols in (b). Features were selected to fall on either side of G_{diag} peaks tracked in Fig. 4.10. Circles: $V_{bg} = -0.138$ V (dip: $V_{bg} = -0.149$ V). Pentagrams: $V_{bg} = -0.117$ V (dip: $V_{bg} = -0.122$ V). Squares: $V_{bg} = -0.094$ V (dip: $V_{bg} = -0.099$ V). Upward triangles: $V_{bg} = -0.025$ V (dip: $V_{bg} = -0.030$ V). In (d), additional symbols show average S_{dot} in the $n = 0$ LL, separated into hole side ($-1.5 < \nu_{dot} < -0.5$, dark blue asterisks) and electron side ($0.5 < \nu_{dot} < 1.5$, light blue squares). Error bars are derived from standard deviation within this range. (f-h): Same plots as (c-e) for features in the nn'n regime (electron side of $n = 0$ LL and $n = 1$ LL) indicated by symbols in (b). Diamonds: $V_{bg} = 0.543$ V (dip: $V_{bg} = 0.559$ V). Hexagrams: $V_{bg} = 0.572$ V (dip: $V_{bg} = 0.581$ V). Downward triangles: $V_{bg} = 0.610$ V (dip: $V_{bg} = 0.619$ V). In (g), additional symbols show average S_{dot} in the $n = 1$ LL, separated into positive ($2.5 < \nu_{dot} < 3.5$, turquoise triangles) and negative ($\nu_{dot} > 4.5$, yellow pentagrams). Error bars are derived from standard deviation within this range.

fluctuations (and therefore becoming smaller at higher temperatures). The LL-averaged values of the thermopower have their minimum amplitude at $T \approx 3.7$ K, separate to essentially constant magnitudes between 10 and 20 K, and move back toward smaller values at higher temperatures. There is some uncertainty in the exact S_{dot} magnitude due to lower signal-to-noise ratio at higher T_{bath} in the quantum Hall thermometry measurements used to determine ΔT (discussed further in Appendix B). It is possible that deviations in S_{dot} and the average value from the constant negative (positive) value predicted for thermopower of a hole-doped (electron-doped) SYK island [144] are due at least in part to experimental uncertainty in this temperacture calibration process. However, differences between features at varying dot carrier densities cannot be explained by ΔT uncertainty; we note that largest (negative) values of the local average S_{dot} occur for $\nu_{dot} \approx -1$ in the higher temperature range, while the peaks in the peak-dip difference at low temperature are highest at larger $|\nu_{dot}|$.

In the nn'n regime (Fig. 4.11(f-h)), the peak-dip averages and peak-dip differences of S_{dot} both spike slightly earlier than in the npn regime, at $T_{bath} = 2.3$ K. The differences drop sharply to zero by 5 K, while the averages converge toward zero until 3.7 K, then diverge to fluctuate around positive values for $\nu_{dot} < 4$ (diamonds) and negative values for $\nu_{dot} > 4$ (downward triangles). The values of S_{dot} in the $n = 1$ LL averaged over a range of filling factors before and after this sign change (turquoise triangles and yellow pentagrams, respectively, in Fig. 4.11(g)) show qualitatively similar behavior to the averages in the $n = 0$ LL, although the decrease in magnitude seems to occur start at lower temperature.

We note several minima and sign changes of S_{dot} in the higher-temperature data, which are particularly evident on the color plot (Fig. 4.11(a)): a sign change at $\nu_{dot} \approx 0$ and at $\nu_{dot} \approx 4$, with an $S_{dot} \approx 0$ minimum for $\nu_{dot} \approx 2$ in the otherwise positive region between them. These begin to emerge at $T_{bath} = 4.5$ K, and the sign changes persist throughout, while the additional minimum begins to weaken for $T_{bath} > 20$ K. The sign change at charge neutrality in the dot and the

minimum at $\nu_{dot} \approx 2$ are reminiscent of thermopower measurements of graphene flakes and Hall bars in the quantum Hall regime, which has peaks in S_{xx} at half-filled LLs with the aforementioned quantized values $(k_B e/h)\ln(2)/\nu$ and minima[43,61]. There is a less-developed local minimum near $\nu_{dot} \approx -2$ that would agree with this picture, but the sign change in the middle of the $n = 1$ LL is different from the previous observations in simpler graphene systems. The thermopower of a Coulomb-blockaded quantum dot exhibits a peak-dip pair centered at each resistance peak[190], which is essentially true of our measured S_{dot} at low temperature only. In general, our thermopower measurements in the $n = 0$ LL are in many ways consistent with a transition from FL to SYK behavior at $T_{bath} \sim 3$ K described in Ref. 144 (see Fig. 4.2(c)), within the uncertainty of our data. However, the lack of $G \sim 1/\sqrt{T}$ behavior and the similarities in both condutance and thermopower measurements between the $n = 0$ and $n = 1$ LLs warrant further consideration.

4.6 Discussion

According to recent theoretical models[142,143], the combination of confinement and edge disorder in the $n = 0$ LL of a small graphene flake has been predicted to approximate the SYK Hamiltonian, which has some distinctive transport signatures[144]. We attempted to test this prediction by measuring electrical conductance and thermopower in an etched graphene quantum dot coupled to the quantum Hall edge states in a larger device. Using a combination of graphite gates, we were able to tune the carrier densities of the dot and reservoirs into the $n = 0$ and $n = 1$ LLs in the dot, while keeping the reservoirs at constant filling factor $\nu_{res} = 2$. Notably, both our conductance and thermopower measurements showed qualitatively similar behavior in most respects between the $n = 0$ LL, where we expected SYK physics to potentially appear, and the $n = 1$ LL, which we expected not to host SYK physics because it lacks the special protection from disorder broadening of the lowest LL. However, this argument assumes that our engineered disorder preserves chiral symmetry, which

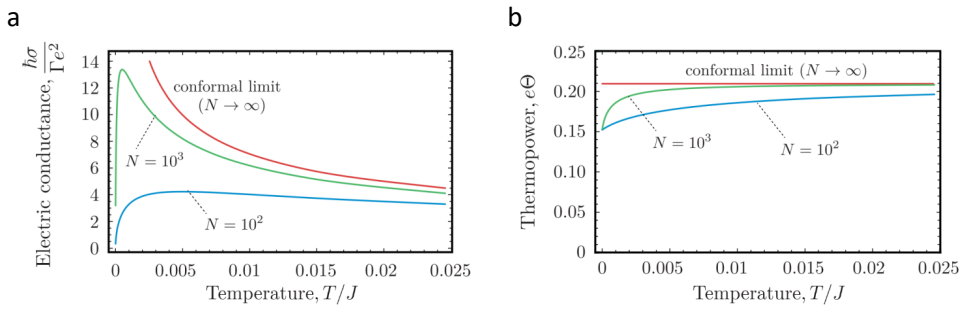

Figure 4.12: Crossovers in transport from the SYK regime at $T > J/N$ to finite-N regime at $T < J/N$: (a) electrical conductance and (b) thermopower. It is assumed that $T, J/N \gg E_{coh}, E_C$. The calculation uses $J = 1, \mathcal{E} = 0.05$. Adapted from Ref. 144.

Chen *et al.* argue is best achieved by an extremely clean "bulk" of the dot with a random edge [142]. In a real device, there are many possible sources of chiral symmetry-breaking disorder, including random on-site potentials induced by fabrication processes [191]. The absence of fractional quantum Hall states even in the reservoirs of our devices at low temperature (350 mK) and high magnetic fields (10 T) and the fact that the $n = 0$ LL does not appear to be more sharply defined than other LLs suggest that a degree of non-engineered, chiral symmetry-breaking disorder remains. If chiral symmetry is not preserved, the $n = 0$ LL is not necessarily much more favorable for the emergence of SYK physics than other LLs. As such, the parallels between the transport signatures in the $n = 0$ and $n = 1$ LLs should not be interpreted as counterevidence for the possibility of SYK behavior in the dot.

We have already noted that both the electrical conductance and the thermopower of the dot undergo transitions in their temperature-dependent behavior from large, rapid oscillations at $T_{bath} \lesssim 4 - 5$ K to smaller and broader modulations at $T_{bath} \gtrsim 5$ K. This is well-aligned with what we would expect for a crossover from coherent transport (for example, universal conductance fluctuations [1,192]) to incoherent SYK behavior, the $T < E_{coh}$ to $T > E_{coh}$ discussed in Section 4.2. However, the increasing electrical conductance in the putative $T > E_{coh}$ regime is clearly different from

the prediction of $G \sim 1/\sqrt{T}$ shown in Fig. 4.2(b). A likely source of this discrepancy is finite-N corrections to the SYK physics, which we had initially assumed were insignificant compared to E_{coh}. For our 140 nm by 90 nm dot at $B = 10$ T, the approximate number of SYK modes $N_0 = BA/\Phi_0$ is only 33, which is far from the conformal limit ($N \to \infty$). With finite-N effects, the electrical conductance changes from uniformly decreasing with increasing temperature as $G \sim 1/\sqrt{T}$ to include regimes where the conductance increases with temperature (Fig. 4.12(a)), which is more consistent with our experimental observations. In contrast, decreasing N causes the thermopower to take longer as the temperature increases to saturate at a constant value (Fig. 4.12(b)), but it qualitatively remains very close to the expectation with $E_{coh} \gg J/N$ (Fig. 4.2(c)). Further theoretical study of the effects of competing lower energy scales, and finite-N corrections in particular, could improve our understanding of the crossover from SYK to coherent physics and whether our experiments provide robust evidence of such a transition occurring in an etched graphene flake.

In addition to finite-N corrections, we may need to consider the charging energy as a competing energy scale. We specifically designed our devices with relatively thin ($\sim$ 5 nm) hBN between the graphene and the graphite gate tuning the carrier density in the dot. Based on the thickness of the hBN, its dielectric constant $\varepsilon_r \approx 4$ [188], and the dot size, we would roughly estimate the charging energy $E_C = e^2/C_{dot}$ to be on the order of 1 K. However, from the spacing of quantum Hall-related features in the dot and reservoir transport (Fig. 4.8), the capacitance we extract gives the charging energy $E_C \approx 2.8$ meV, or 32 K. This corresponds to an unexpectedly low capacitance, but it is consistent with the capacitance between the graphite gates and the reservoirs, based on quantum Hall measurements of the reservoirs. It is possible that the graphite flakes used for the gates were too thin to behave as a pure metal; a lower density of states in the graphite gates could cause a substantial quantum capacitance contribution [193].

Another practical difficulty was the inability to directly measure the temperature gradient across the dot, which ties into more general device design considerations. Continuing this line of mea-

surements, we can suggest a few changes that may provide additional flexibility. It may be useful to reconfigure the contacts to the reservoirs so that it is possible to measure ΔT due to the heater at more locations, providing a better map of the temperature gradient and thus a better estimate of the gradient across the dot. We can also imagine changing the geometry so that the dot density is tuned by a local top gate, contacted using an air bridge; this may be more convenient for precisely adjusting the carrier density in the dot, and the additional nearby metal could help reduce E_C. Defining the dot using local anodic oxidation [194] on a graphene flake prior to encapsulation would reduce the number of lithography steps, and may generate the appropriate randomness on the edge while reducing undesirable contamination of the rest of the device.

Experimental challenges notwithstanding, our measurements already represent a significant step toward realization of the SYK model in a mesoscopic system. We see promising signatures in our measurements of a transition from rapid fluctuations (which, in the case of the thermopower, are highly temperature-dependent) to more broadly-varying conductance and thermopower (which becomes much less temperature-dependent) in the temperature range predicted for our quantum dot size and applied magnetic field [161]. Further experimental and theoretical analysis of this transition regime, including temperature-dependent conductance and thermopower fluctuations, may differentiate disorder-induced phase fluctuations in the finite-N FL regime (universal conductance fluctuations [1,192]) from the strongly-correlated, incoherent SYK regime.

By using your intelligence, you can sometimes make your problems twice as complicated.

Ashleigh Brilliant

5

Outlook and future directions

Unusual quantum effects can emerge in mesoscopic systems as a result of the interplay of dimensional confinement and Coulomb interactions. In this thesis, we have explored three examples of novel phenomena arising in mixed-dimensional devices, probed by electronic and thermoelectric transport measurements. In Chapter 2, we showed that the 1D-2D nature of a carbon nanotube-graphene device appears in the Coulomb drag between these two conductors. In Chapter 3, our electrical and thermal conductance measurements of single carbon nanotubes, using graphene as

heater, thermometer, and electrode, were the basis for developing a new model for plasmon-enabled energy transport through barriers to charge flow. In Chapter 4, we discussed electronic and thermoelectric transport measurements of an etched graphene quantum dot in the quantum Hall regime, motivated by the potential to realize the SYK model. We will close with a few remarks on future directions.

The carbon nanotube-graphene system remains an option for studying graphene hydrodynamics probed via Coulomb drag, but there are plenty of other possibilities for this type of device. Carbon nanotubes have great utility as charge sensors [14] and local gates [95,195]. As the ability to cut or otherwise manipulate materials using atomic force microscopes tips has continued to advance, a precisely placed metallic carbon nanotube could be bent into a shaped gate to constrain the flow of chiral edge states or hydrodynamic electrons, or a have small section cut between two contacted ends to form an extremely thin quantum point contact. As a flexible mesoscopic conductor with effectively 1D electronic confinement, carbon nanotubes have great potential to be creatively integrated into otherwise 2D or 3D devices.

Graphene-based Johnson noise thermometry has proved to be a useful technique for thermal conductance measurements of a variety of quantum materials. For further experiments incorporating carbon nanotubes, fully hBN-encapsulated or suspended nanotube bridges could move the study of 1D thermal transport into a less disorder-dominated regime. This would enable further exploration of Luttinger liquid thermal transport, as well as the thermal side of other phenomena electronically observed in carbon nanotubes, such as the Kondo effect [196], which has appeared in nanotube quantum dots.

As for the possible implementation of the SYK Hamiltonian in graphene, we have already mentioned several possible modifications to the experimental geometry and fabrication process that could improve future devices. Taking a wider view, we note that the geometry of the device, two graphene reservoirs connected by the dot, is essentially the same as the graphene-based noise ther-

mometry devices described in Chapter 3, though there are many differences in the details. It would be intriguing to perform thermal conductance measurements of etched graphene quantum dots as a further test of the theory. Capacitance measurements of the evolution with temperature and carrier density of the dot chemical potential μ and $d\mu/dn$, which have recently been performed on monolayer graphene devices [197], could provide a complementary approach to studying SYK dynamics in this system. Another route to SYK physics in graphene may be magic angle twisted bilayer graphene [10] (or one of its multi-layered relatives), which host flat bands even with no applied magnetic field and has already been shown to host a phase with near-Planckian dissipation [152]. For the experiments we presented in this thesis, we hope continued dialogue with the theory community will shed additional light on the unusual behavior we observed.

This is an exciting time to study the physics of low-dimensional (including mixed-dimensional) devices, particularly incorporating van der Waals materials. The field is now mature enough that many of the earlier hurdles of material quality and fabrication techniques have been cleared. While improvements in these areas continue to be made, graphene and its immediate relatives have come to rival or surpass more conventional 2DEGs as a platform for quantum Hall experiments. At the same time, an increasing array of new materials and measurement techniques are creating new possibilities for mesoscopic transport experiments. We hope some of the work presented here might be a springboard for innovative studies of low-dimensional phenomena.

A

Supporting data

This appendix provides additional data that enhances the discussion in Chapter 2.

A.1 Additional Onsager data

We present here additional data comparing the drag response using the two different circuit configurations: driving current in the SWNT and measuring voltage across two probes on graphene, and driving current in the graphene and measuring voltage across the SWNT.

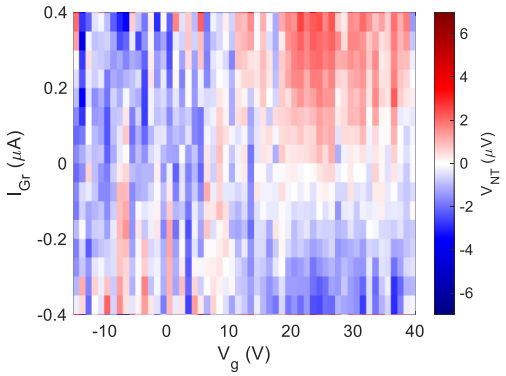

Figure A.1: Drag voltage at $T = 300$ K as a function of drive current and gate voltage, with graphene as the drive layer and SWNT as the drag layer. Current is applied at the closest pair of voltage probes ($x = 800$ nm from the SWNT). Data has been slightly smoothed in the x-direction to reduce noise.

Figure A.1 shows a color plot of drag voltage versus drive current and gate voltage at $T = 300$ K, using the graphene as the drive layer and SWNT as the drag layer. We have applied a narrow (± 3 V range) moving average filter in the x-direction (gate voltage axis), essentially binning the data from adjacent gate voltages together, to reduce noise and make overall trends in the data more apparent. The same general behavior is apparent in this reciprocal configuration as shown in the Chapter 2 for SWNT-drive, graphene-drag measurements (Figure 2.4(e)), although the higher degree of noise in measurements using the SWNT as the drag layer complicates a straightforward comparison based on the color plots alone.

Additional examples of drag voltage versus drive current data for reciprocal drag circuit configurations at individual gate voltages are shown in Figure A.2. Our moving average filter is restricted to an even smaller range (± 1 V) for better quantitative comparison. The range of I_{drive} is restricted to avoid nonlinearites due to high bias, although some nonlinearity in the SWNT-drive data (orange, filled circles) at gate voltages nearer the graphene CNP (e.g. Fig. A.2(c-e)). Although there is more noise in the measurements for which the SWNT was the drag layer (blue, open circles), the general degree to which the two data sets coincide and the overall linearity of both measurements provide

strong evidence that Onsager reciprocity is respected in this regime.

The higher level of noise in the measured drag voltage when the SWNT is the drag layer, which is consistently observed across all gate voltages and temperature, merits some discussion. There are a few potential reasons for increased voltage fluctuations when the SWNT is the drag layer. First of all, the drag resistance is on the order of a few Ohms, while the channel resistance of graphene is less than $\sim$ 1 kΩ, and the resistance of the SWNT is larger than 1 MΩ. Such a large disparity between the SWNT resistance and the drag resistance makes it challenging to detect small resistance variations when we use the SWNT as drag layer. The higher resistance of the SWNT means that small current fluctuations result in larger voltage noise than would be observed if another graphene sheet were used as the drive layer.

An additional contributing factor may be random reconfiguration of mobile charges on the SiO_2 substrate. In our device geometry, the graphene channel is encapsulated, but the SWNT is in direct contact with the SiO_2. Thus, stochastic charge fluctuations in the charge traps on the substrate can induce voltage fluctuations in the SWNT when it is being used as drag layer to probe potential. For SWNT drive, we apply a relatively large bias voltage to obtain the same amount of drive current, thus usually fluctuations in the charge environment would not affect the driving current. The graphene drag layer is much less disordered and thus less susceptible to charge fluctuations on the SiO_2.

Finally, the increased noise level in the graphene drive-nanotube drag configuration may be a result of the high SWNT resistance relative to the amplifier impedance. The input impedance of the voltage amplifier we use is 100 MΩ (SR560) while the load resistance of nanotube is $\sim$2 MΩ. In order to avoid spurious capacitive coupling, we measure the DC drag at slow speed, corresponding to 300 ms of averaging time and $\sim$ 1 second per data point acquisition. In this regime of low frequency measurement with large source resistance, the noise figure (NF) of our preamp is $\sim$ 0.5 dB (https://www.thinksrs.com/products/sr560.htm), suggesting that the noise is completely domi-

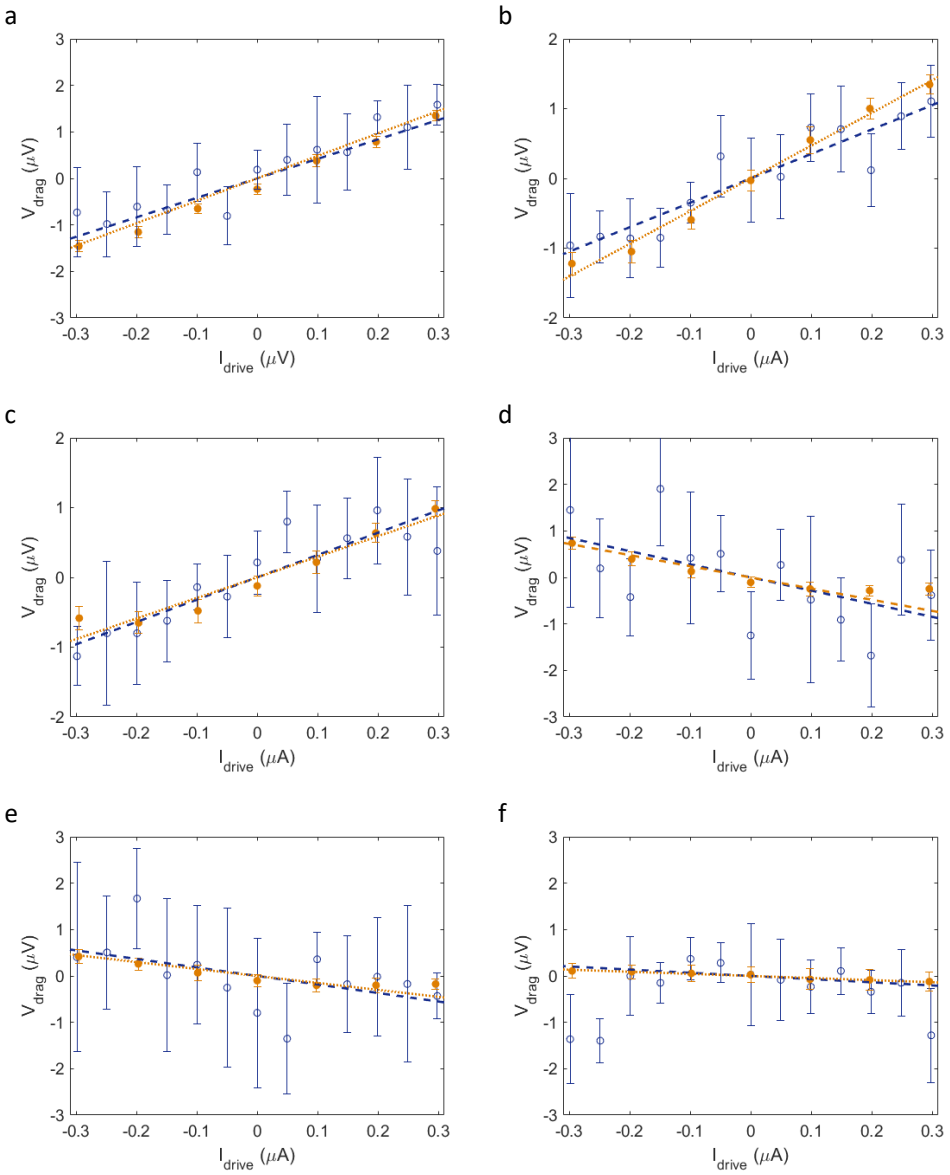

Figure A.2: Drag voltage versus drive current at various gate voltages for reciprocal layer configurations: driving current in the SWNT while measuring graphene voltage (orange, filled symbols) and driving current in the graphene while measuring voltage across the SWNT (blue, open symbols) at $T = 300$ K. V_g value stated is the center of the moving average filter. (a) $V_g = 23$ V. (b) $V_g = 20$ V. (c) $V_g = 16$ V. (d) $V_g = -5$ V. (e) $V_g = -11$ V. (f) $V_g = -18$ V.

nated by Johnson noise across the source resistance. The effective rms noise is $\sim 0.5\,\mu$V, comparable to the fluctuation of the data we observed in the graphene drive-nanotube drag measurement. Note that for the nanotube drive-graphene drag measurement, the source resistance drops to $\sim 1\,\mathrm{k}\Omega$, where the fluctuation in the measured signal is dominated by amplifier noise (NF $\sim$ 20). We estimate that the rms noise for this measurement is $\sim$ 20 nV due to the reduced source resistance despite the increased amplifier noise.

A.2 Individual layer transport and drag resistance in different measurements

The data presented in the main body of this thesis were primarily gathered from two separate thermal cycles of the same device (D1), with the first set of measurements (D1-A) occurring shortly after the completion of nanofabrication, and the second set of measurements (D1-B) starting approximately 9 months later. In Chapter 2, the data in Fig. 2.4, Fig. 2.8(a-c), and Fig. 2.15 are from D1-A, and the data in Fig. 2.8(d-e), Fig. 2.9 and Fig. 2.10 are from D1-B. Comparing similar measurements for the two different data sets (for example the drag resistance versus back gate voltage in Fig. 2.4(f) for D1-A and Fig. 2.9(d) for D1-B), it is apparent that they qualitatively follow the same behavior, but with some quantitative discrepancies. In particular, the back gate voltage range with an appreciable drag signal is much larger for D1-A ($V_g \sim 20$ V) than for D1-B ($V_g \sim 3$ V). This can be attributed to a comparable change in the disorder in the graphene, observed as a change in the CNP position and peak width. Figure A.3 shows a direct comparison of the SWNT conductance, graphene resistance, and drag resistance as a function of gate voltage for D1-A (Fig. A.3(a-c)) and D1-B (Fig. A.3(d-f)). In both data sets, the drag signal width directly corresponds to the width of the graphene CNP peak. Since all the preceding discussion about possible physical mechanisms has relied on the interplay of various regimes (including a disorder-dominated regime) rather

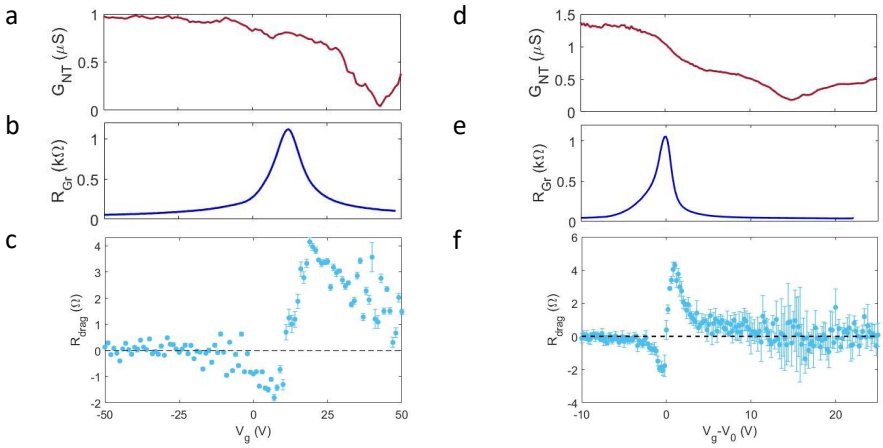

Figure A.3: Individual layer transport and drag resistance as a function of back gate voltage for measurement D1-A. (a) SWNT conductance at $T = 200$ K. (b) Graphene resistance at $T = 100$ K. (c) Drag resistance at $T = 200$ K. (d-e) Individual layer transport and drag resistance as a function of adjusted back gate voltage for the same device after thermal cycling and 9 months of storage (measurement D1-B). The voltage value at the graphene charge neutrality point has been subtracted. (d) SWNT conductance at $T = 200$ K. (e) Graphene resistance at $T = 200$ K. (f) Drag resistance at $T = 200$ K.

than specific numerical predictions (e.g. that the peaks occur at a specific Fermi wavevector in either graphene or SWNT), our arguments should apply equally well in both data sets.

As an additional comparison, Figures A.4 and A.5 show drag resistance data from several other devices. There are a few key differences in the geometry of the various devices. For device pair D2, the graphene was etched into 2 bar segments of differing widths (Fig. A.4(a)). D2-1 is 1.9 μm wide, while D2-2 is 600 nm wide. D1 and D3 have a single bar each (Fig. A.5(a)); D1 is 1 μm wide by 7 μm long, while D3 is 1.2 μm wide by 9.7 μm long. The hBN separating the SWNT from the graphene is significantly thicker for D2 (5 nm versus 2 nm for D1 and 3 nm for D3). Finally, the metal electrodes in D2 contact narrow, protruding sections of graphene ("noninvasive" contacts), while in D1 and D3 they directly contact the bar ("invasive" contacts). We also note that the SWNTs are all metallic, but the chiralities and corresponding diameters are different for each device. The SWNT

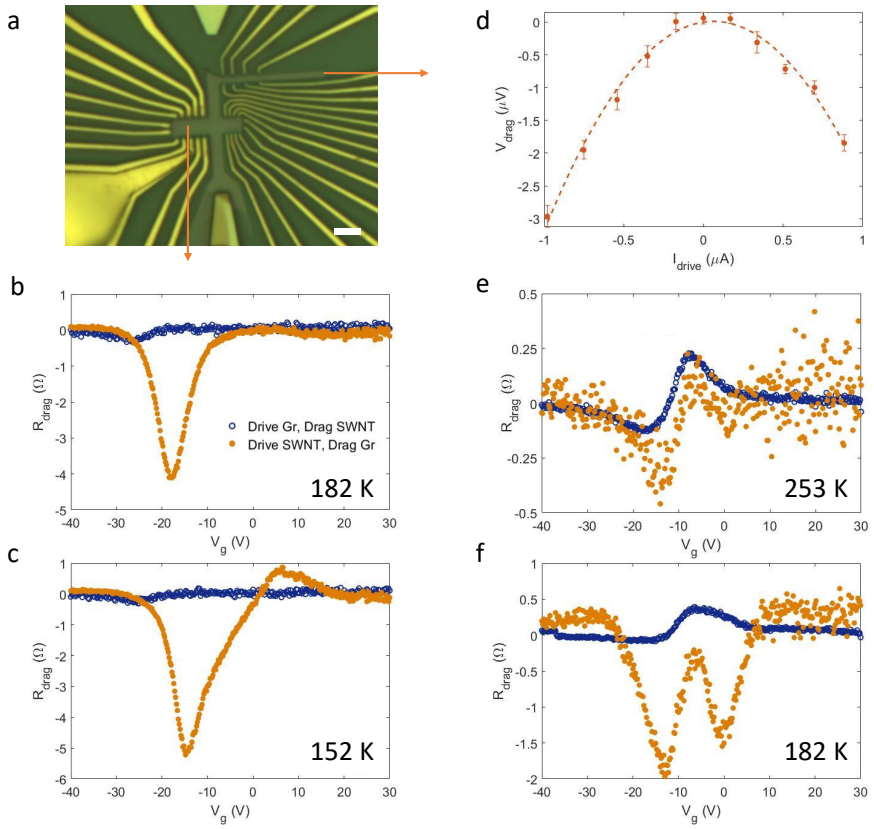

Figure A.4: a) Optical microscope image of device D2. D2-1 refers to the lower, wider section and D2-2 is the upper, narrower section. Scale bar is 4 μm. (b-c) D2-1 drag resistance versus back gate voltage using graphene (blue) or CNT (orange) as the drive layer, at $T = 182$ K (b) and 152 K (c). (d) D2-2 drag voltage in graphene versus drive current in SWNT at $T = 200$ K. (e-f) D2-2 drag resistance versus back gate voltage using graphene (blue) or SWNT (orange) as the drive layer, at $T = 253$ K (e) and 182 K (f). The CNT charge neutrality point in all measurements is at ~ 40 V.

incorporated into D1 has chiral indices $(16, 13)$ and diameter 1.97 nm, the SWNT in D2 has chiral indices $(21, 5)$ and diameter 2.26 nm, and the SWNT in D3 has chiral indices $(21, 15)$ and diameter 2.45 nm.

Measurements of the drag resistance as a function of the gate voltage for D2-1 and D2-2 show consistently smaller signal than D1, which is reasonable given the larger interlayer separation. The exception is when graphene is used as the drive layer, in which case D2-1 shows a comparatively large signal (Fig. A.4(b-c)). Drive/drag layer reciprocity is not observed in the wider bar D2-1, and

while it is respected to a degree in the narrower bar D2-2 (Fig. A.4(e-f)), it breaks down at a higher temperature than in device D1 ($T \sim 200$ K in D2-2, compared to $T \sim 140$ K in D1). These measurements were carried out using a small drive current (200 nA) in an attempt to remain in the linear response regime, and the reported R_{drag} in Figure A.4(b-c),(e-f) is from a linear fit of the drag voltage versus drive current in this small range. Subsequent measurements with larger drive current (Fig. A.4(d)) show a mostly quadratic drag current-voltage relationship. It is therefore likely that the breakdown of layer reciprocity is due to an earlier and stronger onset of nonlinear transport effects (discussed in Section 2.5), and even measurements with a small drive current may have a substantial nonlinear transport contribution. Furthermore, we note that narrow, noninvasive contacts have been predicted not to thermalize efficiently with the electron system in graphene-graphene drag devices near charge neutrality, leading to a breakdown of layer reciprocity even in the linear response regime[76]. This detail of the device geometry may also contribute to the behavior seen in the D2 devices. Since the width of the narrower device D2-2 is comparable to the width of the noninvasive graphene contacts, the bar and contact can thermalize more effectively, which allows some degree of layer reciprocity to be preserved.

The geometry of device D3 is similar to D1, and it displays layer reciprocity at comparable temperatures (Fig. A.5(b)). The drag resistance qualitatively resembles D1, although with a smaller magnitude. This may be attributed to the increased layer separation in device D3. The graphene quality is similar to D1 (Fig. A.5(c) versus Fig. 2.4(d)), but the SWNT has substantially higher resistance and appears quite disordered (Fig. A.5(d)). The drag signal on the positive side of graphene CNP lacks the distinctive peak of the D1 data, likely because SWNT carrier density and current were lower than the corresponding part of the signal in D1. The high-resistance SWNT, as well as additional inhomogeneity appearing during and after thermal cycles, prevented an extensive characterization of device D3. Nonetheless, the initial data we were able to gather support the explanation of the drag behavior in Chapter 2.

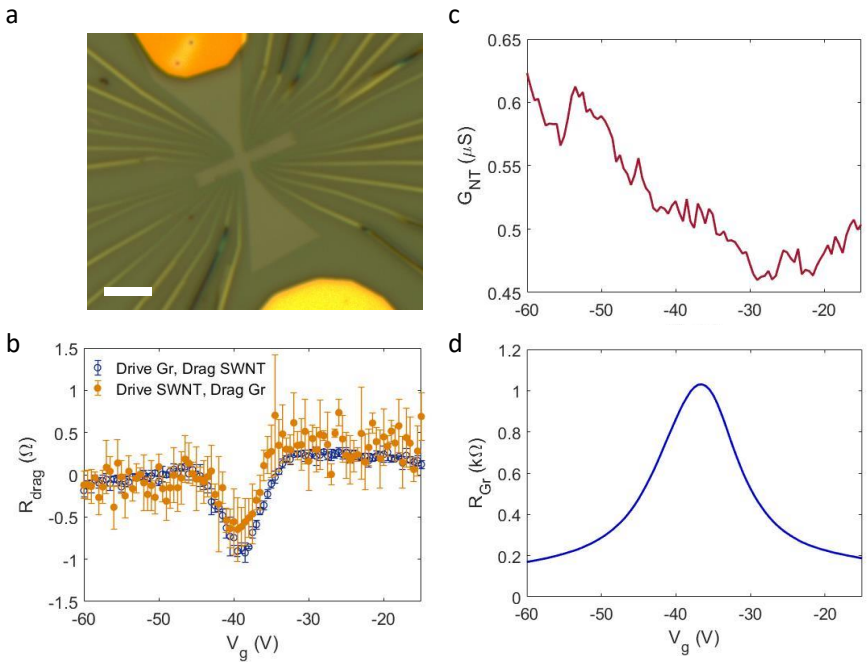

Figure A.5: a) Optical microscope image of device D3. Scale bar is 5 μm. (b) D3 drag resistance versus gate voltage using graphene (blue) or SWNT (orange) as the drive layer, at $T = 200$ K. (c) SWNT conductance versus gate voltage at $T = 200$ K. (d) Graphene conductance versus gate voltage at $T = 200$ K.

B

Thermopower measurement technique

In this appendix, we describe the measurement technique for the thermopower experiments described in Chapter 4. Unlike a measurement of resistance $R = V/I$, in which either voltage or current is directly applied by the experimenter and the other quantity is measured, determining the thermopower $S = -\Delta V_{th}/\Delta T$ of a mesoscopic device requires careful measurement to extract both quantities. In our devices, running a current through a thin wire nearby causes Joule heating in the wire, which generates a temperature gradient across the sample. We must then measure both the

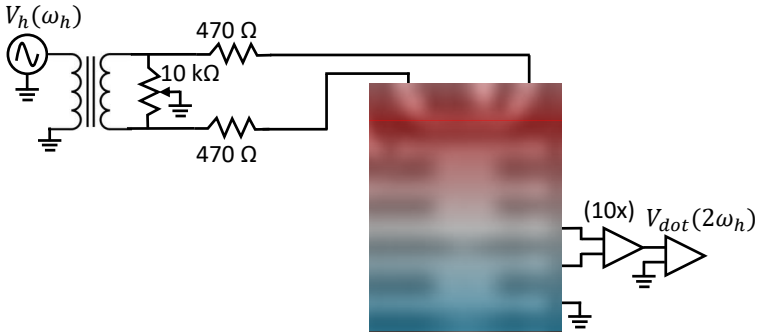

Figure B.1: Circuit schematic for dot thermopower measurements.

thermally-induced voltage ΔV_{th} and the temperature gradient ΔT. In this case, we used the AC (2ω) technique to detect ΔV_{th} and measurements of changes in the quantum Hall signal as a function of T_{bath} and heater excitation to estimate the temperature gradient.

B.1 AC THERMOPOWER MEASUREMENTS

The underlying principle of the AC method for thermopower measurements is that applying an AC excitation to the heater generates a temperature gradient modulated at twice the excitation frequency, and this frequency dependence translates to ΔV_{th} as well. This technique was used in Refs. 43 and 185, although they used a different method to estimate the temperature gradient.

Figure B.1 shows the circuit used for AC thermopower measurements across the dot. To avoid inadvertently creating a voltage offset between the heater and graphene channel, we symmetrically biased the heater using lock-in amplifier connected to a $1:1$ transformer, with a tunable 10 kΩ resistor between the output arms to tune the common mode potential. The output arms are connected to the ends of the heater through matched 470 Ω resistors, to convert the voltage bias from the excitation lock-in to a current bias on the heater. The total two-terminal resistance of the heater side of the assembly, including the external resistors, line resistances, and heater resistance, was $R_h = 1.453$

kΩ, used to calculate I_h when needed. R_h was not found to change with temperature within the experimental range. The true amplitude V' of the voltage excitation from the lock-in sine output is related to the root-mean-squared (rms) value on the lock-in display V_h by

$$V' = \sqrt{2} V_h \cos(\omega_h t), \tag{B.1}$$

where ω_h is the frequency of the AC excitation on the heater.

The temperature gradient ΔT resulting from the heater excitation is proportional to the Joule power,

$$\Delta T = \zeta \frac{V'^2}{R_h} = 2\frac{\zeta}{R_h} V_h^2 \cos^2(\omega_h t) = \frac{\zeta}{R_h} V_h^2 \cos(2\omega_h t) + \frac{\zeta}{R_h} V_h^2, \tag{B.2}$$

where ζ is a proportionality constant determined by the thermometry calibration measurements described in the next section. From the equation above, we see that applying an AC voltage to the heater at frequency ω_h generates a temperature gradient with an AC component at $2\omega_h$ with amplitude $\Delta T_{AC} = \frac{\zeta}{R_h} V_h^2$.

Once we have determined the corresponding ΔT, we can find the thermopower from voltage measurements at the second harmonic of the heater frequency:

$$S_{AC} = \frac{\sqrt{2}\Delta V_{th}(2\omega_h)}{\Delta T}, \tag{B.3}$$

where the factor of $\sqrt{2}$ again comes from the fact that the lock-in amplifier detects the rms value of the voltage. The second harmonic signal is $\pi/2$ out of phase with the original excitation, and so should be measured on the Y channel of the lock-in amplifier. For our experiments, we typically also used a low-noise voltage preamplifier set to a gain of 10 in order to improve the signal-to-noise ratio for measuring small thermal voltages, but we repeatedly confirmed that repeating the measurement without this preamplifier did not substantially affect the thermopower reading.

B.2 Temperature gradient estimation with quantum Hall thermometry

We now describe the method for determining the temperature gradient, using the calibration circuit shown in Fig. B.2(a). The essential idea is to measure the longitudinal Hall resistance across two voltage probes that are at the same distance from the heater, and should therefore be at the same temperature. As the temperature increases, either globally due to a change in T_{bath} or more locally due to an excitation in the heater generating a temperature gradient, the resistance values will change. In particular, the R_{xx} minima at integer quantum Hall fillings should increase as

$$R_{xx}^{min} \propto e^{-\Delta_a/k_B T}, \tag{B.4}$$

where Δ_a is the activation gap[198]. For small changes in temperature δT, this can be approximated by $\Delta R_{xx} \propto \delta T$. We can therefore monitor changes in R_{xx} as a function of either V_h (at constant T_{bath}) or T_{bath} (with no applied V_h). Since we have established that the temperature gradient due to the heater excitation is proportional to V_h^2, we will measure either $\Delta R_{xx}(\delta T_{bath}) = A\delta T_{bath}$ or $\Delta R_{xx}(V_h) = BV_h^2$. Note that the coefficient A contains the factor ζ/R_h defined in the previous section. By measuring simultaneously at several pairs of voltage probes, we can map the spatial temperature variations due to the heater; in this case, we use the pairs of contacts in the upper and middle reservoirs closest to the dot (R_{xx}^U and R_{xx}^M, respectively, in Fig. B.2(a)). It is important to note that this is a resistance measurement, not a thermopower measurement; the lock-in excitation frequency for the R_{xx} measurement (ω_e) must be chosen not to overlap with the heater frequency ω_h or its second harmonic. We used $\omega_h = 23.333$ Hz and $\omega_e = 17.777$ Hz.

Some results of R_{xx} measurements across the upper reservoir contacts at $B = 4$ T as a function of V_{bg} are shown in Fig. B.2(b-c) for varying V_h (b) and T_{bath} (c), with an initial temperature of $T_{bath} = 3$ K. We chose to perform the calibration at $B = 4$ T due to the easy visibility of multiple

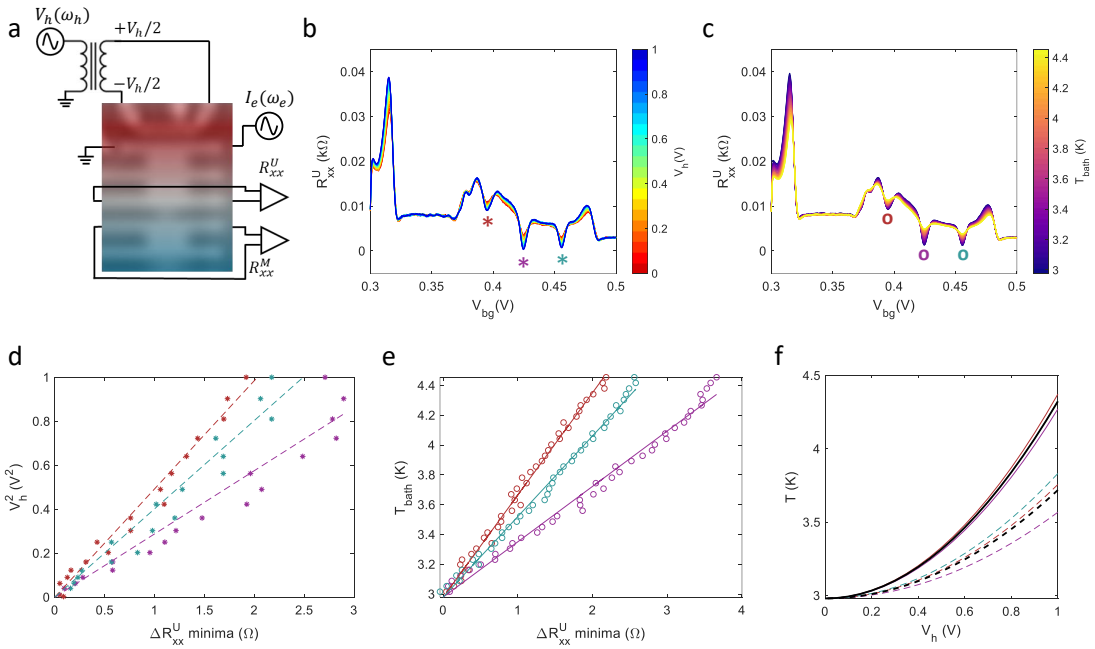

Figure B.2: (a) Simplified circuit schematic for temperature gradient estimation: heater is symmetrically biased through a $1:1$ transformer, generating a temperature gradient across the sample proportional to V_h^2. Temperature increase across dot is estimated by measurement of changes in R_{xx} on either side of the dot, using voltage probes at a constant distance from the heater, as a function of either V_h or T_{bath} (with no applied V_h). R_{xx} is measured at frequency ω_e (b) Upper reservoir R_{xx} (R^U_{xx}) as a function of V_{bg} at various V_h, with $B = 4$ T, $T_{bath} = 3$ K and $V_{tg} = 0$ V. $\nu_{res} = 7, 8, 9$ minima indicated by red, purple and teal stars, respectively. (c) Same measurement as (b), but $V_h = 0$ V and T_{bath} is varied from 3 K to 4.47 K. $\nu_{res} = 7, 8, 9$ minima indicated by circles. (d) V_h^2 versus change in R^U_{xx} at $\nu_{res} = 7, 8, 9$, with lines of best fit used for calibration. (e) T_{bath} versus change in R^U_{xx} at $\nu_{res} = 7, 8, 9$, with lines of best fit. (f) Temperature increase from T_{bath} in upper (solid lines) and middle (dashed lines) reservoirs as a function of V_h. Red, purple, and teal lines indicate individual estimates for $\nu_{res} = 7, 8, 9$ minima, while bold black lines indicate the average of the estimates.

R_{xx} minima within a relatively small range of V_{bg}. We tracked the change in R_{xx} at $\nu_{res} = 7,\ 8$, and 9 in each reservoir as a function of V_h^2 and T_{bath}, shown in Fig. B.2(d) and (e), respectively for the upper reservoir. Similar results were obtained for the middle reservoir, although the change in R_{xx}^M as a function of V_h^2 was smaller due to the larger distance from the heater. By fitting the data, we could extract the calibration coefficients A and B for each T_{bath}, and thus find the conversion from applied V_h to resulting temperature: $T = ABV_h^2$. The results for $T_{bath} = 3$ K are shown in Fig. B.2(f). We note that each R_{xx} minimum gives a slightly different value for the calibration coefficients (indicated by corresponding colors in the figure), so the average value is used for final estimate of ΔT, with any obvious outliers excluded.

At higher temperatures ($T_{bath} > 6$ K), the R_{xx} minima corresponding to symmetry-broken integer states had become nearly indistinguishable, so we looked for other features in the R_{xx} data that varied linearly with respect to small changes in T_{bath} and used them for the calibration. While the use of other features rests on a slightly less robust theoretical foundation than R_{xx} minima, we note this method has yielded reliable temperature estimates in other graphene quantum Hall systems [199].

C

Rayleigh scattering spectroscopy, imaging and transfer of carbon nanotubes

One of the most extraordinary features of the carbon nanotube (CNT) is its extreme aspect ratio; a single-walled CNT can be centimeters long but only a nanometer in diameter [15]. With typical diameters far less than the diffraction limit of visible light, CNTs cannot be observed with conventional optical microscopy, and thus alternative sensing methods are necessary to incorporate individual

CNTs into mesoscopic devices. Furthermore, typical CVD growth methods produce CNTs with a range of diameters and therefore electronic properties. A random distribution of diameters will yield a batch of grown CNTs that is 1/3 metallic and 2/3 semiconducting, depending on whether equivalent or inequivalent atoms in the graphene lattice are on top of each other when it is "rolled up" to form the CNT. It is therefore useful to have a technique for characterizing the chiral indices of carbon nanotubes. Finally, once a CNT has been located and characterized, it may be useful to transfer it to a new substrate so it can be combined with other device elements (such as a van der Waals heterostructure) or undergo additional nanofabrication steps.

To combine these three capabilities, we developed a specialized transfer stage that incorporated Rayleigh scattering spectroscopy and imaging. The elastically scattered light from broadband illumination of a suspended CNT enables both direct visualization of the CNT and identification of its chiral indices. Once characterized and located, a desired CNT can be stamped down and transferred to a prepared substrate. This unique tool was critical in the realization of several experiments, including the work described in Chapters 2 and 3 of this thesis and also in Refs. 14, 95. As many of the fabrication details were described in Sections 2.3 and 3.3, this appendix will lay out some of the underlying principles of Rayleigh spectroscopy for carbon nanotubes and give a detailed account of the experimental apparatus as a guide for future researchers.

C.1 Theory of Rayleigh scattering spectroscopy for carbon nanotubes

This topic has been covered extensively in previous publications[96,200]. As such, this section will provide a brief overview of the theory and operating principle of the Rayleigh setup.

As discussed in Section 1.1.2, the 1D confinement of the electrons in a nanotube causes van Hove singularities in the electronic density of states (DOS). Electron-electron interactions lead to the formation of strongly bound exciton states, which dominate the optical response[201]. The resulting

optical transition energies can be probed by a variety of spectroscopic techniques, such as photoluminescence[25] and Raman spectroscopy[26,202]. Rayleigh scattering spectroscopy, so called because it measures the spectrum of an object smaller (in diameter, at least) than the light that it elastically scatters, relies on the same essential physics as the optical absorption process. Since individual nanotubes are so small, their optical absorption is weak[200], and therefore it is more practical to measure their scattering response in a direction that avoids the incident light (darkfield geometry or "off-axis," meaning collected at an angle away from the incident or transmitted beam). The interaction of a nanotube with an incident laser beam induces a dipole moment oscillating at the optical frequency. The collected off-axis scattering signal scales as the radiated electric field squared, which is quadratic in the magnitude of the induced dipole moment ($|\varepsilon - 1|^2$, where ε is the effective dielectric function). As the incident laser wavelength varies, peaks in the resulting scattering spectrum reflect peaks of ε as a function of photon energy, which are a direct reflection of the electronic transitions. The transition energies are typically labeled by both nanotube type (metallic or S1/S2 semiconducting) and the gap index, so $E_{11}^{M}, E_{22}^{M}, E_{33}^{M}\ldots$ are the three lowest-energy transitions for metallic nanotubes and $E_{11}^{1(2)}, E_{22}^{1(2)}, E_{33}^{1(2)}\ldots$ are the three lowest-energy transitions for type 1(2) semiconducting nanotubes.

In 1999, H. Kataura *et al.*[26] reported that the gap energies of nanotubes vary a function of their diameter, producing the "Kataura plot" reproduced in Fig. C.1. A nanotube of any given diameter has multiple bandgaps determined by its chirality; there can be multiple chiral indices that result in a nanotube of the same diameter, but they will not have the same electronic structure or gap energies. Each transition energy ($E_{11}^{1}, E_{11}^{2}, E_{22}^{2}, E_{22}^{1}, E_{11}^{M}\ldots$) will be represented by a different branch on the Kataura plot. Observing several optical transitions is sufficient to uniquely assign chiral indices to a single-walled carbon nanotube.

While Rayleigh scattering spectroscopy is clearly not the only viable method for determining the chirality of a carbon nanotube, it has several key benefits for the purposes of integration into

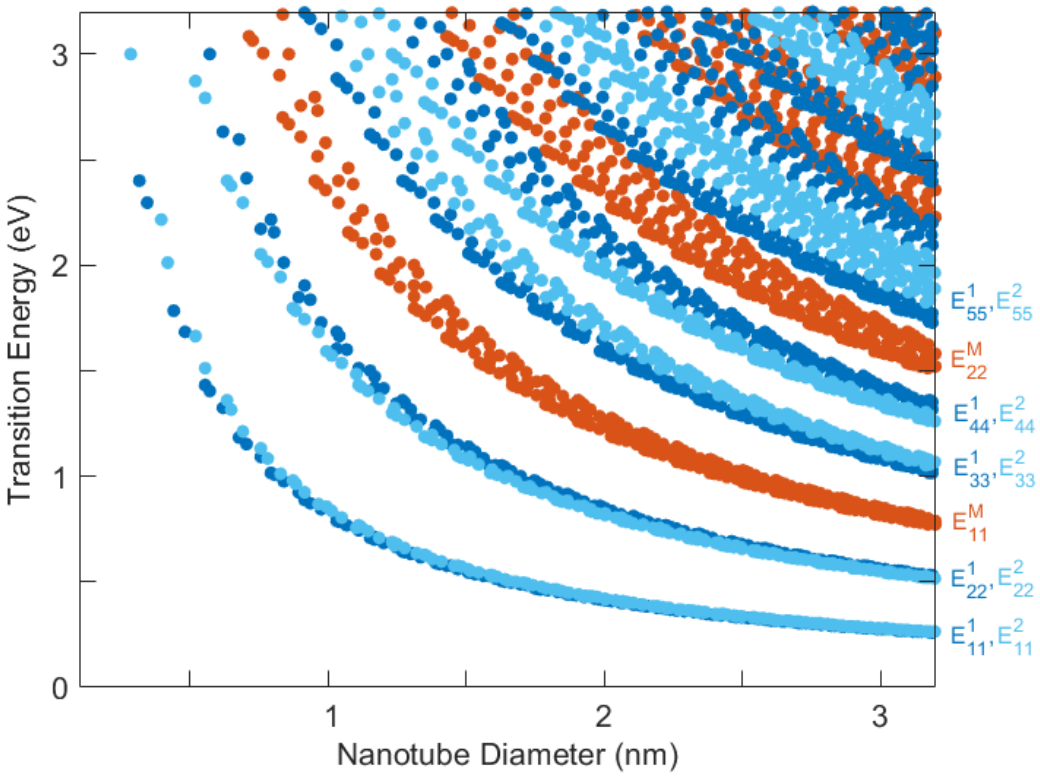

Figure C.1: Kataura plot, showing the relationship between nanotube diameters and their transition energies. The first five optical transitions for semiconducting nanotubes and the first two for metallic tubes are labeled. Data were generated from a tight-binding calculation described in Ref. 14.

the fabrication process. Elastic scattering provides a relative strong signal compared, for example, to inelastic (Raman) scattering. This makes the technique useful for imaging suspended nanotubes, which are otherwise difficult to see or completely invisible to conventional microscopy due to their high aspect ratio and low scattering cross-section [200]. Initial versions of nanotube-graphene drag device fabrication used only Raman spectroscopy for nanotube characterization, with the nanotubes first locally coated with a Cr/Au film deposited via thermal evaporation through a stencil mask. Collecting the Raman spectra also required up to several minutes of acquisition time per nanotube, and the spectrometer was not integrated with a transfer stage. Identifying an individual single-walled, metallic carbon nanotube and keeping track of its position along the slit of the growth chip in order to later transfer to a heterostructure or other substrate was a time-consuming and meticulous process. Additionally, while the metal film rendered portions of the nanotubes visible, it was also found to diffuse along the length of many nanotubes, changing their transport characteristics. In contrast, Rayleigh scattering spectroscopy can be combined with imaging without introducing contamination, can be made high-throughput, and, in our case, was integrated directly with a tranfer stage. The spectroscopic results are also simple to interpret (corresponding directly to optical resonances), and the method works reliably with metallic and semiconducting nanotubes.

C.2 Technical considerations and description of the tool

As mentioned in the previous section, it is most convenient to measure Rayleigh scattering of NTs in a darkfield geometry, either by imaging the CNTs on a transparent substrate and carefully matching the refractive indices of the surrounding media [203], or by imaging CNTs suspended in air [96,200]. While both present technical challenges, the latter geometry is a simpler way to prevent backscattering and is more favorable for transfer to new substrates and preservation of CNT cleanliness, all important factors for incorporation into high-quality mesoscopic devices.

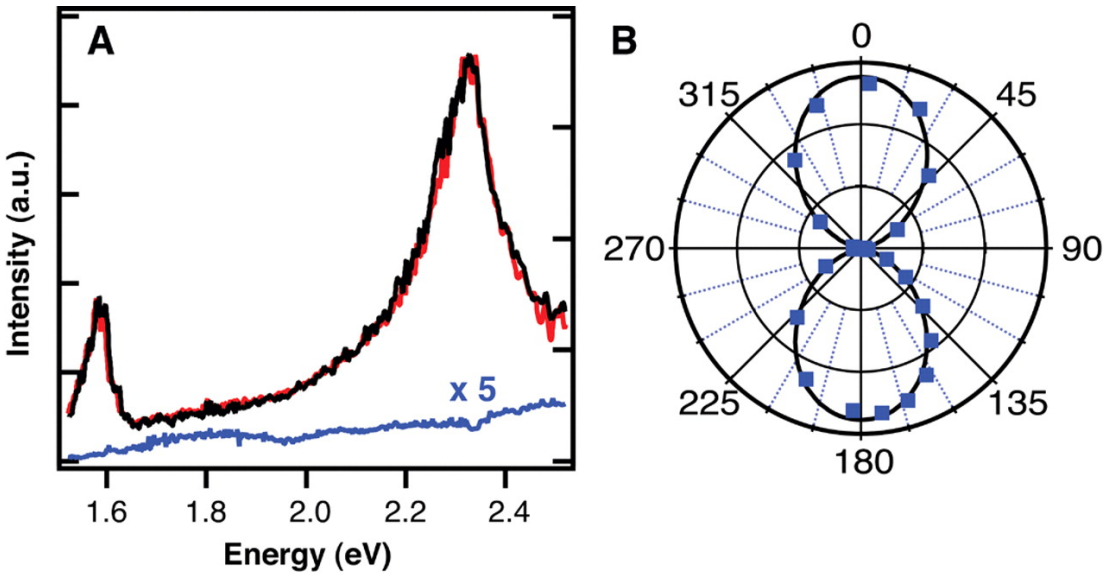

Figure C.2: Polarization dependence of carbon nanotube Rayleigh scattering. (a) Black and red lines show Rayleigh spectra collected from different spots on the same nanotube with incident light polarized parallel to the nanotube axis. Blue line (magnification x 5) shows Rayleigh spectrum from the same nanotube with incident light polarized perpendicular to the nanotube axis. (b) Polar plot of Rayleigh scattering intensity as a function of polarization angle θ of the incident light relative to the nanotube axis. Black line is a $cos^2\theta$ fit. Reproduced from Ref. 24.

Another key feature of the spectroscopy setup is the use of a supercontinuum white light laser as the excitation source. In order to measure various possible transition energies, the wavelength of the light being scattered must be varied across a reasonable subset of the range of roughly 300 nm to 2500 nm. This can be achieved with a tunable laser source, but a broadband laser enables simultaneous measurement at many wavelengths, dramatically decreasing the acquisition time for a single spectrum. It is necessary to assume that inelastic scattering is much weaker than the elastic contribution, but fortunately this is generally true (though measurements of the lowest-energy transitions, E_{11}^1 and E_{22}^2, may pick up significant contributions from inelastic scattering[200]). We used a supercontinuum laser (NKT Photonics SuperK Extreme EXW-12) with a wavelength range of 455-2350 nm, average spectral density approximately 3 mW/nm, and total power of 4 W, which was more than sufficient for excitation of detectable optical response from suspended nanotubes.

A final technical detail that proved critical to improving the quality of the Rayleigh spectra and images of suspended nanotubes was leveraging the strong polarization dependence of the Rayleigh signal to enhance the signal-to-noise ratio, as shown in Figure C.2[24]. The "antenna effect" dramatically reduces the scattering response when the incident light polarization is perpendicular to the long axis of the nanotube[204]. The scattered light is also predominantly polarized along the nanotube axis[200]. Our CVD-grown nanotubes have a strong tendency to grow along the direction of gas flow, so the suspended nanotubes are well-aligned in a known direction, perpendicular the slit over which they are suspended. We can thus introduce polarizing filters into both the incident laser path and the detection path, so that only light along the predominant direction of the nanotubes will be sent to the cameras and spectrometer. This dramatically reduced the level of background signal.

The remainder of this appendix will give a detailed description of the apparatus and its operation. The majority of the parts were purchased from ThorLabs; names in parentheses refer to part numbers (accurate at time of writing).

The transfer stage section of the Rayleigh setup (Figures C.3 and C.4) is an inversion of the more typical transfer stage geometry: lower stage, which supports the target substrate held down by vacuum suction and heated by themocouples attached to the copper block, moves in x, y, and z, while the suspended CNTs are supported by the slide holder and move only in the xy-plane. The fixed z-distance for the CNTs aids in maintaining the focus of the supercontinuum laser at the location of the CNTs.

The fan can be used to speed up cooling of the stage, but should be used with caution, as the resulting vibrations potentially induce strain between the NTs (or whatever is being transferred) and the target substrate. The "height adjust" knob manually controls the fan height. The x, y, and z motion of the lower stage are controlled by one motorized controller (part number), while the x and y motion of the slide holder and z motion of the objectives (i.e. their focal plane) are controlled by a

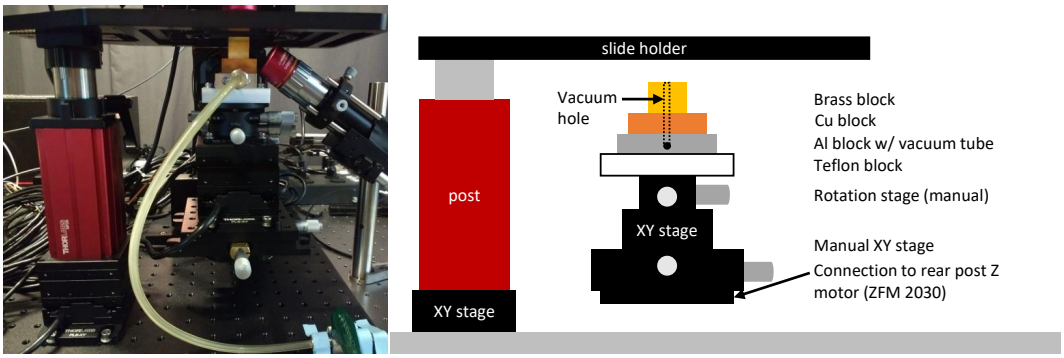

Figure C.3: Front view of stage and manipulators, with photograph (left) and schematic (right). The angled white laser couple visible in the photograph is described in more detail in Figure C.8.

separate controller.

Figures C.5 and C.6 show front and top-down representations of the imaging column, which is the first part of the detection path for the Rayleigh signal and both illumination and detection paths for using the setup as a typical optical microscope. The lenses are Mitutoyo NIR/visible long working distance objectives (it is important to ensure, as much as possible, that all optical components function as intended at the full range of wavelengths of the supercontinuum laser). The lenses are on a turret mounted on a holder connected to the rear supporting column, with a motor (connected to the same controller as the x and y motion of the slide holder) adjusting the height. A flexible bellows connects this to a hole in a upper breadboard, which supports the rest of the imaging column. The vertically-mounted components consist of a 50/50 plate beam splitter (which allows light from the sample to pass through, but also reflects down LED light from the side as illumination for optical microscopy), an adjustable iris aperture (to adjust the amount of light coming in, if the signal is too bright), a polarizing prism (aligned with the nanotube axis, as discussed above), and a mirror (to send the light to the cameras and spectrometer). Behind the column is a white LED light source

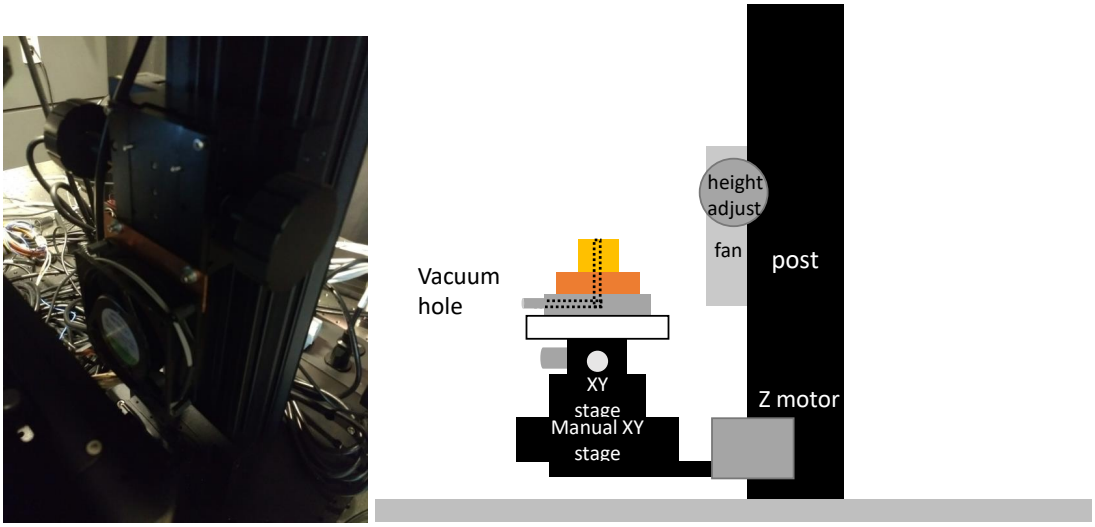

Figure C.4: Side view of stage and manipulators (without slide holder).

used for optical microscopy, which is directed to the imaging column via a mirror and the beam splitter. There are some extraneous optical components visible in the pictures which belong to an attempt to add Raman spectroscopy capabilities to the setup; these were deemed unnecessary, given the reliability of our Rayleigh spectroscopy and imaging.

The last section of the detection path sends the light from the imaging column to another 50/50 beam splitter. One half of the signal is focused through a lens and sent through a camera mount to either a visible-wavelength color camera (used when the transfer stage is being operated for typical van der Waals heterostructure fabrication) or a NIR camera (for Rayleigh imaging; most nanotube transition energies are in the IR range). The other half of the signal is focused through a 20x NIR objective to an optical fiber connected to a spectrometer (Princeton Instruments SpectraPro with PIXIS:400BR eXcelon CCD camera).

Finally, we return to the incident light path (Figure C.8). The supercontinuum laser light is sent

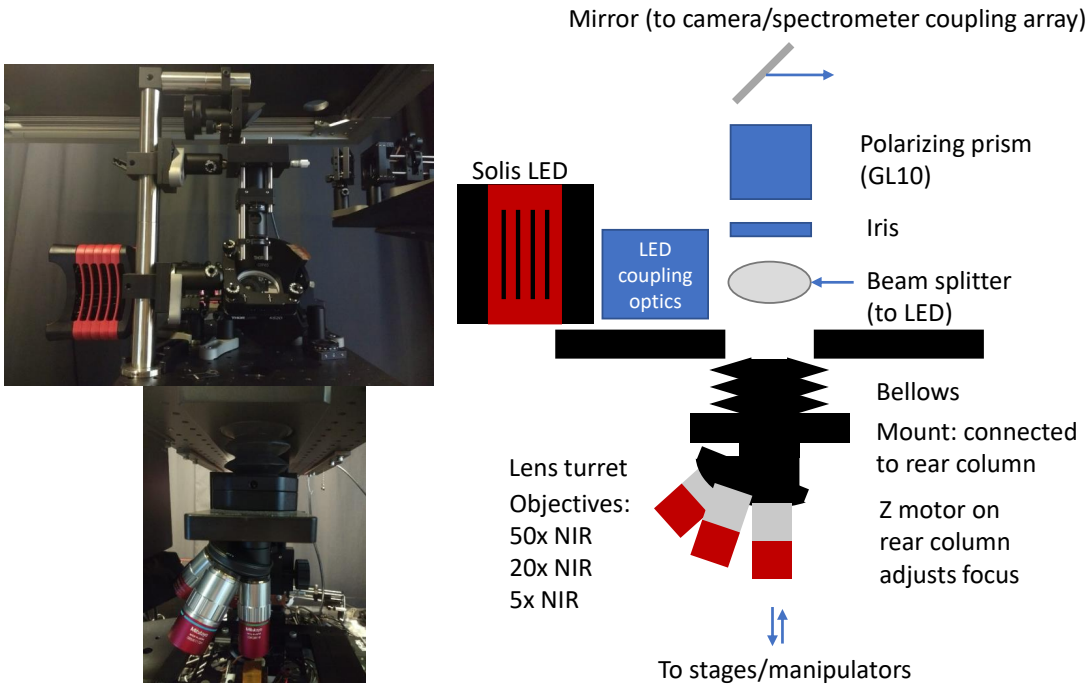

Figure C.5: Imaging column (front view). Some components are presented in unrealistic colors for improved visibility.

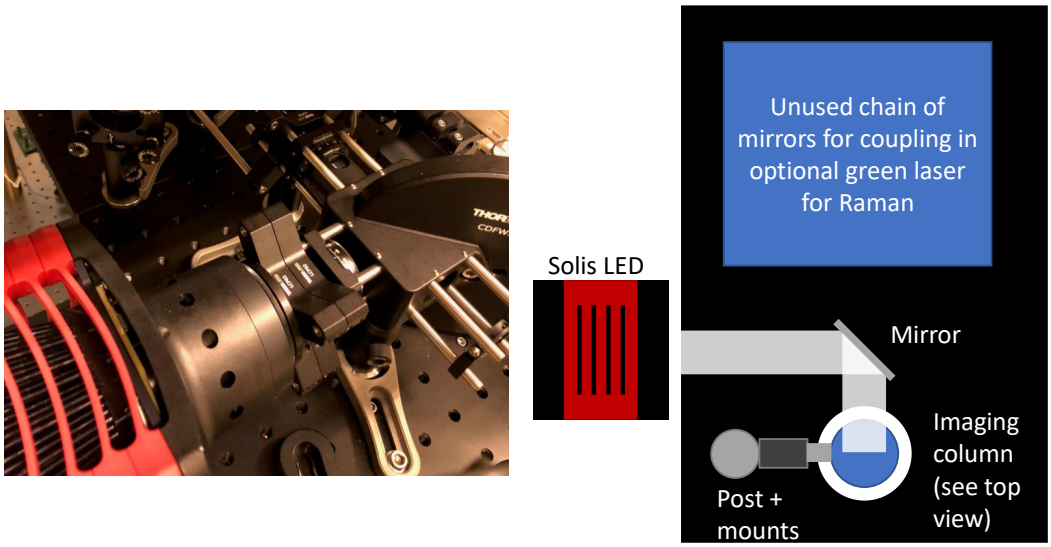

Figure C.6: Imaging column (top view). Unused components on breadboard are mentioned for completeness only. Photo taken by Austin Cheng.

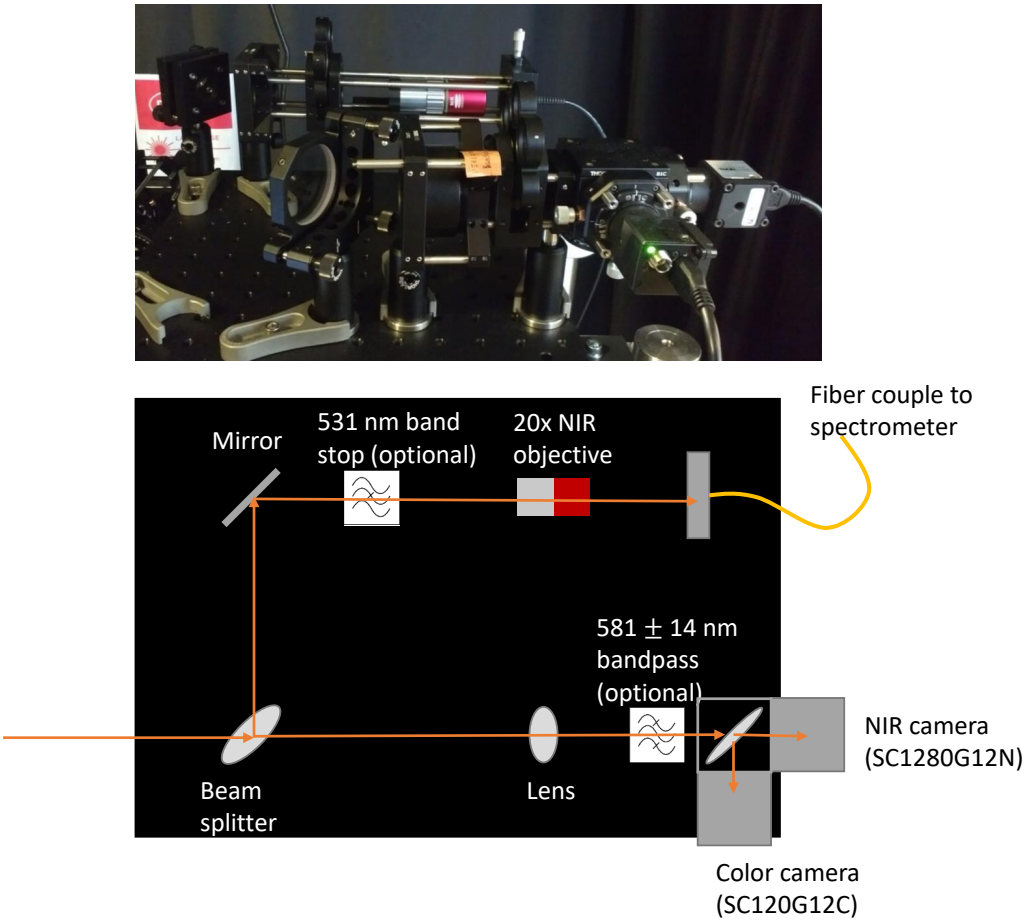

Figure C.7: Camera/spectrometer coupling array (top view). Signal path is represented by orange arrows.

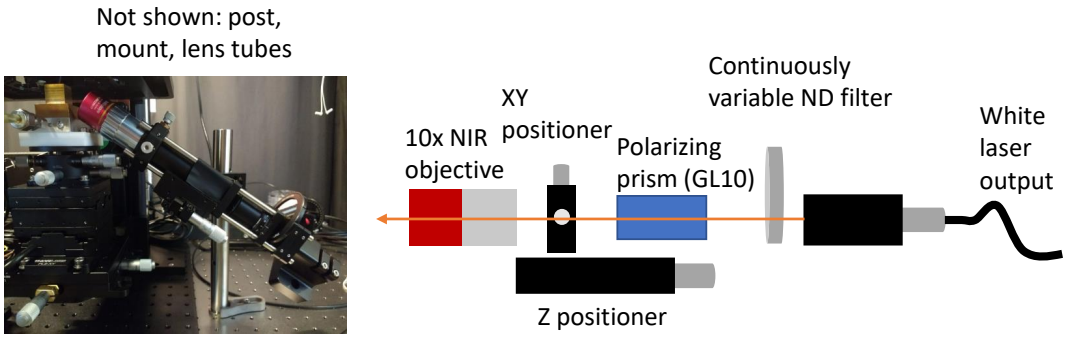

Figure C.8: White laser coupler (lens tubes and mounting post not shown in schematic).

through a continuously variable ND filter (allowing us to reduce the power if needed, in addition to the power adjustment capacity of the laser), a polarizing prism (aligned with the nanotube growth direction), and a 10x NIR objective (to focus the laser on the suspended nanotubes). Manual X-Y and Z positioning knobs allow fine adjustments of the focal point and focal plane. The entire assembly is mounted on a post, so that the laser light shines up at a roughly 30° angle from the optical table, passes through the slit on the nanotube growth chip (over which the nanotubes are suspended), and is stopped by a black beamstop (not shown) to avoid dangerous reflections. Note that in the photogragh (left side of Figure C.8), the light from the objective would be blocked by the metal stage. This is only because the stage was in the raised "contact" position. During imaging, the stage is lowered out of the way of the incident light path.

D

MATLAB code for Rayleigh scattering spectroscopy

This appendix contains the two key MATLAB programs used for identifying nanotubes from spectrometer data, primarily written by Austin Cheng and included here for the reference of future researchers. The first, "rly," prompts the user to select data files for both spectrum and background data (collected when the laser is not illuminating a nanotube) and outputs the spectrum with the

background subtracted. The second, "rlypk," takes the background-corrected spectrum from "rly," asks the user to identify the peak positions (typically using 2 peaks gives the best result), compares the peak positions to the values from a Kataura plot, and outputs the results of the fit.

D.1 Background subtraction program (rly.m)

```
function [Wavelength,Energy,Result]=rly(CNTFullFilePath,BackgroundFullFilePath,LaserFullFilePath)

if nargin==0
    % Select CNT Signal Data
    [CNTFileName, CNTPathName] = uigetfile( ...
    {'*.csv','Text Files (*.csv)'; ...
    '*.txt','Text Files (*.txt)'; ...
    '*.*',  'All Files (*.*)'}, ...
    'Pick CNT Signal Data','C:\Users\Kim Lab Rayleigh\Documents\LightField\2018');
    CNTFullFilePath=fullfile(CNTPathName, CNTFileName);
    if isequal(CNTFileName,0)
        disp('User selected Cancel')
    else
        disp(['User selected ', CNTFullFilePath])
    end
    % Select Background Signal Data
    [BackgroundFileName, BackgroundPathName] = uigetfile( ...
    {'*.csv','Text Files (*.csv)'; ...
    '*.txt','Text Files (*.txt)'; ...
    '*.*',  'All Files (*.*)'}, ...
    'Pick Background Signal Data','C:\Users\Kim Lab Rayleigh\Documents\LightField\2018');
    BackgroundFullFilePath=fullfile(BackgroundPathName, BackgroundFileName);
    if isequal(BackgroundFileName,0)
        disp('User selected Cancel')
    else
        disp(['User selected ', BackgroundFullFilePath])
    end
    % Select Laser Signal Data
%     [LaserFileName, LaserPathName] = uigetfile( ...
%     {'*.csv','Text Files (*.csv)'; ...
%     '*.txt','Text Files (*.txt)'; ...
```

```
%     '*.*',  'All Files (*.*)'}, ...
%     'Pick Laser Signal Data','C:\Users\Kim Lab Rayleigh\Documents\LightField');
%     LaserFullFilePath=fullfile(LaserPathName, LaserFileName);
%     if isequal(LaserFileName,0)
%         disp('User selected Cancel')
%     else
%         disp(['User selected ', LaserFullFilePath])
%     end
end

% Structure of the file is: Wavelength, Intensity.
tempCNT=importdata(CNTFullFilePath);
tempBackground=importdata(BackgroundFullFilePath);
%tempLaser=importdata(LaserFullFilePath);

CNT=tempCNT(:,2);
Background=tempBackground(:,2);
%Laser=tempLaser(:,2);

% CNT=smooth(tempCNT(:,2),10);
% Background=smooth(tempBackground(:,2),10);
% Laser=smooth(tempLaser(:,2),10);

Wavelength=tempCNT(:,1); % wavelength in nanometers

%Constants
h=6.62607*10^-34; % Planck's Constant
c=3*10^8; % Speed of light in m/s
ec=1.60217662*10^-19; % Elementary Charge
Energy=h*c./(Wavelength*10^-9*ec);

%Result=(CNT-Background)./(Laser-Background);
%Result=(CNT-Background)./(Background);
Result=CNT-Background;
%Result=CNT;
%Result=deleteoutliers(Result,0.05,1);
%Result=smooth(Result,10);
% Plot
figure(1);
plot(Energy,Result,'b','LineWidth',2);
xlabel('Transition energy (eV)');
```

```
ylabel('Intensity (a.u.)');
xmax=h*c./(450*10^-9*ec);
xmin=h*c./(1100*10^-9*ec);
xlim([xmin xmax]);

CombinedResult=[Wavelength Energy Result];

%Output to specific directory
Out_pre='Out_';
Outfile=[Out_pre CNTFileName]; %name output file as 'Out_importfilename'
Outfullpath=fullfile(CNTPathName,Outfile);
save (Outfullpath,'CombinedResult', '-ascii', '-tabs');
```

D.2 Peak fitting program (rlypk.m)

```
    function [eVpk,out]=rlypk(eVpk)
% The acceptable error of peak position in eV
error=0.05;

% Constants
h=6.62607*10^-34; % Planck's Constant
c=3*10^8; % Speed of light in m/s
ec=1.60217662*10^-19; % Elementary Charge

% Load kataura table
katauratable=load('katauraS6.mat');
kataura=table2array(katauratable.katauraS6);
kataurasize=size(kataura);
katauralength=kataurasize(1);
% Add additional column to kataura array for fitting parameter
kataura=[kataura zeros(katauralength,1)];
dupkataura=kataura;
dupdupkataura=kataura;
%%%%%%%%%%%%%%%%%%%%%%%
if nargin==0
% Select Rayleigh spectrum with prefix Out_
    [rlyFileName,rlyPathName] = uigetfile( ...
    {'*.csv','Text Files (*.csv)'; ...
    '*.txt','Text Files (*.txt)'; ...
    '*.*',  'All Files (*.*)'}, ...
```

```
    'Pick CNT Rayleigh Spectrum','D:\Rayleigh\2018');
    rlyFullFilePath=fullfile(rlyPathName, rlyFileName);
    if isequal(rlyFileName,0)
        disp('User selected Cancel')
    else
        disp(['User selected ', rlyFullFilePath])
    end
% Select Rayleigh peak positions
rlyspec=importdata(rlyFullFilePath);
figure(2);hold on;
h_plot=plot(rlyspec(:,2),rlyspec(:,3),'b','LineWidth',2);
xlabel('Transition energy (eV)');
ylabel('Intensity (counts)');
[eVpk,pk]=ginput(6);
scatter(eVpk,pk,'r')
end

close Figure 2
%%%%%%%%%%%%%%%%%%%%%%%%%

eVpklength=length(eVpk);
result=[];
% Find closest match in eV peak position with Kataura values
for j = 1:7-eVpklength
    for i=1:eVpklength
        dupkataura(:,5+i+j)=abs(kataura(:,5+i+j)-eVpk(i));
        dupkataura((dupkataura(:,5+i+j)>error),:)=NaN;
    end
    dupdupkataura(:,13)=sum(dupkataura(:,6+j:6+j+eVpklength-1),2);
    result = vertcat(dupdupkataura(all(~isnan(dupkataura(:,1:6)),2),:),result);
    dupkataura=kataura;
    dupdupkataura=kataura;
end
% Sort the matches. Showing best match first.
result=sortrows(result,13);
% Remove repeated matches. Keeping the first match. The original ordering is not kept.
[C,ia,ic]=unique(result(:,1:2),'rows','first');
result=result(ia,:);
% Reorder the matches by showing the best match first.
result=sortrows(result,13);
% Create table to show matches
```

```
n=result(:,1);
m=result(:,2);
Type=num2str(result(:,4));
Type(Type=='0')='M';
Diameter=result(:,5);
ChiralAngle=result(:,6);
E11eV=result(:,7);
E22eV=result(:,8);
E33eV=result(:,9);
E44eV=result(:,10);
E55eV=result(:,11);
E66eV=result(:,12);
Fit=result(:,13);
out=table(n,m,Type,Diameter,ChiralAngle,E11eV,E22eV,E33eV,E44eV,E55eV,E66eV,Fit);
```

References

[1] S. Datta, *Electronic Transport in Mesoscopic Systems*, 1st ed. (Cambridge University Press, Cambridge, 1995).

[2] W. G. van der Wiel, S. D. Franceschi, T. Fujisawa, J. M. Elzerman, S. Tarucha, and L. P. Kouwenhoven, Science **289**, 2105 (2000).

[3] R. Scheibner, H. Buhmann, D. Reuter, M. N. Kiselev, and L. W. Molenkamp, Physical Review Letters **95**, 176602 (2005).

[4] Z. Shi, X. Hong, H. A. Bechtel, B. Zeng, M. C. Martin, K. Watanabe, T. Taniguchi, Y.-R. Shen, and F. Wang, Nature Photonics **9**, 515 (2015).

[5] A. Lucas and K. C. Fong, Journal of Physics: Condensed Matter **30**, 053001 (2018), arXiv:1710.08425 .

[6] K. v. Klitzing, G. Dorda, and M. Pepper, Physical Review Letters **45**, 494 (1980).

[7] K. S. Novoselov, A. K. Geim, S. V. Morozov, D. Jiang, Y. Zhang, S. V. Dubonos, I. V. Grigorieva, and A. A. Firsov, Science **306**, 666 (2004).

[8] C. R. Dean, A. F. Young, I. Meric, C. Lee, L. Wang, S. Sorgenfrei, K. Watanabe, T. Taniguchi, P. Kim, K. L. Shepard, and J. Hone, Nature Nanotechnology **5**, 722 (2010), arXiv:1005.4917 .

[9] L. Wang, I. Meric, P. Y. Huang, Q. Gao, Y. Gao, H. Tran, T. Taniguchi, K. Watanabe, L. M. Campos, D. A. Muller, J. Guo, P. Kim, J. Hone, K. L. Shepard, and C. R. Dean, Science **342**, 614 (2013).

[10] Y. Cao, V. Fatemi, S. Fang, K. Watanabe, T. Taniguchi, E. Kaxiras, and P. Jarillo-Herrero, Nature **556**, 43 (2018).

[11] L. Fritz, J. Schmalian, M. Müller, and S. Sachdev, Physical Review B **78**, 085416 (2008), arXiv:0802.4289 .

[12] M. Müller, J. Schmalian, and L. Fritz, Physical Review Letters **103**, 025301 (2009), arXiv:0903.4178 .

[13] L. Levitov and G. Falkovich, Nature Physics **12**, 672 (2016), arXiv:1508.00836 .

[14] A. Cheng, *Electric Transport in Hybrid Carbon Nanotube-Graphene Devices*, Ph.d., Harvard University (2019).

[15] H.-S. P. Wong and D. Akinwande, *Carbon Nanotube and Graphene Device Physics* (Cambridge University Press, Cambridge, 2010) pp. 139–148.

[16] A. H. Castro Neto, F. Guinea, N. M. R. Peres, K. S. Novoselov, and A. K. Geim, Reviews of Modern Physics **81**, 109 (2009), arXiv:0709.1163 .

[17] S. Ilani and P. L. McEuen, Annual Review of Condensed Matter Physics **1**, 1 (2010).

[18] J. Crossno, J. K. Shi, K. Wang, X. Liu, A. Harzheim, A. Lucas, S. Sachdev, P. Kim, T. Taniguchi, K. Watanabe, T. A. Ohki, and K. C. Fong, Science **351**, 1058 (2016).

[19] P. Gallagher, C. S. Yang, T. Lyu, F. Tian, R. Kou, H. Zhang, K. Watanabe, T. Taniguchi, and F. Wang, Science **364**, 158 (2019).

[20] M. J. H. Ku, T. X. Zhou, Q. Li, Y. J. Shin, J. K. Shi, C. Burch, L. E. Anderson, A. T. Pierce, Y. Xie, A. Hamo, U. Vool, H. Zhang, F. Casola, T. Taniguchi, K. Watanabe, M. M. Fogler, P. Kim, A. Yacoby, and R. L. Walsworth, Nature **583**, 537 (2020).

[21] T. Ando, T. Nakanishi, and R. Saito, Journal of the Physical Society of Japan **67**, 2857 (1998).

[22] Y. Zhang, Y. W. Tan, H. L. Stormer, and P. Kim, Nature **438**, 201 (2005), arXiv:0509355 [cond-mat] .

[23] H. Aoki and M. S. Dresselhaus, eds., *The Physics of Graphene* (Springer, 2014).

[24] M. Y. Sfeir, F. Wang, L. Huang, C. C. Chuang, J. Hone, S. P. O'Brien, T. F. Heinz, and L. E. Brus, Science **306**, 1540 (2004).

[25] A. Hartschuh, H. N. Pedrosa, J. Peterson, L. Huang, P. Anger, H. Qian, A. J. Meixner, M. Steiner, L. Novotny, and T. D. Krauss, ChemPhysChem **6**, 577 (2005).

[26] H. Kataura, Y. Kumazawa, Y. Maniwa, I. Umezu, S. Suzuki, Y. Ohtsuka, and Y. Achiba, Synthetic Metals **103**, 2555 (1999).

[27] P. L. McEuen, M. Bockrath, D. H. Cobden, Y.-G. Yoon, and S. G. Louie, Physical Review Letters **83**, 5098 (1999).

[28] G. Falkovich and L. Levitov, Physical Review Letters **119**, 1 (2017), arXiv:1607.00986 .

[29] N. W. Ashcroft and M. N. David, *Solid State Physics*, college ed ed. (Harcourt College Publishers, Orlando, FL, 1976) p. 826.

[30] Y. M. Zuev, *Nanoscale Thermoelectric Energy Conversion*, Phd thesis, Columbia University (2011).

[31] L. Onsager, Physical Review **37**, 405 (1931).

[32] R. Franz and G. Wiedemann, Annalen der Physik und Chemie **165**, 497 (1853).

[33] N. Wakeham, A. F. Bangura, X. Xu, J.-F. Mercure, M. Greenblatt, and N. E. Hussey, Nature communications **2**, 396 (2011).

[34] R. W. Hill, C. Proust, L. Taillefer, P. Fournier, and R. L. Greene, Nature **414**, 711 (2001).

[35] V. Venkatachalam, S. Hart, L. Pfeiffer, K. West, and A. Yacoby, Nature Physics **8**, 676 (2012), arXiv:1202.6681 .

[36] M. Li and G. Chen, MRS Bulletin **45**, 348 (2020), arXiv:1912.12767 .

[37] J. Waissman, L. E. Anderson, A. V. Talanov, Z. Yan, Y. J. Shin, D. H. Najafabadi, M. Rezaee, X. Feng, D. G. Nocera, T. Taniguchi, K. Watanabe, B. Skinner, K. A. Matveev, and P. Kim, Nature Nanotechnology **17**, 166 (2022), arXiv:2101.01737 .

[38] F. Reif, *Fundamentals of statistical and thermal physics* (McGraw-Hill, Boston, 1965).

[39] B. Dutta, J. T. Peltonen, D. S. Antonenko, M. Meschke, M. A. Skvortsov, B. Kubala, J. König, C. B. Winkelmann, H. Courtois, and J. P. Pekola, Physical Review Letters **119**, 1 (2017).

[40] J. Crossno, X. Liu, T. A. Ohki, P. Kim, and K. C. Fong, Applied Physics Letters **106**, 10.1063/1.4905926 (2015).

[41] K. C. Fong and K. C. Schwab, Physical Review X **2**, 031006 (2012), arXiv:1202.5737 .

[42] M. Jonson and G. D. Mahan, Physical Review B **21**, 4223 (1980).

[43] F. Ghahari Kermani, *Interaction Effects on Electric and Thermoelectric Transport in Graphene*, Phd thesis, Columbia University (2014).

[44] J. Zaanen, Science **351**, 1026 (2016).

[45] R. Gurzhi, Uspekhi Fizicheskih Nauk **94**, 689 (1968).

[46] L. W. Molenkamp and M. J. de Jong, Solid State Electronics **37**, 551 (1994).

[47] J. Xue, J. Sanchez-Yamagishi, D. Bulmash, P. Jacquod, A. Deshpande, K. Watanabe, T. Taniguchi, P. Jarillo-Herrero, and B. J. Leroy, Nature Materials **10**, 282 (2011), arXiv:1102.2642 .

[48] D. K. Efetov and P. Kim, Physical Review Letters **105**, 2 (2010), arXiv:1009.2988 .

[49] D. Y. H. Ho, I. Yudhistira, N. Chakraborty, and S. Adam, Physical Review B **97**, 121404 (2018), arXiv:1710.10272 .

[50] D. J. Acheson, *Elementary Fluid Dynamics* (Oxford University Press, Oxford, 1990).

[51] R. V. Gorbachev, A. K. Geim, M. I. Katsnelson, K. S. Novoselov, T. Tudorovskiy, I. V. Grigorieva, A. H. MacDonald, S. V. Morozov, K. Watanabe, T. Taniguchi, and L. A. Ponomarenko, Nature Physics **8**, 896 (2012), arXiv:1206.6626 .

[52] X. Liu, L. Wang, K. C. Fong, Y. Gao, P. Maher, K. Watanabe, T. Taniguchi, J. Hone, C. Dean, and P. Kim, Physical Review Letters **119**, 056802 (2017), arXiv:1612.08308 .

[53] K. S. Novoselov, A. K. Geim, S. V. Morozov, D. Jiang, M. I. Katsnelson, I. V. Grigorieva, S. V. Dubonos, and A. A. Firsov, Nature **438**, 197 (2005).

[54] K. S. Novoselov, Z. Jiang, Y. Zhang, S. V. Morozov, H. L. Stormer, U. Zeitler, J. C. Maan, G. S. Boebinger, P. Kim, and A. K. Geim, Science **315**, 1379 (2007), arXiv:0702408 [cond-mat] .

[55] K. I. Bolotin, F. Ghahari, M. D. Shulman, H. L. Stormer, and P. Kim, Nature **462**, 196 (2009), arXiv:0910.2763 .

[56] F. D. Haldane, Physical Review Letters **61**, 2015 (1988).

[57] Y. Aharonov and A. Casher, Physical Review A **19**, 2461 (1979).

[58] B. I. Halperin, Physical Review B **25**, 2185 (1982), arXiv:9506066v2 [arXiv:cond-mat] .

[59] D. B. Chklovskii, B. I. Shklovskii, and L. I. Glazman, Physical Review B **46**, 4026 (1992).

[60] D. Tong, in *TIFR Infosys Lectures*, January (2016).

[61] J. G. Checkelsky and N. P. Ong, Physical Review B - Condensed Matter and Materials Physics **80**, 1 (2009), arXiv:0812.2866 .

[62] S. M. Girvin and M. Jonson, Journal of Physics C: Solid State Physics **15**, 10.1088/0022-3719/15/32/006 (1982).

[63] S. Sachdev and J. Ye, Physical Review Letters **70**, 3339 (1993), arXiv:9212030 [cond-mat] .

[64] A. Kitaev, in *KITP Program: Entanglement in Strongly-Correlated Quantum Matter* (2015).

[65] S. A. Hartnoll, A. Lucas, and S. Sachdev, *Holographic quantum matter* (MIT Press, Cambridge, MA, 2018) arXiv:1612.07324 .

[66] J. Maldacena, S. H. Shenker, and D. Stanford, Journal of High Energy Physics **2016**, 10.1007/JHEP08(2016)106 (2016), arXiv:1503.01409 .

[67] B. N. Narozhny and A. Levchenko, Reviews of Modern Physics **88**, 025003 (2016), arXiv:1505.07468 .

[68] T. J. Gramila, J. P. Eisenstein, A. H. MacDonald, L. N. Pfeiffer, and K. W. West, Physical Review Letters **66**, 1216 (1991).

[69] N. P. R. Hill, J. T. Nicholls, E. H. Linfield, M. Pepper, D. A. Ritchie, A. R. Hamilton, and G. A. C. Jones, Journal of Physics: Condensed Matter **8**, L557 (1996).

[70] S. Kim, I. Jo, J. Nah, Z. Yao, S. K. Banerjee, and E. Tutuc, Physical Review B **83**, 161401 (2011), arXiv:1010.2113 .

[71] M. Yamamoto, M. Stopa, Y. Tokura, Y. Hirayama, and S. Tarucha, Science **313**, 204 (2006).

[72] D. Laroche, G. Gervais, M. P. Lilly, and J. L. Reno, Nature Nanotechnology **6**, 793 (2011), arXiv:arXiv:1008.5155v3 .

[73] D. Laroche, G. Gervais, M. P. Lilly, and J. L. Reno, Science **343**, 631 (2014), arXiv:1312.4950 .

[74] A. G. Rojo, Journal of Physics: Condensed Matter **11** (1999).

[75] M. Titov, R. V. Gorbachev, B. N. Narozhny, T. Tudorovskiy, M. Schütt, P. M. Ostrovsky, I. V. Gornyi, A. D. Mirlin, M. I. Katsnelson, K. S. Novoselov, A. K. Geim, and L. A. Ponomarenko, Physical Review Letters **111**, 1 (2013), arXiv:1303.6264 .

[76] J. C. W. Song and L. S. Levitov, Physical Review Letters **111**, 126601 (2013), arXiv:1303.3529 .

[77] J. C. W. Song and L. S. Levitov, Physical Review Letters **109**, 236602 (2012), arXiv:1205.5257 .

[78] J. C. W. Song, D. A. Abanin, and L. S. Levitov, Nano Letters **13**, 3631 (2013), arXiv:1304.1450 .

[79] X. Liu, *Correlated Electron States in Coupled Graphene Double-layer Heterostructures*, Ph.d., Harvard University (2018).

[80] X. Liu, J. I. A. Li, K. Watanabe, T. Taniguchi, J. Hone, B. I. Halperin, P. Kim, and C. R. Dean, Science **375**, 205 (2022), arXiv:2012.05916 .

[81] Z. Wang, D. A. Rhodes, K. Watanabe, T. Taniguchi, J. C. Hone, J. Shan, and K. F. Mak, Nature **574**, 76 (2019).

[82] Y. M. Sirenko and P. Vasilopoulos, Physical Review B **46**, 1611 (1992).

[83] S. K. Lyo, Physical Review B **68**, 045310 (2003).

[84] R. Mitra, M. R. Sahu, K. Watanabe, T. Taniguchi, H. Shtrikman, A. K. Sood, and A. Das, Physical Review Letters **124**, 116803 (2020), arXiv:2002.09874 .

[85] R. Mitra, M. R. Sahu, A. Sood, T. Taniguchi, K. Watanabe, H. Shtrikman, S. Mukerjee, A. K. Sood, and A. Das, arXiv preprint (2020), arXiv:2009.08882 .

[86] E. A. Laird, F. Kuemmeth, G. A. Steele, K. Grove-Rasmussen, J. Nygård, K. Flensberg, and L. P. Kouwenhoven, Reviews of Modern Physics **87**, 703 (2015), arXiv:1403.6113 .

[87] S. M. Badalyan and A. P. Jauho, Physical Review Research **2**, 013086 (2020), arXiv:1906.05517 .

[88] B. N. Narozhny, M. Titov, I. V. Gornyi, and P. M. Ostrovsky, Physical Review B **85**, 195421 (2012), arXiv:1110.6359 .

[89] D. A. Bandurin, I. Torre, R. K. Kumar, M. Ben Shalom, A. Tomadin, A. Principi, G. H. Auton, E. Khestanova, K. S. Novoselov, I. V. Grigorieva, L. A. Ponomarenko, A. K. Geim, and M. Polini, Science **351**, 1055 (2016), arXiv:1509.04165 .

[90] R. Krishna Kumar, D. A. Bandurin, F. M. D. Pellegrino, Y. Cao, A. Principi, H. Guo, G. H. Auton, M. Ben Shalom, L. A. Ponomarenko, G. Falkovich, K. Watanabe, T. Taniguchi, I. V. Grigorieva, L. S. Levitov, M. Polini, and A. K. Geim, Nature Physics **13**, 1182 (2017), arXiv:1703.06672 .

[91] A. I. Berdyugin, S. G. Xu, F. M. D. Pellegrino, R. Krishna Kumar, A. Principi, I. Torre, M. Ben Shalom, T. Taniguchi, K. Watanabe, I. V. Grigorieva, M. Polini, A. K. Geim, and D. A. Bandurin, Science **364**, 162 (2019), arXiv:1806.01606 .

[92] A. Shytov, J. F. Kong, G. Falkovich, and L. Levitov, Physical Review Letters **121**, 176805 (2018), arXiv:1806.09538 .

[93] D. Svintsov, Physical Review B **97**, 121405 (2018).

[94] J. A. Sulpizio, L. Ella, A. Rozen, J. Birkbeck, D. J. Perello, D. Dutta, M. Ben-Shalom, T. Taniguchi, K. Watanabe, T. Holder, R. Queiroz, A. Principi, A. Stern, T. Scaffidi, A. K. Geim, and S. Ilani, Nature **576**, 75 (2019), arXiv:1905.11662 .

[95] A. Cheng, T. Taniguchi, K. Watanabe, P. Kim, and J.-D. Pillet, Physical Review Letters **123**, 216804 (2019), arXiv:1910.13307 .

[96] M. Y. Sfeir, T. Beetz, F. Wang, L. Huang, X. M. H. Huang, M. Huang, J. Hone, S. O'Brien, J. A. Misewich, T. F. Heinz, L. Wu, Y. Zhu, and L. E. Brus, Science **312**, 554 (2006).

[97] B. Peng, Y. Yao, and J. Zhang, Journal of Physical Chemistry C **114**, 12960 (2010).

[98] X. M. H. Huang, R. Caldwell, L. Huang, S. C. Jun, M. Huang, M. Y. Sfeir, S. P. O'Brien, and J. Hone, Nano Letters **5**, 1515 (2005).

[99] Q. Cao, S.-J. Han, J. Tersoff, A. D. Franklin, Y. Zhu, Z. Zhang, G. S. Tulevski, J. Tang, and W. Haensch, Science **350**, 68 (2015).

[100] J.-W. Huang, C. Pan, S. Tran, B. Cheng, K. Watanabe, T. Taniguchi, C. N. Lau, and M. Bockrath, Nano Letters **15**, 6836 (2015).

[101] W. Kim, A. Javey, R. Tu, J. Cao, Q. Wang, and H. Dai, Applied Physics Letters **87**, 173101 (2005).

[102] G. Pitner, G. Hills, J. P. Llinas, K.-M. Persson, R. Park, J. Bokor, S. Mitra, and H.-S. P. Wong, Nano Letters **19**, 1083 (2019).

[103] H. B. G. Casimir, Reviews of Modern Physics **17**, 343 (1945).

[104] P. Mazur, Periodica Polytechnica Chemical Engineering **41**, 197 (1997).

[105] E. H. Hwang, R. Sensarma, and S. Das Sarma, Physical Review B - Condensed Matter and Materials Physics **84**, 1 (2011).

[106] L. Anderson, A. Cheng, T. Taniguchi, K. Watanabe, and P. Kim, Physical Review Letters **127**, 257701 (2021), arXiv:2106.10246 .

[107] J. I. A. Li, T. Taniguchi, K. Watanabe, J. Hone, A. Levchenko, and C. R. Dean, Physical Review Letters **117**, 046802 (2016), arXiv:1602.01039 .

[108] S. J. Blundell and K. M. Blundell, *Concepts in Thermal Physics*, 2nd ed. (Oxford University Press, Oxford, 2009) pp. 413–415.

[109] J. Martin, N. Akerman, G. Ulbricht, T. Lohmann, J. H. Smet, K. von Klitzing, and A. Yacoby, Nature Physics **4**, 144 (2008), arXiv:0705.2180 .

[110] N. J. Couto, D. Costanzo, S. Engels, D. K. Ki, K. Watanabe, T. Taniguchi, C. Stampfer, F. Guinea, and A. F. Morpurgo, Physical Review X **4**, 1 (2014), arXiv:1401.5356 .

[111] K. K. Ng, *Complete Guide to Semiconductor Devices*, 1st ed. (McGraw-Hill, New York, NY, 1995).

[112] K. Zhang, Y. Feng, F. Wang, Z. Yang, and J. Wang, Journal of Materials Chemistry C **5**, 11992 (2017).

[113] A. Laturia, M. L. Van de Put, and W. G. Vandenberghe, npj 2D Materials and Applications **2**, 6 (2018).

[114] J. H. Seol, I. Jo, A. L. Moore, L. Lindsay, Z. H. Aitken, M. T. Pettes, X. Li, Z. Yao, R. Huang, D. Broido, N. Mingo, R. S. Ruoff, and L. Shi, Science **328**, 213 (2010).

[115] D. C. Elias, R. V. Gorbachev, A. S. Mayorov, S. V. Morozov, A. A. Zhukov, P. Blake, L. A. Ponomarenko, I. V. Grigorieva, K. S. Novoselov, F. Guinea, and A. K. Geim, Nature Physics **7**, 701 (2011), arXiv:1104.1396 .

[116] R. Nicklow, N. Wakabayashi, and H. G. Smith, Physical Review B **5**, 4951 (1972).

[117] W. Lu, D. Wang, and L. Chen, Nano Letters **7**, 2729 (2007).

[118] B. Kozinsky and N. Marzari, Physical Review Letters **96**, 166801 (2006), arXiv:0602599 [cond-mat] .

[119] N. M. R. Peres, J. M. B. Lopes dos Santos, and A. H. Castro Neto, EPL (Europhysics Letters) **95**, 18001 (2011).

[120] S. Ilani, L. A. K. Donev, M. Kindermann, and P. L. McEuen, Nature Physics **2**, 687 (2006).

[121] F. M. D. Pellegrino, I. Torre, and M. Polini, Physical Review B **96**, 195401 (2017), arXiv:1706.08363 .

[122] D. A. Abanin, S. V. Morozov, L. A. Ponomarenko, R. V. Gorbachev, A. S. Mayorov, M. I. Katsnelson, K. Watanabe, T. Taniguchi, K. S. Novoselov, L. S. Levitov, and A. K. Geim, Science **332**, 328 (2011).

[123] D. A. Bandurin, A. V. Shytov, L. S. Levitov, R. K. Kumar, A. I. Berdyugin, M. Ben Shalom, I. V. Grigorieva, A. K. Geim, and G. Falkovich, Nature Communications **9**, 4533 (2018), arXiv:1806.03231 .

[124] A. Aharon-Steinberg, A. Marguerite, D. J. Perello, K. Bagani, T. Holder, Y. Myasoedov, L. S. Levitov, A. K. Geim, and E. Zeldov, Nature **593**, 528 (2021), arXiv:2012.02842 .

[125] J. B. Johnson, Physical Review **32**, 97 (1928).

[126] H. Nyquist, Physical Review **32**, 110 (1928).

[127] K. C. Fong, E. E. Wollman, H. Ravi, W. Chen, A. A. Clerk, M. D. Shaw, H. G. Leduc, and K. C. Schwab, Physical Review X **3**, 1 (2014), arXiv:1308.2265 .

[128] S. Yiğen and A. R. Champagne, Nano Letters **14**, 289 (2014).

[129] E. V. Sukhorukov and D. Loss, Physical Review B - Condensed Matter and Materials Physics **59**, 13054 (1999).

[130] A. V. Talanov, J. Waissman, T. Taniguchi, K. Watanabe, and P. Kim, Review of Scientific Instruments **92**, 014904 (2021), arXiv:2008.12739 .

[131] C. L. Kane and M. P. A. Fisher, Physical Review Letters **76**, 3192 (1996), arXiv:9610037 [cond-mat] .

[132] M.-R. Li and E. Orignac, Europhysics Letters **60**, 4 (2002), arXiv:0201291 [cond-mat] .

[133] M. S. Purewal, B. H. Hong, A. Ravi, B. Chandra, J. Hone, and P. Kim, Physical Review Letters **98**, 2 (2007), arXiv:0704.0300 .

[134] A. Garg, D. Rasch, E. Shimshoni, and A. Rosch, Physical Review Letters **103**, 1 (2009), arXiv:0903.3054 .

[135] S. Frank, P. Poncharal, Z. L. Wang, and W. A. de Heer, Science **280**, 1744 (1998).

[136] C. T. White and T. N. Todorov, Nature **393**, 240 (1998).

[137] P. Poncharal, C. Berger, Y. Yi, Z. L. Wang, and W. A. de Heer, The Journal of Physical Chemistry B **106**, 12104 (2002).

[138] A. Javey, J. Guo, Q. Wang, M. Lundstrom, and H. Dai, Nature **424**, 654 (2003).

[139] I. V. Krive, Low Temperature Physics **24**, 377 (1998).

[140] R. Fazio, F. W. J. Hekking, and D. E. Khmelnitskii, Physical Review Letters **80**, 5611 (1998).

[141] I. Shapir, A. Hamo, S. Pecker, C. P. Moca, Legeza, G. Zarand, and S. Ilani, Science **364**, 870 (2019).

[142] A. Chen, R. Ilan, F. de Juan, D. I. Pikulin, and M. Franz, Physical Review Letters **121**, 036403 (2018), arXiv:1802.00802 .

[143] O. Can, E. M. Nica, and M. Franz, Physical Review B **99**, 045419 (2019), arXiv:1808.06584 .

[144] A. Kruchkov, A. A. Patel, P. Kim, and S. Sachdev, Physical Review B **101**, 205148 (2020), arXiv:1912.02835 .

[145] S.-S. Lee, Annual Review of Condensed Matter Physics **9**, 227 (2018), arXiv:1703.08172 .

[146] S. Sachdev, Physical Review X **5**, 1 (2015), arXiv:1506.05111 .

[147] C. C. Homes, S. V. Dordevic, M. Strongin, D. A. Bonn, R. Liang, W. H. Hardy, S. Komiya, Y. Ando, G. Yu, N. Kaneko, X. Zhao, M. Greven, D. N. Basov, and T. Timusk, Nature **430**, 539 (2004).

[148] J. Zaanen, Nature **430**, 512 (2004).

[149] J. A. N. Bruin, H. Sakai, R. S. Perry, and A. P. Mackenzie, Science **339**, 804 (2013).

[150] A. Legros, S. Benhabib, W. Tabis, F. Laliberté, M. Dion, M. Lizaire, B. Vignolle, D. Vignolles, H. Raffy, Z. Z. Li, P. Auban-Senzier, N. Doiron-Leyraud, P. Fournier, D. Colson, L. Taillefer, and C. Proust, Nature Physics **15**, 142 (2019).

[151] G. Grissonnanche, Y. Fang, A. Legros, S. Verret, F. Laliberté, C. Collignon, J. Zhou, D. Graf, P. A. Goddard, L. Taillefer, and B. J. Ramshaw, Nature **595**, 667 (2021), arXiv:2011.13054 .

[152] Y. Cao, D. Chowdhury, D. Rodan-Legrain, O. Rubies-Bigorda, K. Watanabe, T. Taniguchi, T. Senthil, and P. Jarillo-Herrero, Physical Review Letters **124**, 076801 (2020), arXiv:1901.03710 .

[153] K. A. Landsman, C. Figgatt, T. Schuster, N. M. Linke, B. Yoshida, N. Y. Yao, and C. Monroe, Nature **567**, 61 (2019), arXiv:1806.02807 .

[154] M. Franz and M. Rozali, Nature Reviews Materials **3**, 491 (2018), arXiv:1808.00541 .

[155] I. Danshita, M. Hanada, and M. Tezuka, Progress of Theoretical and Experimental Physics **2017**, 1 (2017), arXiv:1606.02454 .

[156] A. Chew, A. Essin, and J. Alicea, Physical Review B **96**, 1 (2017), arXiv:1703.06890 .

[157] D. I. Pikulin and M. Franz, Physical Review X **7**, 031006 (2017), arXiv:1702.04426 .

[158] Z. Luo, Y. Z. You, J. Li, C. M. Jian, D. Lu, C. Xu, B. Zeng, and R. Laflamme, npj Quantum Information **5**, 10.1038/s41534-019-0166-7 (2019), arXiv:1712.06458 .

[159] Z. Bi, C. M. Jian, Y. Z. You, K. A. Pawlak, and C. Xu, Physical Review B **95**, 1 (2017), arXiv:1701.07081 .

[160] B. I. Halperin, private communication (2021).

[161] M. Brzezinska, Y. Guan, O. V. Yazyev, S. Sachdev, and A. Kruchkov, arXiv preprint (2022), arXiv:2208.01032 .

[162] A. Altland, D. Bagrets, and A. Kamenev, Physical Review Letters **123**, 226801 (2019), arXiv:1908.11351 .

[163] S. Banerjee and E. Altman, Physical Review B **95**, 134302 (2017), arXiv:1610.04619 .

[164] B. Kobrin, Z. Yang, G. D. Kahanamoku-Meyer, C. T. Olund, J. E. Moore, D. Stanford, and N. Y. Yao, Physical Review Letters **126**, 30602 (2021), arXiv:2002.05725 .

[165] J. I. Li, C. Tan, S. Chen, Y. Zeng, T. Taniguchi, K. Watanabe, J. Hone, and C. R. Dean, Science **358**, 10.1126/science.aao2521 (2017).

[166] A. A. Zibrov, C. Kometter, H. Zhou, E. M. Spanton, T. Taniguchi, K. Watanabe, M. P. Zaletel, and A. F. Young, Nature **549**, 10.1038/nature23893 (2017).

[167] R. Ribeiro-Palau, S. Chen, Y. Zeng, K. Watanabe, T. Taniguchi, J. Hone, and C. R. Dean, Nano Letters **19**, 2583 (2019), arXiv:1901.01277 .

[168] D. Bischoff, P. Simonet, A. Varlet, H. C. Overweg, M. Eich, T. Ihn, and K. Ensslin, physica status solidi (RRL) - Rapid Research Letters **10**, 68 (2016).

[169] L. A. Ponomarenko, F. Schedin, M. I. Katsnelson, R. Yang, E. W. Hill, K. S. Novoselov, and A. K. Geim, Science **320**, 356 (2008), arXiv:0801.0160 .

[170] S. Engels, A. Epping, C. Volk, S. Korte, B. Voigtländer, K. Watanabe, T. Taniguchi, S. Trellenkamp, and C. Stampfer, Applied Physics Letters **103**, 073113 (2013).

[171] J. Güttinger, C. Stampfer, F. Libisch, T. Frey, J. Burgdörfer, T. Ihn, and K. Ensslin, Physical Review Letters **103**, 046810 (2009).

[172] J. Güttinger, C. Stampfer, T. Frey, T. Ihn, and K. Ensslin, Physica Status Solidi (B) **246**, 2553 (2009), arXiv:0905.2567v1 .

[173] J. Güttinger, C. Stampfer, T. Frey, T. Ihn, and K. Ensslin, Nanoscale Research Letters **6**, 253 (2011).

[174] J. Güttinger, F. Molitor, C. Stampfer, S. Schnez, A. Jacobsen, S. Dröscher, T. Ihn, and K. Ensslin, Reports on Progress in Physics **75**, 10.1088/0034-4885/75/12/126502 (2012).

[175] L. Banszerus, A. Rothstein, T. Fabian, S. Möller, E. Icking, S. Trellenkamp, F. Lentz, D. Neumaier, K. Watanabe, T. Taniguchi, F. Libisch, C. Volk, and C. Stampfer, Nano Letters **20**, 7709 (2020), arXiv:2008.02585 .

[176] L. Banszerus, A. Rothstein, E. Icking, S. Möller, K. Watanabe, T. Taniguchi, C. Stampfer, and C. Volk, Applied Physics Letters **118**, 103101 (2021), arXiv:2010.14399 .

[177] L. Banszerus, K. Hecker, S. Möller, E. Icking, K. Watanabe, T. Taniguchi, C. Volk, and C. Stampfer, Nature Communications **13**, 3637 (2022), arXiv:2110.13051 .

[178] C. Gutiérrez, D. Walkup, F. Ghahari, C. Lewandowski, J. F. Rodriguez-Nieva, K. Watanabe, T. Taniguchi, L. S. Levitov, N. B. Zhitenev, and J. A. Stroscio, Science **361**, 789 (2018).

[179] C. Tong, A. Kurzmann, R. Garreis, W. W. Huang, S. Jele, M. Eich, L. Ginzburg, C. Mittag, K. Watanabe, T. Taniguchi, K. Ensslin, and T. Ihn, Physical Review Letters **128**, 067702 (2022), arXiv:2106.04722 .

[180] B. Özyilmaz, P. Jarillo-Herrero, D. Efetov, D. A. Abanin, L. S. Levitov, and P. Kim, Physical Review Letters **99**, 2 (2007), arXiv:0705.3044 .

[181] M. T. Allen, O. Shtanko, I. C. Fulga, J. I. Wang, D. Nurgaliev, K. Watanabe, T. Taniguchi, A. R. Akhmerov, P. Jarillo-Herrero, L. S. Levitov, and A. Yacoby, Nano Letters **17**, 7380 (2017).

[182] W. Liang, M. Bockrath, D. Bozovic, J. H. Hafner, M. Tinkham, and H. Park, Nature **411**, 665 (2001).

[183] T. Guhr, A. Müller-Groeling, and H. A. Weidenmüller, Physics Reports **299**, 189 (1998), arXiv:9707301 [cond-mat] .

[184] F. Ghahari, H. Y. Xie, T. Taniguchi, K. Watanabe, M. S. Foster, and P. Kim, Physical Review Letters **116**, 1 (2016), arXiv:1601.05859 .

[185] Y. M. Zuev, W. Chang, and P. Kim, Physical Review Letters **102**, 096807 (2009), arXiv:0812.1393 .

[186] A. Harzheim, J. Spiece, C. Evangeli, E. McCann, V. Falko, Y. Sheng, J. H. Warner, G. A. D. Briggs, J. A. Mol, P. Gehring, and O. V. Kolosov, Nano Letters **18**, 7719 (2018).

[187] K. Zimmermann, A. Jordan, F. Gay, K. Watanabe, T. Taniguchi, Z. Han, V. Bouchiat, H. Sellier, and B. Sacépé, Nature Communications **8**, 14983 (2017), arXiv:1605.08673 .

[188] Y. Ronen, T. Werkmeister, D. Haie Najafabadi, A. T. Pierce, L. E. Anderson, Y. J. Shin, S. Y. Lee, Y. H. Lee, B. Johnson, K. Watanabe, T. Taniguchi, A. Yacoby, and P. Kim, Nature Nanotechnology **16**, 563 (2021), arXiv:2008.12285 .

[189] D. S. Wei, T. Van Der Sar, J. D. Sanchez-Yamagishi, K. Watanabe, T. Taniguchi, P. Jarillo-Herrero, B. I. Halperin, and A. Yacoby, Science Advances **3**, 1 (2017), arXiv:1703.00110 .

[190] C. W. J. Beenakker and A. A. M. Staring, Physical Review B **46**, 9667 (1992).

[191] P. Kumar, K. S. Figueroa, A. C. Foucher, K. Jo, N. Acero, E. A. Stach, and D. Jariwala, Journal of Vacuum Science and Technology A **39**, 032201 (2021).

[192] C. W. J. Beenakker, in *The Oxford Handbook of Random Matrix Theory*, edited by G. Akemann, J. Baik, and P. Di Francesco (Oxford University Press, Oxford, 2011) pp. 723—-758, arXiv:0904.1432 .

[193] K. Takase, S. Tanabe, S. Sasaki, H. Hibino, and K. Muraki, Physical Review B - Condensed Matter and Materials Physics **86**, 1 (2012), arXiv:1210.7601 .

[194] L. A. Cohen, N. L. Samuelson, T. Wang, K. Klocke, C. C. Reeves, T. Taniguchi, K. Watanabe, S. Vijay, M. P. Zaletel, and A. F. Young, arXiv preprint , 1 (2022), arXiv:2204.10296 .

[195] S.-B. Chiu, A. Mreńca-Kolasińska, K. L. Lei, C.-H. Chiu, W.-H. Kang, S.-C. Chen, and M.-H. Liu, Physical Review B **105**, 195416 (2022).

[196] P. Jarillo-Herrero, J. Kong, H. S. van der Zant, C. Dekker, L. P. Kouwenhoven, and S. De Franceschi, Nature **434**, 484 (2005).

[197] F. Yang, A. A. Zibrov, R. Bai, T. Taniguchi, K. Watanabe, M. P. Zaletel, and A. F. Young, Physical Review Letters **126**, 156802 (2021), arXiv:2008.05466 .

[198] A. J. M. Giesbers, U. Zeitler, M. I. Katsnelson, L. A. Ponomarenko, T. M. Mohiuddin, and J. C. Maan, Physical Review Letters **99**, 206803 (2007).

[199] A. T. Pierce, Y. Xie, S. H. Lee, P. R. Forrester, D. S. Wei, K. Watanabe, T. Taniguchi, B. I. Halperin, and A. Yacoby, Nature Physics **18**, 37 (2022), arXiv:2103.00015 .

[200] T. F. Heinz, in *Carbon Nanotubes* (Springer, 2007) pp. 353–369.

[201] F. Wang, G. Dukovic, L. E. Brus, and T. F. Heinz, Science **308**, 838 (2005).

[202] T. Michel, M. Paillet, D. Nakabayashi, M. Picher, V. Jourdain, J. C. Meyer, A. A. Zahab, and J. L. Sauvajol, Physical Review B **80**, 1 (2009).

[203] D. Y. Joh, L. H. Herman, S. Y. Ju, J. Kinder, M. A. Segal, J. N. Johnson, G. K. L. Chan, and J. Park, Nano Letters **11**, 1 (2011).

[204] H. Ajiki and T. Ando, Physica B: Physics of Condensed Matter **201**, 349 (1994)

This thesis was typeset using LaTeX, originally developed by Leslie Lamport and based on Donald Knuth's TeX. The body text is set in 11 point Egenolff-Berner Garamond, a revival of Claude Garamont's humanist typeface. A template that can be used to format a PhD thesis with this look and feel has been released under the permissive MIT (X11) license, and can be found online at github.com/suchow/Dissertate or from its author, Jordan Suchow, at suchow@post.harvard.edu. Thanks again to my amazing family! I couldn't have done this without all of you.